Suspended graphene on silicon photonics for pressure sensors

A thesis submitted to the University of Manchester for the degree of:

Master of Philosophy

in the Faculty of Science & Engineering.

2021

Rory Owain Phillips

Department of Materials

Contents

List of Figures

List of Tables

List of Abbreviations

µm	Micrometre
3D	Three-dimensional
APS	Ammonium persulfate
CCD	Charge-coupled device
CMOS	Complementary metal-oxide semiconductor
CVD	Chemical vapour deposition
DI	Deionised
EBL	Electron beam lithography
EM	Electromagnetic
FHD	Flame hydrolysis
GO	Graphene oxide
GPa	Gigapascal
IPA	Isopropanol
MPa	Megapascal
NGI	National Graphene Institute
NIR	Near infra-red
nm	Nanometre
PMMA	Poly (methyl-methacrylate)
PM-PCF	Polarisation-maintaining photonic crystal fibre
PZT	Lead zirconium titanate
rGO	Reduced graphene oxide
SEM	Scanning electron microscope/microscopy

TE	Transverse electric
TEM	Transmission electron microscope/microscopy
TIR	Total internal reflection
TM	Transverse magnetic
TO	Transverse optical
TPa	Terapascal
TPA	Two photon absorption
UV-Vis	Ultraviolet-visible spectroscopy (UV-Vis)
XPS	X-ray photoelectron spectroscopy

Abstract

Graphene is an optically active material that can be interfaced with silicon photonics. It has been shown that graphene attenuates the evanescent field of light surrounding a silicon photonic waveguide when in close proximity. However, there is little research into the interfacing of graphene oxide (GO) and reduced graphene oxide (rGO) with silicon photonics. These materials are less optically active and, as such, are better candidates for larger interaction lengths. In order to achieve this interfacing, robust membranes need to be fabricated and examined.

This work investigates the effect of GO and rGO on light travelling through silicon photonic waveguides. It also examines the relationship between light intensity and interaction length of rGO membranes in contact with bus waveguides. This work developed the membranes necessary to interface rGO with silicon photonic waveguides. The results showed that rGO/Parylene-C membranes can attenuate the evanescent field of light over a silicon photonic waveguide. These membranes have been evaluated using AFM through suspension over hole structures in Si/SiO_2 substrates and blister testing. New protocols for Parylene-C CVD coating of rGO membranes have been established. It was found that the rGO/Parylene-C membranes were stable enough to transfer and inflate into blisters.

It is anticipated that further developments into the use of 2D materials with silicon photonic waveguides following this research will result in the creation of touch attenuation pressure sensors. This will be achieved by suspending membranes above waveguides and allowing pressure changes to push the membranes closer into the evanescent field. Knowing the relationship between attenuation and distance from the evanescent field, the pressure will be readily calculated.

Declaration

No portion of the work referred to in the thesis has been submitted in support of an application for another degree or qualification of this or any other university or other institute of learning.

Rory Owain Phillips

Copyright Statement

Acknowledgements

I would like to thank Aravind Vijayaraghavan and Iain Crowe for guiding me on this journey.

Chris Berger deserves a special mention for teaching me the tricks of the cleanroom and putting up with me generally. Thanks, chief!

I am forever indebted to Cian Bartlam for being my rock throughout this process. Without Cian, this would not have been possible to achieve. Thank you for your unimpeachable knowledge of chemistry and characterisation and for the general craic and chats we enjoyed over pints and roll-ups. I hope that our relationship is forever strong and stable.

Wentao Zou, thank you for your insightful knowledge and caring nature. I am humbled to be able to call you a friend. Thanks also to Nat Parsons for being my agony aunt and injecting me with vigour when the road seemed too tough to navigate.

Mark Hibbert, my friend and confidante, thank you for facilitating rent-free living for my time as a postgraduate and opening my eyes to some of Manchester's choicest venues.

Richard Blundell, Sam Kelly, Emily Cookesy, Luke Prince and Jason Burke – thanks for keeping me grounded and showing me the meaning of moderation.

Medzy Boi and Hummus, your confidence in me was unwavering. Never change.

Thank you to my family for being a constant source of guidance and for reminding me of the importance of prioritisation.

Thanks also to Toffee, you never judged me, and for that, I am truly grateful.

Most importantly, Danie McCool, thanks for putting up with me; we got there in the end!

1. Introduction and Aim of the Project

1.1 Introduction

Researchers at the University of Manchester have recently demonstrated that graphene can be interfaced with silicon waveguides, particularly ring resonators, to modulate the transmission of light.[1] The resultant effect can be used in sensing. For instance, by dynamically varying the height of the graphene above the waveguide, an optical nano-mechanical actuator can be developed, which will serve as a force, pressure or acoustic sensor. Graphene is known for its unique combination of extraordinary stiffness and high electrical conductivity and the ability to modulate the electromagnetic field in its surrounding medium, therefore it can be employed as a sensor. A sensor functioning through the interaction of a graphene based membrane integrated with a photonic device (i.e. waveguides) is targeted. Ultimately, pressure waves in an aqueous medium that the sensor is in contact with would be measured as a change in the optical transmission in the waveguide to function as a touch attenuation sensor.

1.2 Aim of the Project

In this project, graphene polymer composite membranes will be developed and their properties measured. These membranes will be evaluated for their potential use interfacing with photonic chips. This will then form the baseline knowledge needed for the development of silicon photonic pressure sensors.

The research project aims to develop the underlying knowledge needed to fabricate a pressure sensor that utilises the evanescent field surrounding a silicon waveguide. Graphene oxide (GO) and reduced graphene oxide (rGO) membranes will be fabricated. These will then be coated with a polymer layer before being suspended over hole structures in silicon dioxide. GO and rGO will be interfaced with silicon photonic waveguide chips

The following objectives will aim to be met along the course of the project:

1. Fabricate GO/rGO polymer composite membranes.
2. Suspend the membranes on hole structures and evaluate using AFM.
3. Optically measure GO/rGO interfaced with silicon photonic chips.

2. Literature Review

2.1 2D Materials

2.1.1 Graphene

Graphene has quickly become the most studied nano-material due to its one atom thickness and remarkable properties. As research develops into this unique material, more applications will be found for graphene, so manufacturing it on an industrial scale will become an important leap forward in making it more accessible for developing technologies.

Graphene was first discovered by Professors Andre Geim and Kostya Novoselov in 2004 using the scotch tape method.[2] Graphene was the first-ever 2D material to be discovered, with strictly 2D materials having been theorised as thermodynamically impossible by Peierls and Landau in the 1930s.[3,4] Geim and Novoselov discovered graphene at the University of Manchester using a method that is now known as the "scotch tape method". They used the graphene that they had produced to fabricate devices to study the electronic properties.[5] This study won the pair the Nobel Prize for Physics in 2010 and began the surge in interest in graphene and 2D materials. Its exceptional properties have led to graphene being studied in nearly every field of science and engineering.[6] Graphene is a two-dimensional monolayer lattice of carbon atoms,[6] taking the form of a honeycomb lattice of sp^2 carbon atoms with bond lengths of 0.142 nm.[7] In the form of a single sheet of carbon atoms, the thickness of monolayer graphene is the same as the atomic diameter of carbon, 0.34 nm.[8] Graphene exhibits some exceptional properties.

Defect-free graphene has a Young's modulus of about 1 TPa and fracture strength of about 130 GPa. These properties were measured using nano-indentation in an atomic force

microscope by Lee et al.[9] As a 2D material, it has a specific surface area of 2630 m^2g^{-1} and has an optical transmittance of 97.7%.[10]

As well as excellent mechanical properties, graphene is highly conductive, both electrically and thermally. The electrical conductivity is measured at 1738 S m^{-1}, which makes graphene an ideal candidate for use in electronic applications.[11] The thermal conductivity at room temperature has been measured to be 5300 W m^{-1} K^{-1}, which is even greater than single-wall carbon nanotubes.[12] This excellent thermal conduction is beneficial to potential electronic applications and would allow graphene to be used in thermal management.[13] Figure 1 shows a comparison of some of graphene's physical properties to other materials.

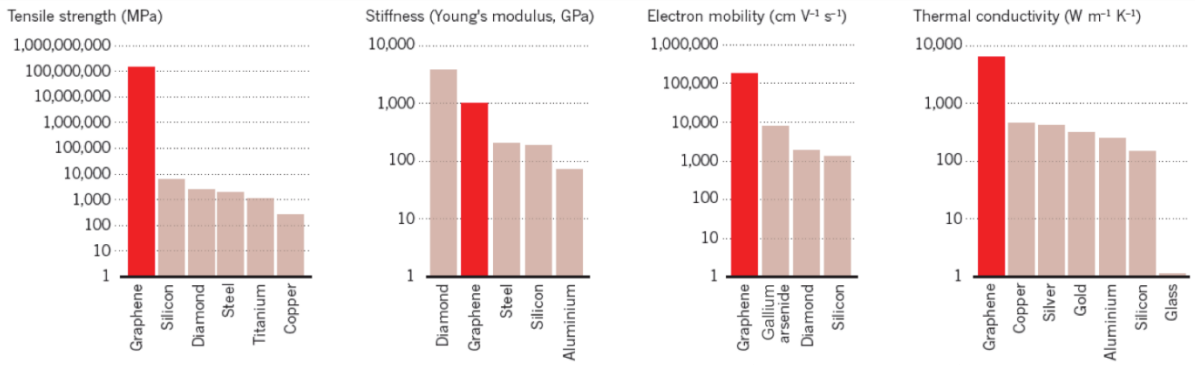

Figure 1: Bar charts showing some of graphene's physical properties compared to other materials.[14] (The electron mobility measurements were taken at 200K)

Another valuable property of graphene is that it can be readily functionalised.[15] This is done either covalently or non-covalently to enhance and manipulate properties such as biocompatibility, sensitivity, loading capacity and specificity.[16] Through functionalisation, graphene has the potential to be used in a plethora of wide-ranging applications.

Graphene has been linked to a wide variety of potential applications. The range of applications under discussion varies from filler in composites to optoelectronics.[17] In terms of using graphene's electrical properties, research into the potential use of graphene in

supercapacitors, interconnects, field emitters, and batteries has exploded.[18] Ultracapacitors have been created with the use of a chemically modified graphene that utilises the specific surface area and excellent electrical performance.[19] Graphene has extremely low optical absorbance, making it transparent. This is an important property for materials used in solar cells. Graphene films have been investigated for use in solar energy capture in place of the industry-standard indium tin oxide.[20] These properties are also linked to replacing metal oxides in liquid crystal displays.

There are two main approaches to produce graphene, namely top-down approaches, including mechanical exfoliation, unzipping of carbon nanotubes and chemical derivation (via the reduction of graphene oxide), and bottom-up approaches, including epitaxial growth, chemical vapour deposition (CVD), amongst others.[21]

Mechanical exfoliation was the first method ever used to produce graphene, with the previously mentioned “scotch tape method”. This is the repeated micromechanical cleavage of graphite to give monolayer graphene. Although the resultant graphene is suitable for fundamental studies, it is labour intensive and not appropriate for mass production.[22]

Shear exfoliation of graphite has been applied to produce graphene platelets in the range of 300-800 nm. This involves suspending the graphite in a solvent and then applying high shear with the use of a fast-spinning rotor. Currently, this technique can produce graphene platelets in liquid suspension at a rate of approximately 4 g h^{-1}. Ultimately, the production rate needs to be significantly higher to meet the demands of a growing market of products that utilise graphene.[23]

Graphene nanoribbons are produced by the "unzipping" of carbon nanotubes using one of a number of methods ranging from electrical to chemical.[24] Nanoribbons are generally around 10 nm in width (depending on the process of production) with a length/width ratio higher than 10.[25] The nanoribbon approach is not a viable route to mass production of graphene but has potential in applications in bio imaging contrast agents[26] as well as being used as a filler for enhancing the mechanical properties of polymeric composites.[27]

Chemical derivation involves the oxidation of graphite, followed by exfoliation and reduction back to graphene. It presents the advantage of using cheap precursors, low reaction temperature, high production yield and chemical reactivity for specific use. However, there are a few disadvantages to be overcome, such as the use of hazardous chemicals (strong acids and oxidizing agents) and the deterioration of graphene properties due to residual defects in the lattice (i.e. electrical conductivity).

Epitaxial growth of graphene is performed by annealing a silicon carbide (SiC) crystal at temperatures of around 2000 K in ultra-high vacuum conditions.[28] In this process, a single crystalline layer of graphene is deposited onto the SiC substrate. Although this method produces large areas of pure graphene on the crystal, it is tough to functionalise it as a result.

2.1.2 Graphene and Photonics

Graphene has many remarkable optoelectronic properties that are highly desirable for photonic applications but unobtainable or non-optimal in other complementary metal-oxide semiconductor (CMOS)-compatible material systems.[29,30] These include ultra-wideband absorption[31,32], controllable inter-band transition[33,34], saturable nonlinear absorption[35] and high-mobility ambipolar carrier transport.[36,37] Furthermore, the ability to produce high-quality graphene at the wafer scale[38], transfer and integrate graphene onto heterogeneous substrates[39], and pattern it into planar devices[40,41], makes practical application of graphene for optoelectronic devices imminent. Therefore, incorporating graphene with Si- compatible photonics is a promising approach toward realising practical high-speed, low-power photonic systems integrated with CMOS circuits[42]. Many graphene-based devices have been demonstrated recently, including photodetectors[43,44], modulators[45,46], polarization controllers[47] and ultra-fast pulsed lasers.[48,49]

Graphene can absorb light from an extensive range of wavelengths, ultraviolet through to infrared; this lends it to be used in photonic devices such as optical modulators and ultrafast, high band-width photodetectors.[45] In the gapless electronic structure of graphene, its low density of states (DOS) near the Dirac point and its 2D structure confines electrons in one atomic layer makes transparency almost independent of wavelength from visible to infrared.[50,34]

Optical modulators are key for altering the properties of light, be it phase, amplitude or polarisation. This is achieved by electro-refraction or electro-absorption .[51] Mach–Zehnder interferometers[51,52] are optical modulators that are based on interference. Ring or disk resonator[53,54] based modulators rely on resonance, and germanium- or III–V-based electro-

absorption modulators[55,56] rely on bandgap absorption. The operating spectra of optical modulators are usually narrow[53–57]. Putting mono-layer graphene onto a silicon waveguide has been reported by Liu et al. to provide an ultrafast response time.[45]A drive voltage modulates the interband transitions of photo-generated electrons over broad spectral ranges, meaning that graphene can be incorporated with a broadband and high-speed optical modulator. Liu et al. have shown that their CMOS-compatible graphene optical modulator can be as small as 25 μm^2, operate at a speed of 1.2 GHz whilst providing excellent performance over broad operating spectra ranging from 1.35 µm to 1.60 µm and a modulation efficiency of ~0.1 dB μm^{-1}.

2.1.3 Graphene Oxide (GO)

Graphene oxide is an oxygenated form of graphene sheet covered with oxygen groups on both the basal plane and edges.[58] The functional groups increase the interlayer spacing and give rise to hybridisation of the planar sp^2carbons to tetrahedral sp^3.[59] Graphene oxide is seen as a viable route to graphene by reduction to produce reduced graphene oxide. This reduced graphene oxide is becoming closer to micro-exfoliated graphene flakes in terms of electrical properties as the reduction of graphene oxide improves.[60]

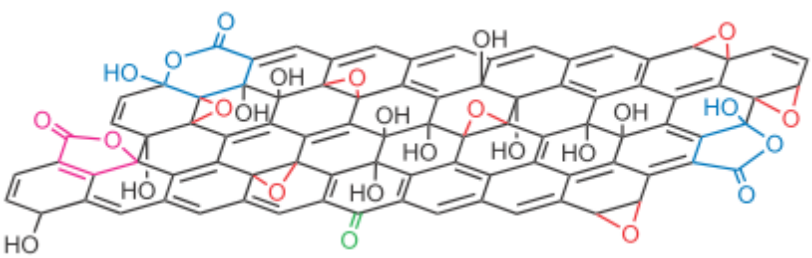

Figure 2: The most recent structural model of graphene oxide.[61]

The structure of graphite oxide has been researched most notably by Hofmann in 1939[62], Ruess in 1946[63], Scholz-Boehm in 1969[64], Nakajima-Matsuo in 1994[65] and Lerf-Klinowski in 1998[66]. The most up-to-date structural model for graphite oxide was proposed by Ajayan et al. in 2009, having used carbon-13 nuclear magnetic resonance spectroscopy (^{13}C NMR) to determine the presence of five and six-membered lactol rings.[61] Figure 2 shows a model of the most recent structure.

Graphite oxide has the base structure of graphite, with individual layers of carbon atoms in a honeycomb lattice on each layer but with several groups on the basal planes and edges resulting from oxidation. Graphite oxide has varying sizes of islands of unoxidised aromatic sp^2 carbons, which are separated on the basal plane by covalently bonded ether (C-O-C) and phenolic (C-OH) groups. At defects and edges, carboxyl (COOH), ketone (=O), and quinone groups are present. As the oxidation time and temperature of the reaction are increased, carbon double bonds and phenolic groups can develop into single bonds, ether, carbonyl and hydroxyl groups.[67–69] Where graphite has an interlayer d-spacing of 0.34 nm, graphite oxide has a d-spacing of ~0.83 nm.[70]

Graphene oxidation levels vary depending on the methodology of synthesis. The maximum C/O ratio lies between 1.8 and 2.5.[71] Due to the oxygen-containing groups on basal planes and edges, as well as unoxidised sp^2 domains; graphene oxide can be regarded as amphiphilic. As opposed to graphene, GO is not hydrophobic and can be dispersed in water and other polar solvents. Due to the ionisation of phenolic hydroxyl and carboxylic acid groups, GO flakes are negatively charged.[72] Therefore, the stability of the GO in water occurs because of the electrostatic repulsion between negatively charged flakes, as well as hydrogen bonds with water molecules.[73]

The advantage of GO being dispersible in water represents its high potential for practical applications, especially for biodevices and drug delivery systems.[74] For example, it has recently been suggested that cancer stem cells may be eradicated through the use of graphene oxide as a nontoxic therapeutic method.[75] Graphene oxide membranes have also been examined for use as gas filters with membrane thicknesses approaching 1.8 nm in some cases.

GO, especially nano-sized GO, possesses a tuneable florescence from blue to near-infrared (NIR) region[76] and therefore, nano-graphene oxide can be used as a fluorescence sensor.[77,78] Moreover, some reports have shown the successful application of nano-sized graphene oxide in cellular imaging and drug delivery due to the above mentioned properties[79–81] and also in photo-thermal therapy due to the ability of nano-graphene oxide to absorb in the NIR region.[82]

2.1.4 Reduced Graphene Oxide (rGO)

Graphene oxide has been researched most commonly as a route to graphene. Through reduction, graphene oxide becomes reduced graphene oxide (rGO), which has properties closer to pristine graphene. By controlling the ratio of sp^2 and sp^3 bonding carbons, rGO can be altered to go from insulating GO to a semiconductor and even to semi-metal electrical properties.[83] Field-effect devices with mobility values of 5,000 $cm^2 V^{-1} s^{-1}$ have been reported with advances in efficient reduction processes.[84]

There are a number of reduction methods: chemical, thermal, or electrochemical reduction pathways.[72] The most common method uses hydrazine, but less toxic methods have been evaluated using sodium borohydride.[61] Electrochemical reduction is a potential green method since electrons are the reducing agents. The electrons can diffuse anywhere the electrolyte exists or in electric conductors. It may also be a good option for temperature sensitive materials given its ability to be carried out at room temperature.[85] Each of the reduction methods result in rGO that has varying degrees of resemblance to pristine graphene with regard to surface morphology and physical properties. For the applications where the "pristine graphene" properties are more required (electronics, composites etc.), less defective and larger rGO flake sizes are desired.

2.2 Pressure sensors

Current acoustic pressure sensors use piezoelectric lead zirconium titanate (PZT) ceramic transducer systems. The ceramics are based on PZT (a registered trademark of Clevite Corporation), which represents a composition in the ceramic of 52-54 mole % lead zirconate ($PbZrO_3$) and 46-48 mole% lead titanate ($PbTiO_3$).[86] These sensors are mounted in large arrays on the scale of tens of metres square in their application. PZT has a theoretical density of 7.9 g cm^{-3},[87] PZT, when used in sensors, resulting in bulky and heavy devices, which are not helpful for efficiency when mounted on a vehicle. Not only this, but PZT is expensive to manufacture and process.

Using graphene in a pressure sensor offers several benefits. As will be mentioned later in more depth, graphene is lightweight, strong, and conductive. Not only this, but with new

methods of synthesis, graphene is becoming processable on larger areas and is becoming progressively cheaper to produce and manipulate.

Using photonics in pressure sensing is beneficial because the signal is not affected by electromagnetic (EM) radiation. Being ferroelectric, PZT has a spontaneous electric polarization (electric dipole) that can be reversed in the presence of an electric field. With the pressure sensors likely to be in close proximity to a lot of EM radiation emitters, using photonic chips will allow for pressures to be measured without the signal being impeded by EM radiation.

Graphene and silicon photonics offer the additional benefit of being flexible in terms of design through micromachining. Fabrication processes outlined later in the report will show the small scales at which graphene can be manipulated.

2.3 Photonic Pressure sensors

Silicon photonics can be defined as utilising silicon-based materials for the generation, guidance, control and detection of light.[88]

Polarisation-maintaining photonic crystal fibre (PM-PCF) has become more readily available recently, attracting a lot of research interest in investigating its potential in communications and sensing applications.[89–91] PM-PCF possesses very low bending loss due to the large numerical aperture and small-core diameter. This feature is crucial for the realization of practical sensors.

Pressure measurement results from a 58.4 cm PM-PCF-based Sagnac interferometer used by Fu et al.[92] show a sensing sensitivity of 3.42 nm MPa^{-1} with a demonstrated measurement range of 0.3 MPa. Exceptionally low bending losses of the PM-PCF allow the fibre to be coiled into a 5 mm diameter circle, which allows for a very small pressure sensor to be manufactured.[92] This proposed pressure sensor has the advantages of being compact in size, highly sensitive, low temperature-sensitive, and potentially low cost.

In 1994, De Brabander et al. developed an optical pressure sensor that used an integrated optical ring resonator to measure the strain induced in a micro-machined silicon diaphragm.[93] This method is similar to the intended approach to be trialled in this project. However, instead of using a silicon diaphragm, suspended graphene will be used as the direct pressure sensing membrane.

A touch attenuation optical waveguide pressure sensor was described by Kodl[94] that operated by attenuating light by pressure moving a cladding material into the evanescent field of light that decays exponentially from the core-cladding interface. Graphene can be used as an attenuator of light in the evanescent field in a similar way. It is this type of sensor that will be adapted for the project.

2.4 Visualising 2D Materials

2.4.1 Optical microscopy

Graphene is visible using optical microscopy under a broad range of conditions. If graphene is deposited onto a silicon dioxide coated silicon substrate, light is allowed to propagate through the graphene and the oxide layer before being reflected by the bulk silicon material. The reflected light interferes with the incoming light such that a contrast is created. Fresnel theory describes the contrast as being dependent on the wavelength of the light and the thickness of the oxide layer. Light is able to propagate through the graphene and the oxide layer, reflect off the bulk silicon substrate and interfere with the incoming light source, thereby creating a contrast. This contrast, described by Fresnel theory, is dependent on the wavelength of the light source and thickness of the oxide.[95] Figure 3 shows the optical contrast as a function of wavelength and oxide thickness. Since green is most comfortable to the human eye for viewing, oxide thicknesses of ~90 nm and ~290 nm are desirable for good optical contrast.

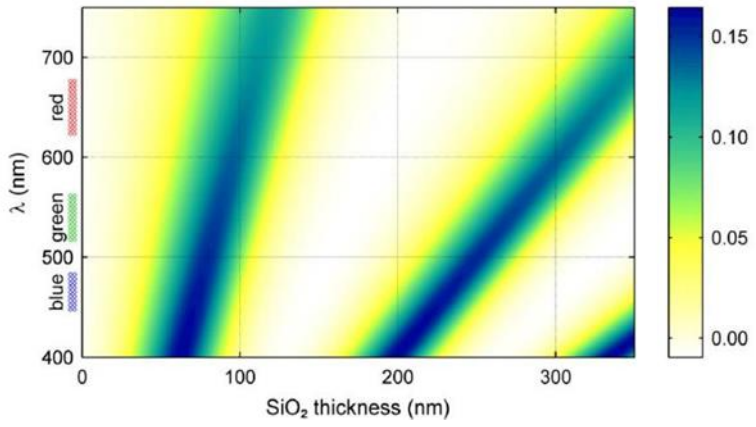

Figure 3: Colour plot of the contrast as a function of wavelength and SiO_2 thickness. The colour scale on the right shows the expected contrast.[95]

2.4.2 Atomic force microscopy (AFM)

AFM provides a 3D map of the surface of a sample on a nano-scale by measuring forces between a sharp silicon nitride probe with a tip width of <10 nm and the surface at a very small distance. The tip is attached to a cantilever which is scanned across the surface of a sample by using a feedback loop and a piezoelectric scanner. A laser is shone onto the back of the cantilever as the probe scans the surface, and a measurement is taken at every contact of the tip with the sample. The laser is reflected onto a position-sensitive photodetector. The amount of bending of the cantilever at the point of contact during scanning is translated into a map of the topography of the surface.

The two primary modes to be used in this project are contact mode and tapping mode.

In contact mode, repulsive Van der Waals forces are used. The cantilever bends when the spring constant of the cantilever is less than the surface. The force on the tip is repulsive. Using feedback loops, a constant cantilever deflection can be maintained, the force between the sample and the probe remains constant, allowing for an image of the surface to be resolved. This mode can scan relatively fast but can damage soft samples due to the forces involved.

In tapping mode, the AFM cantilever is oscillated at or near its resonance frequency by a piezoelectric actuator. The AFM tip touches the surface at the lower end of its vertical movement. This is better for samples that are more fragile or loosely attached to a surface (for example, graphene transferred onto a substrate). However, slower scan speeds are required. Tip-surface adhesion is usually not a problem because the stiff AFM cantilevers used have enough energy at the contact point to overcome the attractive forces. For the

feedback in this mode of operation, the effect of the resonant amplitude of the oscillating tip is measured rather than the deflection as in contact mode.

2.5 Photons and matter

2.5.1 Photoelectric effect and photo-excitation of carriers

In photoelectric (photon-electron) interaction, a photon transfers all of its energy to an electron which is then emitted. These are called photoelectrons. As the photoelectrons pass through the surrounding matter, the rapidly lose their energy, moving only a small distance from their initial location. Therefore, the energy of the photon is transferred into the matter close to the point of photoelectric interaction. Photoelectric interactions are only possible when the photon has sufficient energy to overcome the binding energy of the electron; the rest of the photon's energy is used by the electron as it moves into the surrounding matter. This is a two-step energy transfer process as there are two discreet steps – photon to electron and electron to surrounding matter. A vacancy is created in this interaction, typically in either the K or L electron shell. To fill the vacancy, another electron in an outer shell drops energy level. This often produces a characteristic X-ray photon which is dependent on the binding energies of the electrons involved. This is known as fluorescent radiation. Photoelectric interactions can cause both attenuation and absorption. The probability of photoelectric absorption is related to the atomic number of the absorbing material, Z, and the energy of the photon, E. This is approximated by:

$$\propto \frac{Z^3}{E^3}$$

2.5.4 X-ray photoemission spectroscopy (XPS)

XPS is the most powerful technique to follow chemical changes in graphene. A sample is irradiated with x-rays of specific energy, causing the ejection of electrons. These soft X-rays overcome the binding energy of the electrons, and the velocity and number of ejected electrons are measured. The ejected photoelectrons have specific kinetic energies which are used directly to identify the elements in a sample. From the photoelectron intensities, the relative concentrations of elements can be determined. Variations in the binding energies and the resulting chemical shifts of the photoelectron lines give information on the chemical states of the constituent elements. When measuring a 2-dimensional sample on a substrate, several layers of the material need to be used to remove interference from the substrate.

The core electrons of a carbon atom are in the $1s^2$ orbital. The incident photons, therefore, eject electrons from this orbital. The XPS spectrum shows the binding energy of the electrons against the intensity. It is the chemically shifted peaks (i.e. additional peaks) that show that it is GO rather than the loss in intensity of the graphene related peak. The spectrum marked “a” in Figure 4 shows the spectrum for graphene and “b” shows the spectrum for GO. This spectrum shows 3 components which can be assigned to graphitic C=C, C-O, and C=O species, respectively.[96]

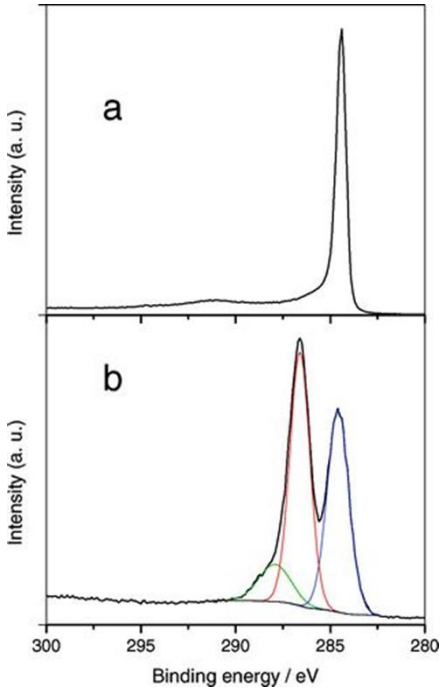

Figure 4: XPS spectra of graphene, a, and graphene oxide, b.[22]

The single peak in spectrum "a" of Figure 4 corresponds to the kinetic energies of the ejected electrons from the $1s^2$ orbital. There is only a single peak due to the fact that graphene has only one type of carbon atom bonding with itself across the honeycomb lattice; this is known as the C 1s peak. The C 1s spectrum will exhibit significant asymmetry toward higher binding energies due to the creation of low-energy electron-hole pairs.[97]

In graphene oxide, there is a much more complex C 1s peak. There are two types of carbon-oxygen bonds that give rise to the red and green peaks in the "b" spectrum. Due to the reduced amount of carbon-carbon bonds, the intensity of the peak is much lower than for pristine graphene.

2.5.2 Rayleigh scattering

When an electromagnetic wave interacts with an atom, the oscillation of the electric field creates an oscillating dipole when the atom's electrons are moved back and forth. This can be thought of as the electron cloud being raised to a "virtual" energy state. This lasts for an extremely short period of time, i.e. in the order of 10^{-14} seconds. Upon dropping back to the ground energy state, the oscillating dipole radiates a photon at the same frequency as the incident photon. This radiation is seen as scattered light and the process is entirely elastic. Rayleigh scattering has been employed as a way of quickly identifying single layer and multilayer samples in Rayleigh scattering microscopy, which can then be combined with Raman scattering for structural identification.[98] Rayleigh scattering is discussed further in the section on Raman spectroscopy.

2.5.3 Raman scattering

Raman scattering differs from Rayleigh scattering as it is inelastic. During the scattering process, the light photons either gain or lose energy – decreasing or increasing in wavelength, respectively. If the electrons of an atom are promoted from ground to virtual state and then drop back down to a higher vibrational state, then the photon that has been scattered has less energy than the incident photon and therefore has a longer wavelength. This phenomenon is known as Stokes scattering. If the atom is in a vibrational state, to begin with, then returning to ground state after scattering, then the scattered photon has more energy and, therefore, a shorter wavelength. This is anti-Stokes scattering. The difference in energies from the incident and resulting photons in the scattering process is carried away by a phonon – a quasi-particle that is the quantum of the lattice vibrations.

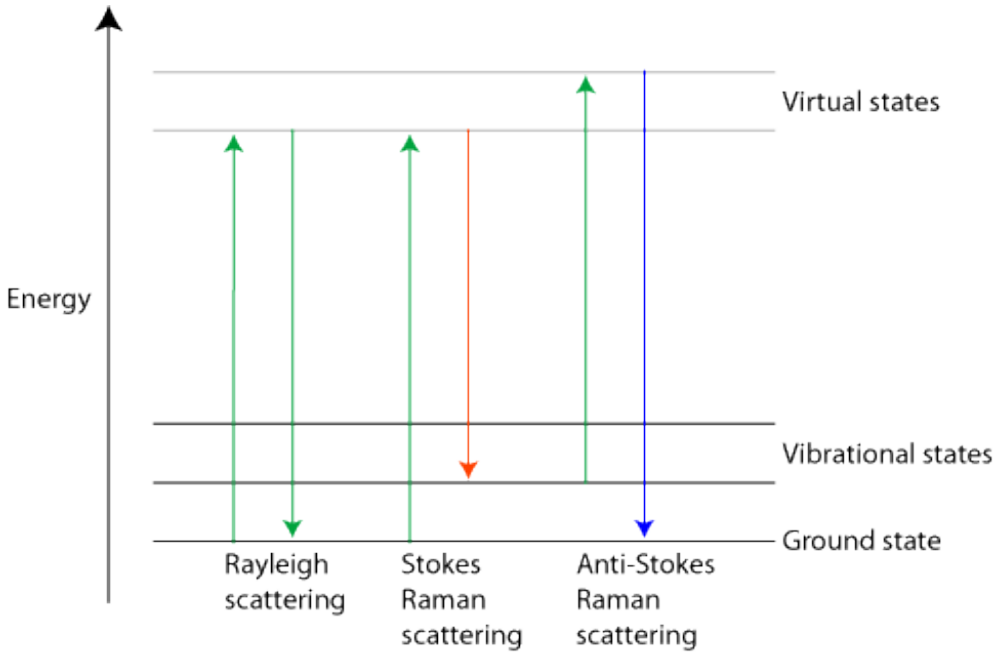

Figure 5: Rayleigh, Stokes and anti-Stokes scattering energy levels.[99]

Raman spectroscopy usually uses only the Stokes half of the spectrum as the intensity is much greater. Stokes scattering is a result of excitation from the ground state to an excited state, with the generation of a red shifted photon relative to the incident wavelength. Anti-Stokes requires the lattice to already be in an excited state, which relaxes to the ground state, producing a blue shifted photon. Generally, the Boltzmann distribution plays a role in that the population of the ground state at equilibrium is typically much higher than the excited states, therefore increasing the transition probability and observed intensity of the Stokes scattered light.

2.5.4 Raman spectroscopy

Raman spectroscopy is extremely useful for characterising graphene. This technique provides information on atomic and molecular vibrations that can be used for sample identification and characterisation. A Raman spectrum can give information on functionalisation, number of layers and defects.[100]

When an incident beam of monochromatic photons hits the sample, most of the light scatters elastically undergoing Rayleigh scattering – the energy of the photon is not changed upon scattering. However, about 0.001% of this light undergoes Raman scattering, where electrons in the sample are excited to different states (essentially molecular vibrations). This happens because of interactions between incident photons and the vibrational energy levels of molecules in a sample, as described above. The vibrational frequencies are specific to chemical bonds of molecules, and so the wavenumbers that are obtained in the spectrum represent a molecular 'fingerprint' of the sample with the intensities proportional to the concentration of the components of the material. The intensity of the shift in frequencies of the vibrations gives a Raman spectrum for a sample. Figure 6 shows a representative spectrum of a graphene edge and displays the notable peaks.

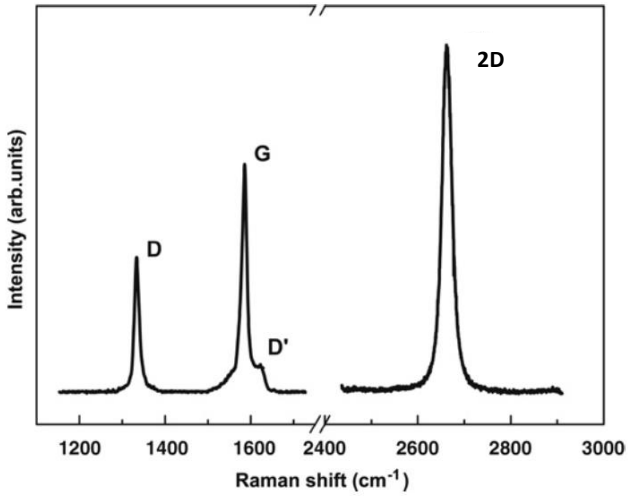

Figure 6: Spectrum of a graphene edge, showing the main Raman features, the D, G and 2D bands.[101]

The band (or peak) positions lie at frequencies that correspond to the energy levels of different molecular vibrations. Therefore the peaks in a Raman spectrum are characteristic of the available bond vibrations in a sample.

Pristine graphene's two most notable peaks are the G peak at 1580 cm^{-1} and the 2D peak at 2700 cm^{-1}. The D band at 1350 cm^{-1} and the D' band at 1620 cm^{-1} appear when there is disorder in the graphene lattice. The Raman shift values are dependent on the excitation laser source and so are not always at the exact positions quoted here. This is due to the double resonant Raman scattering of the D, D' and 2D peaks, with recombination of the excited electron hole occurring at the same symmetry point. Due to conservation of energy, this is dependent on the initial excitation energy. The G band is nondispersive as it is due to single phonon scattering between symmetry points.[101] A typical first-order Raman scattering process gives rise to the G band. There are two scattering processes that give rise to the D band: one elastic scattering by a defect in the lattice and one inelastic scattering by

the emission or absorption of a transverse optical (TO) phonon. The description of transverse phonons relates to the condition where the momentum is perpendicular to the wavevector of the incident light. The optical character arises from the fact that adjacent atoms in the lattice oscillate out of phase with respect to each other. The 2D band occurs from two TO phonons near the K point. The double resonance process involved in the D' and D bands is known as an intervalley process because it connects two non-equivalent K and K' points in the first Brillouin zone. The D' band is the same as the D band in the sense that it occurs from a defect and a TO phonon, however, it is an intravalley process as it connects two points around the K point or the K' point alone. As the defect density increases, the I_D/I_G ratio increases up to a maximum. After this point, structural defects of the basal plane dominate, forming a discontinuous lattice where the scattering process for the D band becomes limited. This increases the FWHM as the number of slightly different sp^2 states in the system increases, giving rise to a perceived broadening of the bands.

The processes involved in gaining a spectrum from a Raman spectrometer take the following path:

Firstly, a laser source is used to optically excite the sample. The monochromatic laser beam is channelled through illumination optics onto the sample. Next, the light is collected through collection optics. Wavelength filters and selector optics are applied to receive the relevant light required to produce a spectrum. The light then reaches the CCD (charge-coupled device). This acts as a photo-detector which turns the optical signal into an electrical signal that will be sent to display a spectrum on a computer.

2.5.5 Ultraviolet-visible spectroscopy (UV-Vis)

This spectroscopy technique gives the concentration of a solution. This is very useful for quickly analysing graphene oxide in solution. A range of wavelengths of light, typically 200 to 700 nm, is passed through a sample in solution.

The valence electrons of a sample are excited from the valence to the conduction bands. The transition of electrons from the valence to conduction bands is relatively low energy. Therefore, the transitions can be accomplished using low energy visible and ultraviolet photons.

Concentration determination is found using the Beer-Lambert law:

$$A = \varepsilon\, b\, c$$

In this equation, A is the absorbance which is found by taking the logarithm of the incident intensity divided by the intensity at length b in the sample ($A = \log(I_0/I)$. ε is the molar absorptivity measured in mL mg^{-1} cm^{-1}. b is the length of the path that the light takes through the sample in centimetres. c is the concentration of a compound within the solution, which is measured in mg ml^{-1}.

To determine the concentration of a sample, a calibration curve is first obtained. This is done for every new sample. The absorptions of different concentrations of a solution are recorded. The absorption intensity is plotted against the concentration of each dilution. According to the Beer-Lambert law, absorbance is proportional to concentration, and so a straight line is expected. The gradient of this line gives the absorption coefficient. This can then be used to calculate the concentration of any other solution of an unknown concentration by measuring the absorption intensity. At high concentrations, the Beer-

Lambert law starts to break down such that the concentration dependence is no longer linear, and so low concentrations must be used (hence the dilution step).

2.6 Photons and graphene

The electronic structure of graphene is unique in that the conical-shaped conduction and valence bands meet at the Dirac point. Because of this, the optical conductance of monolayer graphene is frequency-independent.[102] The optical absorbance of graphene is also frequency-independent and is proportional to the number of layers, i.e. single-layer graphene absorbs 2.3%, bilayer graphene absorbs 4.6% etc. In terms of photonics, tuning the absorbance of graphene is very important. [103] Controlling photon-graphene interactions is feasible due to the fact that the chemical potential can be tuned with an external electric field.[33],[34]

Graphene is a promising material for photon-electron conversion[29] due to its unique optical properties.[104] In graphene, multiple electron-hole pairs (excitons) can be produced from a single incident photon. This happens during the energy relaxation of the initially created exciton. There are two methods by which the relaxation occurs. Exciton-exciton annihilation occurs when the photoexcited carriers (excitons) transfer their energy to secondary electrons, which gain energy. Phonon emission is the process in which the excitons lose their energy into the lattice as heat. The conversion of light into excitons is dependent on the competition of these energy relaxation pathways. The process is greatly enhanced when the excitons transfer their energy into the creation of more carriers.

2.7 Photons and waveguides

Light is transmitted through a waveguide due to total internal reflection (TIR). When the propagating light strikes the boundary between the silicon and the silicon dioxide cladding material, it is reflected due to the difference in refractive indices. This is possible when the incident light strikes the boundary at an angle that is larger than the critical angle with respect to the normal of the boundary. The larger the angle is to the normal, the more light is reflected back into the waveguide until the angle at which TIR occurs. Because the light is channelled into the waveguides by the diffraction grating, the critical angle is always reached, and so light always propagates down the waveguide. This can be thought of much like a normal fibre-optic cable.

In general, bulk silicon shows weak nonlinearities. However, the cross-sections of waveguides are so small that the optical power density increases, which enhances the nonlinear effects. Light propagates through silicon waveguides under the effects of nonlinear optical phenomena, including interactions between photons and free charge carriers, the Kerr effect, two photon absorption (TPA) and the Raman effect. The nonlinearity enables photon interactions that allow for the passive transmission of light. Silicon is used for waveguides due to its intrinsic uniformity and transparency of light at near infra-red (NIR) wavelengths.

2.8 Silicon waveguides

Silicon waveguides work by total internal reflection of the light that is passed into and through them. This is achieved by a difference in refractive indexes of the silicon core (through which the light is guided) and the surrounding silicon dioxide cladding.[105] The high contrast of refractive indices between the silicon and oxide cladding material offers high photonic integration capabilities.[106,107]

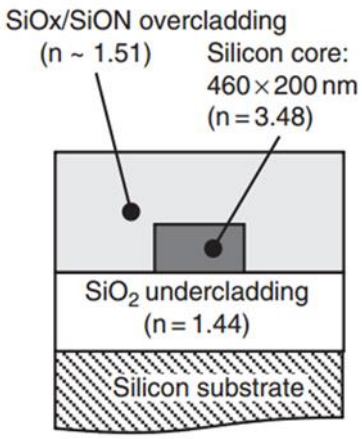

Figure 7: Cross section of a silicon waveguide used by Ohkawa et al.[108]

Figure 7 shows the cross-section of a waveguide and gives the dimensions and different refractive indexes used by Ohkawa et al. The buried oxide layer also gives natural confinement of optical waves vertically. As the cladding functions only as a reflecting layer, propagation of light only occurs in one direction.

An important factor of silicon waveguides for the purpose of this project is that not all of the light that travels through the waveguide remains within it; this is shown in Figure 8. There is an evanescent field of light surrounding the silicon core.

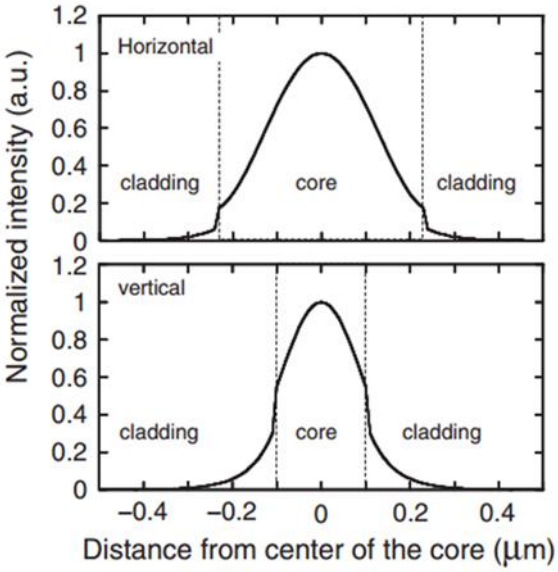

Figure 8: Intensity of light as a function of distance from the silicon core of a waveguide.[108]

Introducing an optically active material such as graphene into this evanescent field attenuates the light passing through a waveguide as some of the light is absorbed. Crowe et al. showed the attenuation experienced in a silicon waveguide is a function of both the height of the graphene from the waveguide and the length of graphene along it (shown in Figure 9).

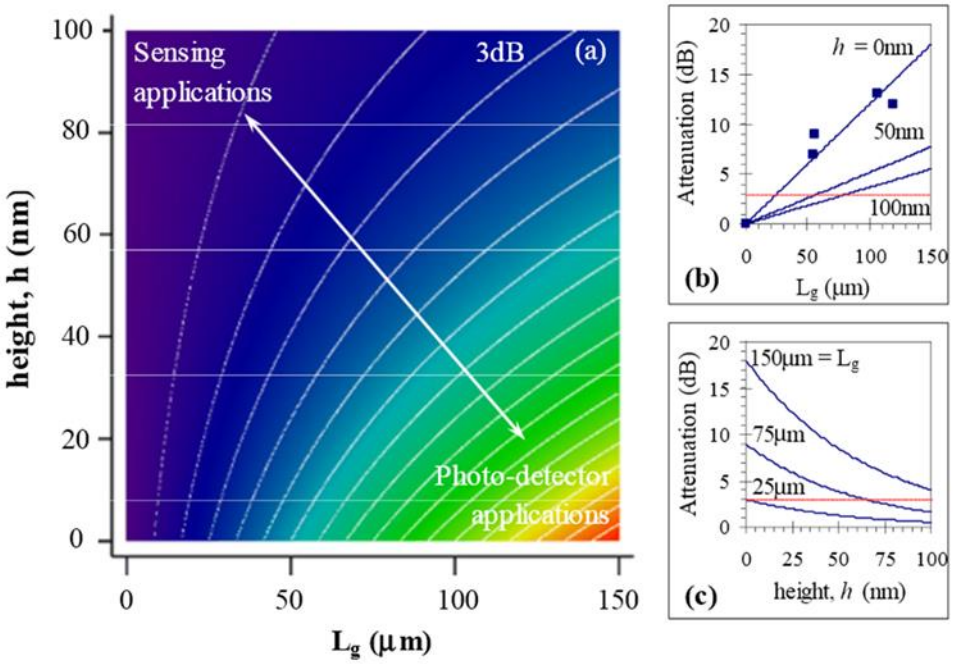

Figure 9: Crowe et al. (a) A contour plot showing attenuation, A_g, of light on a racetrack resonator as a function of the height of a graphene membrane from the waveguide, h, and the length of graphene along the waveguide, L_g, (blue – low, red – high, contour lines – 1 dB increment) . (b) Calculated Ag as a function of L_g for specific heights (h = 0, 50, 100 nm) along with their measured data (blue squares) and (c) calculated A_g as a function of height for specific lengths (Lg = 25, 75, 150 μm). The red dashed lines in (b) and (c) indicate the graphene (L_g, h) co-ordinates where the cavity resonance signal is attenuated by 3dB.[1]

Waveguides experience losses in signal strength in coupling the light from the input fibre and the grating on the chip, losses along the straight waveguide and losses due to curvature. The waveguide chips to be used in this project have grating couplers that channel a vertical light beam into the waveguide. Vertical coupling, as opposed to other methods of light-coupling, has a number of benefits. Vertical coupling requires less precise fabrication processes such as chip cleaving and polishing involved in end-on coupling. Lower losses are seen with near-vertical incidence of light onto a vertical grating coupler.[109] Also, vertical coupler gratings can be laid out in two dimensions which can offer more devices per chip in

a grid-like system, therefore more devices per chip and extra flexibility in design. Lower losses are observed in waveguides that employ vertical coupling as the devices do not need to span the entire length of a chip.

Investigations of propagation loss contributions have shown that scattering due to sidewall roughness dominates and as such, decreasing the height of the waveguide core results in significant decreases of propagation losses.[110] Propagation losses in waveguides can be reduced using optimized lithography and etch processes.[111] Other reasons for propagation losses include material limitations, such as free-carrier absorption, surface-state absorption and scattering, two-photon absorption, and defects.[112]

High-quality resonators are seen to have a high-quality factor, Q. A high Q means a sharp resonance which makes observation of small resonance wavelength shifts necessary for sensing applications easier.[113]

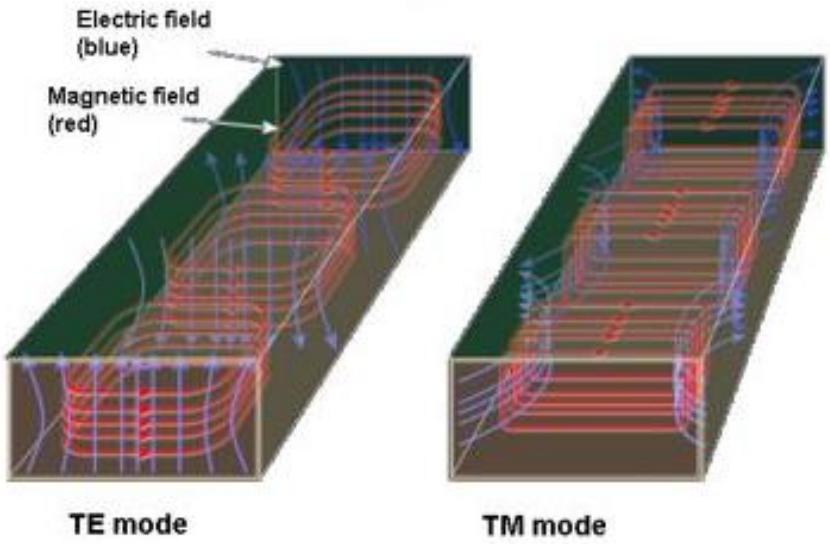

Figure 10: TE and TM propagation modes in a waveguide.[114]

Waveguides can support transverse electric (TE) and transverse magnetic (TM) modes but not transverse electric and magnetic (TEM) mode waves. In TE modes, the electric field is transverse to the direction of propagation, $E_z = 0$ and $H_z \neq 0$. In TM modes, it is the magnetic field that is transverse, and an electric field component is in the propagation direction, $H_z = 0$ and $E_z \neq 0$. The electric and magnetic fields of TE and TM modes are shown in Figure 10. There is a lower threshold frequency that must be exceeded in order for electromagnetic waves to propagate. This is known as the cut-off frequency, f_c.

2.9 Ring resonators

A ring resonator works by having a straight waveguide near to a ring waveguide. The light couples from the straight waveguide into the ring. The cavity of a ring resonator is in resonance when the light waves in the loop build up a circumferential phase shift that equals an integer times 2π. Therefore, larger rings will have more wavelengths that result in constructive interference within the ring, building a strong field.[115] After the light has propagated through the ring, some light couples back into the straight waveguide, interfering with the incident light. At resonance, no light is transmitted through the straight waveguide due to complete destructive interference when the propagation length around the ring is an integral number of wavelengths. This results in notches in the output spectrum at resonant wavelengths of the ring.

This makes the optical ring resonator an ideal notch filter, blocking the light at the resonant wavelength.

Having a ring resonator with a small radius of curvature is desirable to reduce the footprint of a device on-chip; smaller dimensions also have the potential to reduce power consumption, particularly in active devices.[116] However, it has been shown by Khan et al. that decreasing bend radii results in a near exponential increase in radiation losses.[117] Figure 11 shows the dimensions of a 70 µm radius ring resonator and the coupling gap between the ring resonator and bus waveguide.

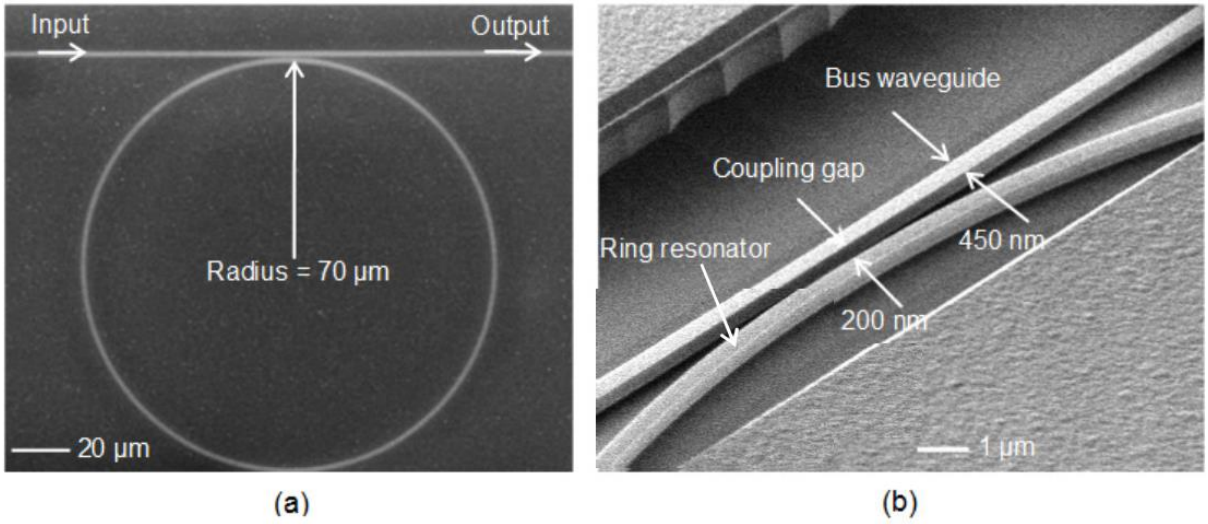

Figure 11: SEM images of (a) ring resonator with 70 µm radius, and (b) zoom view of the gap between the bus waveguide and ring resonator.[118]

2.10 Alternative waveguide materials

2.10.1 InGaAsP/InP and AlGaAs/GaAs

Monolithic integration (multiple circuits on a single chip) is possible using this crystalline semiconductor. The optimum wavelength range is 1.3 – 1.5 µm as these wavelengths offer the lowest losses in the optical fibres. Waveguides can be manufactured using epitaxial growth on an InP substrate or by etching. The waveguide structures are usually 1 – 2 µm in length. This is possible due to high refractive index contrast.

AlGaAs/GaAs waveguides operate in the 0.8 µm wavelength range. They are also produced using similar methods to the InGaAsP/InP waveguides but with a GaAs substrate.

Both with such small dimensions have the same problem of difficulty in light coupling from an optical fibre to the waveguide.

2.10.2 Glass

Glass waveguides can be produced either by deposition or diffusion. Deposition involves either chemical vapour deposition (CVD) or flame hydrolysis (FHD) of silica on a substrate (normally silicon). Due to low index contrast, the devices are relatively large. However, their size allows easier coupling with optical fibres. Glass waveguides tend to operate in the near infra-red range of wavelengths.

2.10.3 $LiNbO_3$

Lithium niobate is anisotropic and offers strong electro-optical and acoustic-optical properties. A diffusion process is used to manufacture these waveguides. The anisotropy leads to components displaying dependence on polarisation. These waveguides operate in the range of wavelengths 1 – 2 µm.

2.10.4 Polymers

Poly (methyl-methacrylate) (PMMA) is a glassy polymer that is used in waveguides, most commonly in the wavelength range 600 – 1550 nm.[119] Polymer materials for use as waveguides are favourable due to their relatively lower cost compared to semiconductor waveguides. These waveguides can be produced by femtosecond laser micromachining[120] or applying an electric field to modify the surface profile.[121]

3. Experimental

3.1 Membranes on waveguides

3.1.1 Optical measurements

Figure 12 shows the optical measurement setup and the path that the light beam takes. A broadband light source (1) is shone through an aperture (2) which directs the light onto a 50% reflective mirror (3) that directs light into a diffraction grating on one side of the waveguide (4). The light then travels down the waveguide, at the bottom of a micro-cavity etched into the silicon oxide cladding, where it is attenuated by the membrane above (under pressure) and then leaves the waveguide through a grating on the other side. The beam then travels back through the 50% reflective mirror, reflected through 90° on a mirror (5), to a beam splitter (6). Half of the light goes to a camera (7) which is used to view the waveguide to align the beam to the first diffraction grating initially, and the other half of the light goes to an optical spectrum analyser (8) which is connected to a laptop with software that produces a spectrum. A spectrum is taken before and after pressure is applied so that the attenuation can be determined.

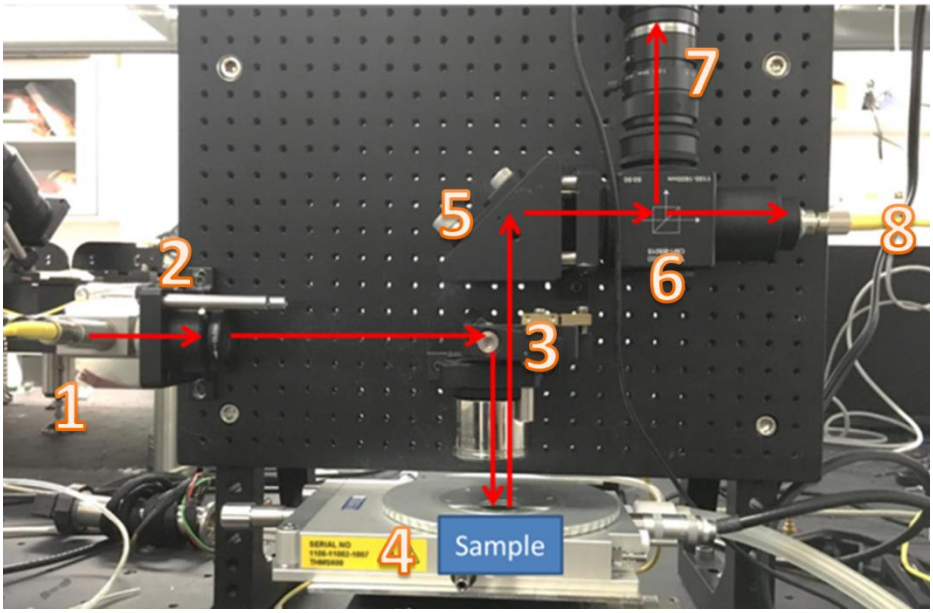

Figure 12: Optical measurement setup.

On one chip, there are many waveguide structures. Figure 13 shows a schematic of part of a waveguide chip. The larger rings are 50 µm radius, and the smaller rings are 25 µm radius. Figure 14 shows an optical image of 4 ring resonators, 2 with windows etched into the cladding material.

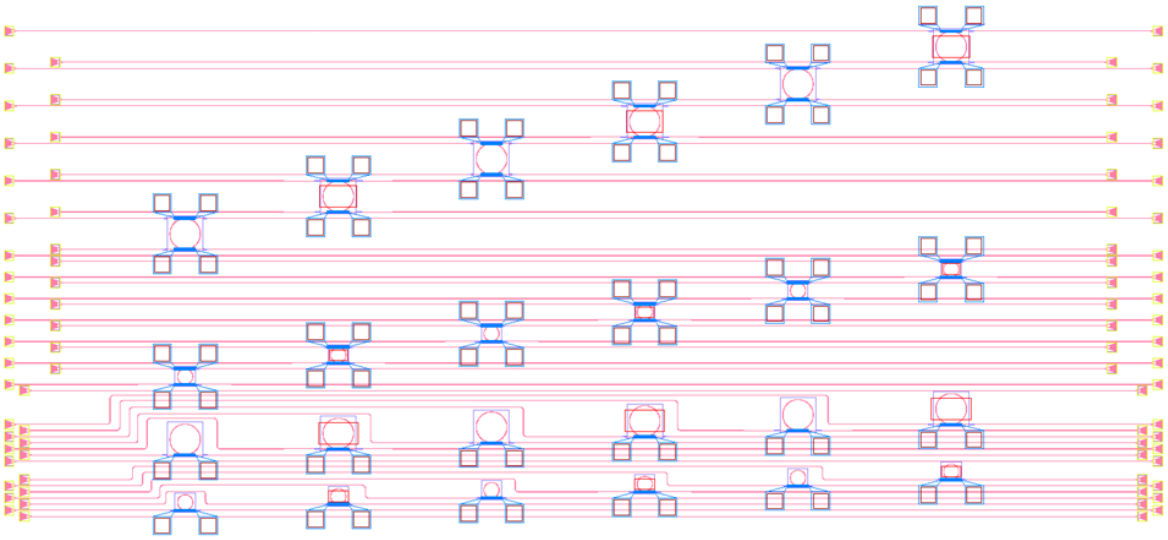

Figure 13: Schematic of an example waveguide chip.

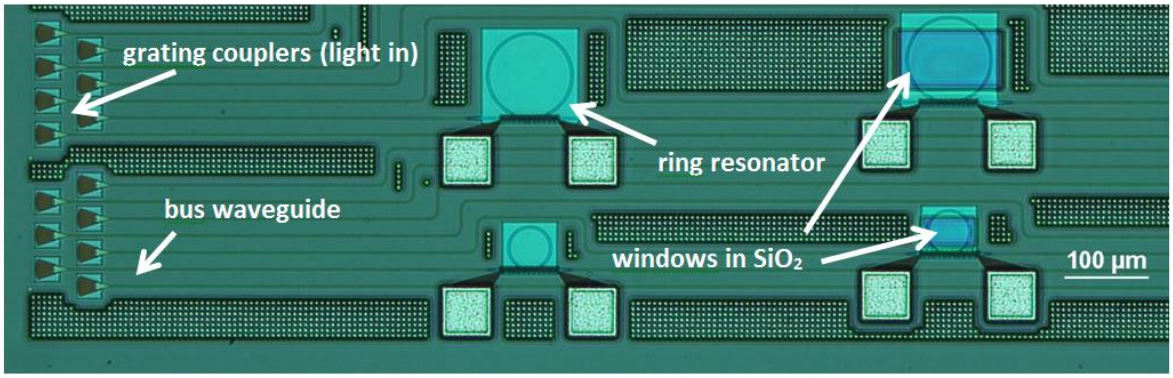

Figure 14: Optical image of part of the initial waveguide system (5x magnification).

3.1.2 Waveguide design changes

Initially, the supplied waveguide chips for the project were not designed for membrane interfacing. When waveguide chips are fabricated, academic research groups will often share sections of a chip to make them economical when paying for fabrication. There were only six ring resonators that had windows in the SiO_2 cladding that could allow for membranes to be placed onto the surface of ring resonators. These were located in a corner, as shown in Figure 15, making transfers very awkward.

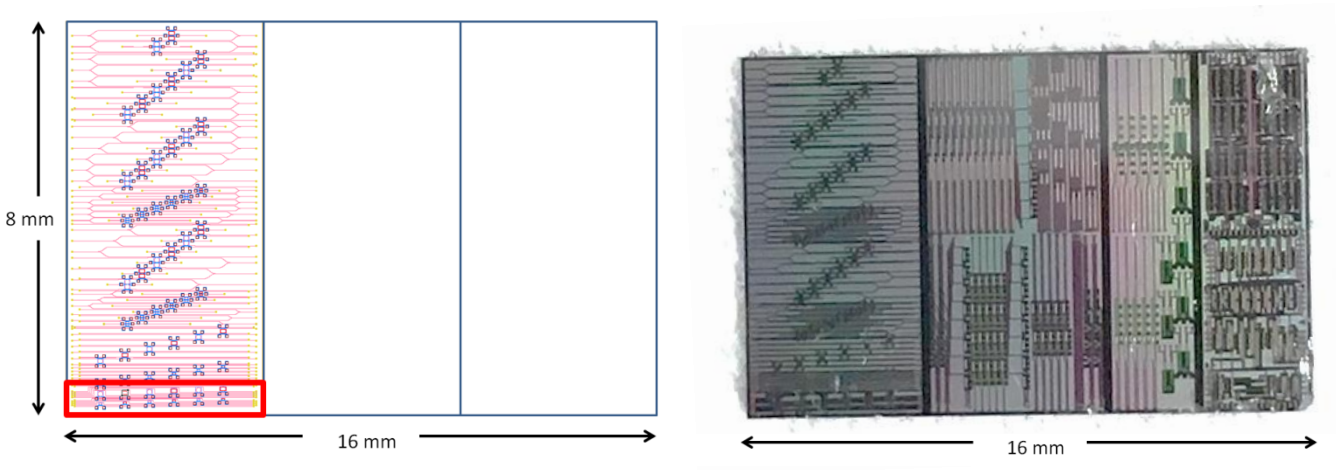

Figure 15: Left - schematic of the waveguide chip for this project (red box indicates location of usable ring resonators). Right - image of the actual chip.

As well as this, the chips had additional functionality such as heaters and heat pads which had top layers of aluminium. These would ultimately impede the success of membrane transfers onto the chips as they would act as vertical barriers, reducing adhesion.

In an effort to reduce the impact of the heaters and heat pads, the waveguide chips were placed into an aluminium etchant and then washed in IPA and dried.

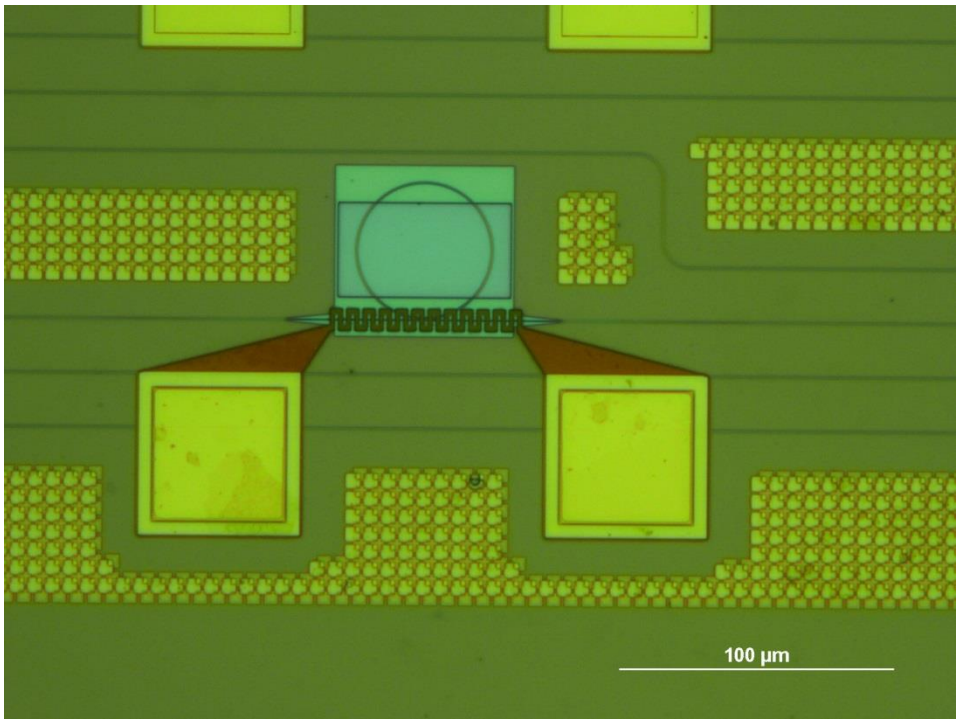

Figure 16: Optical image showing a single ring resonator after aluminium etching (20x magnification)

The etching introduced contamination to the surface of the chip and did not remove the layers of the heater pads beneath the aluminium, as shown in Figure 16. These initial waveguide chips were used in the proof of concept experiment with GO. In order to improve the efficiency of experimentation, a method of multiple transfers was developed (outlined in section 3.2.4). This proved to be less effective than anticipated, and so for greater repeatability of transfers, the waveguide chips needed to be redesigned.

This first redesign was fabricated by Cornerstone (Capability for OptoelectRoNics, mEtamateRialS, nanoTechnOlogy aNd sEnsing), "…a license free, open source Silicon Photonics rapid prototyping foundry…"[122] run by the Silicon Photonics Group at the University of Southampton.

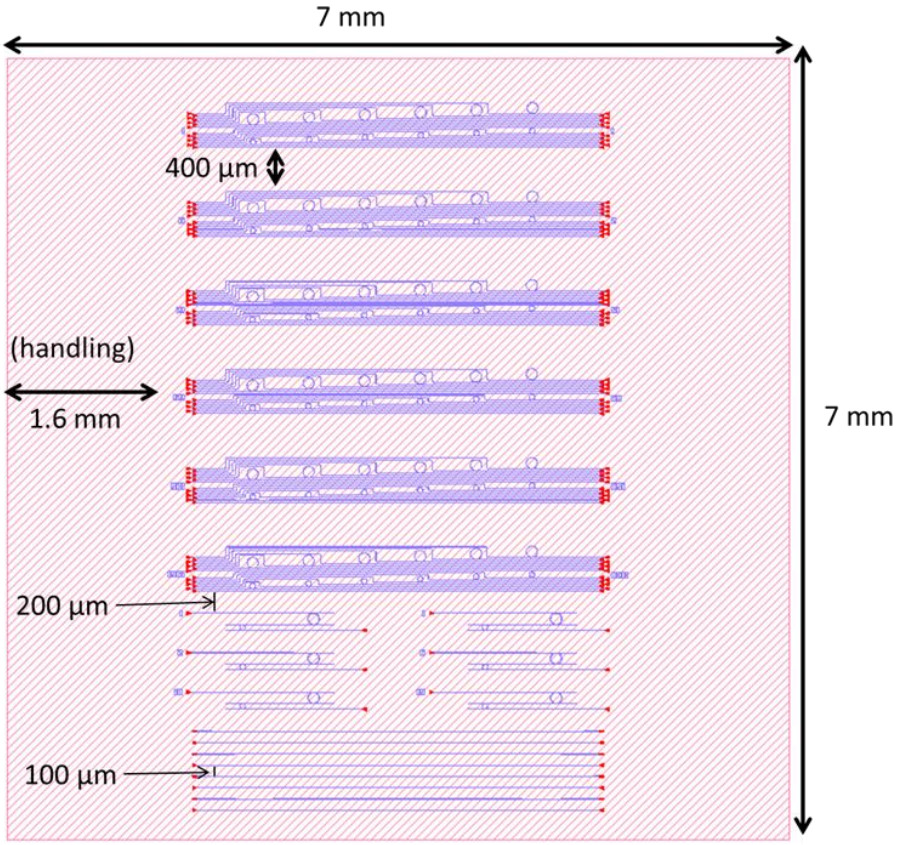

Figure 17: First redesign of the waveguide chip.

A new waveguide design (Figure 17) was developed to work better for the requirements of transferring 2D materials onto waveguides. The original set of multiple single ring resonator systems was used and repeated with more spacing to allow for easier membrane transfers. A set of Vernier ring systems was added to trial the tracking of single peaks as the Vernier system can act as a peak filter. At the bottom of the new design, a set of straight waveguides were added with two different grating couplers used to allow for comparisons to be made between the two. The fabrication of the new design was outlined in advance. It

was decided that the new designs would be fabricated without a top silicon oxide cladding layer to allow for more precision in membrane placement. The new design also differed from the previous chip in that the new design does not have heating elements, heater pads and other metallic architecture close to the rings as they are obsolete at this stage of the project.

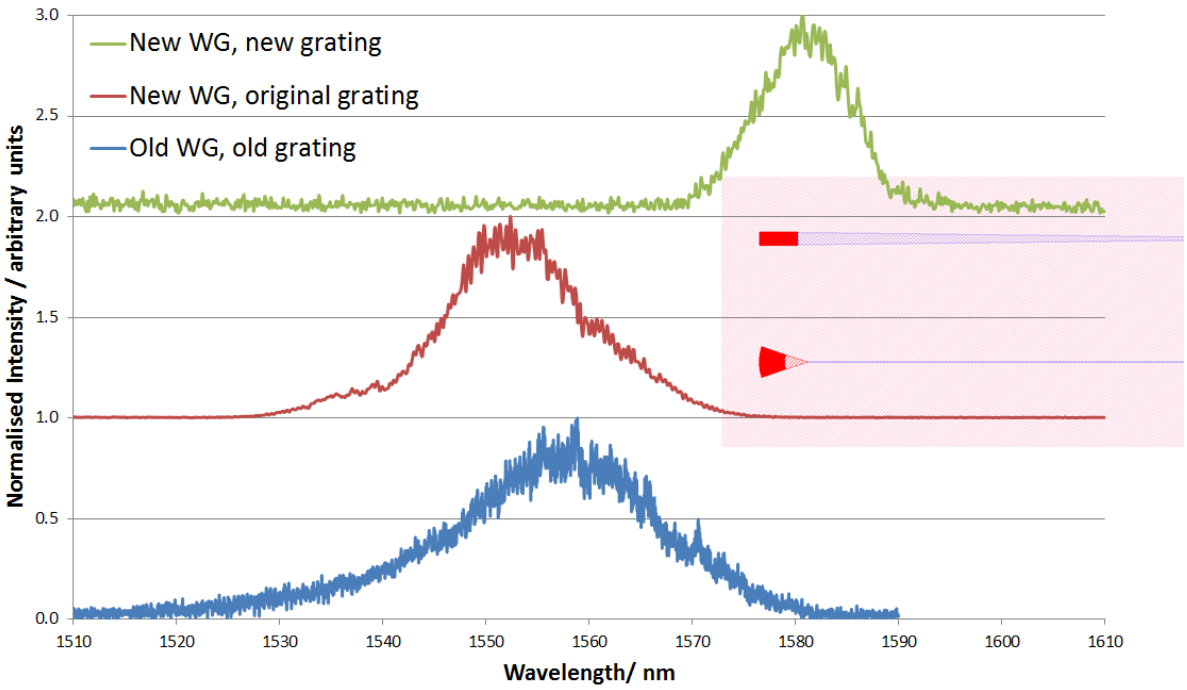

Figure 18: Optical data showing iterations of grating couplers. Inset right, top: new grating coupler design, bottom: original grating coupler design.

Figure 18 shows the peaks transmitted through the two different grating coupler designs. The new style of grating coupler offered a sharper peak, which is desirable. However, due to the new wavelength of the transmitted signal, the light exiting the waveguides could not be seen on the camera of the optical measurement set up. Being able to see the transmitted light on the display is critical for alignment of the waveguide grating couplers. Without

visual feedback alignment is impossible. For that reason, the original grating style was kept for the next iteration of the waveguide design.

Figure 18 also shows a less noisy and sharper peak on the new waveguide compared with the previous waveguide. This can be attributed to the removal of peripherals on the chip, such as heaters and heater pads.

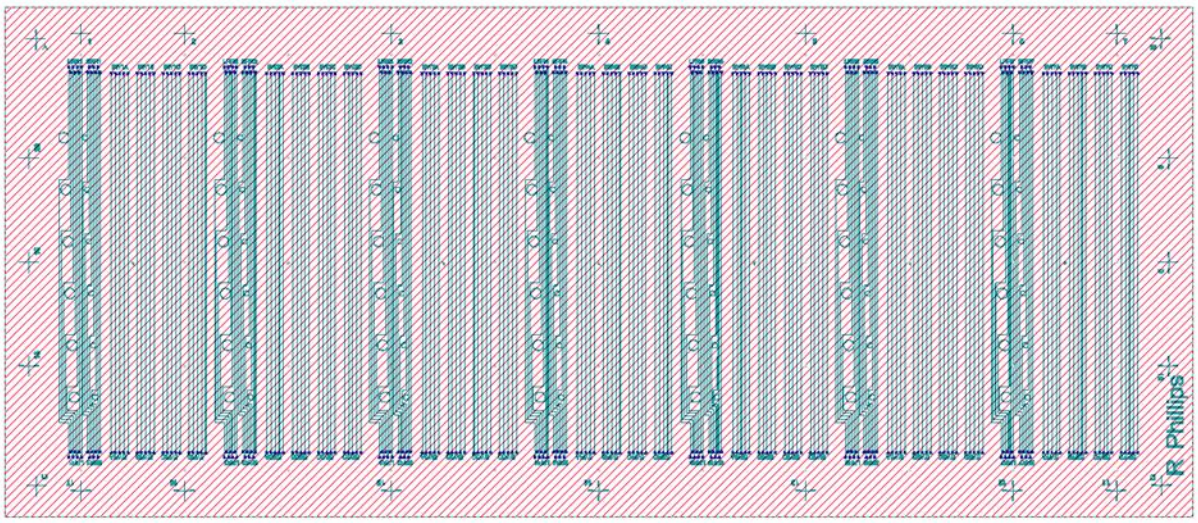

Figure 19: Final waveguide chip design.

It was postulated that optical measurements gained from adjusting the interaction length of a membrane along a bus waveguide rather than on ring resonators would be more straightforward to analyse with fewer variables to consider. For that reason, the final waveguide chip (Figure 19) was designed to contain multiple groups of bus waveguides. There was no cladding on this new chip. It was postulated that a thin PMMA layer could be used to coat the waveguide chip, and then electron beam lithography (EBL) could be used to open windows in the PMMA on which membranes could be transferred.

3.2 Fabrication of rGO/Parylene-C membranes

3.2.1 Substrate preparation

Substrates are generally prepared for transfers using the following method:

1) Wafers are scribed and broken into useable sizes, appropriate for the transfer being undertaken (typically 2 x 2 cm squares).
2) The pieces of substrate are quickly rinsed with acetone to remove the bulk of any photoresist that has been used as a protection layer up until this point, and then it is fully submerged in a beaker of acetone which is placed in a sonication bath for 5 minutes to give a deep cleaning effect.
3) The substrate is then rinsed with isopropanol (IPA) before being submerged in a beaker of IPA, which is then sonicated for 5 minutes.
4) The substrate is rinsed with deionised (DI) water.
5) A flow of nitrogen is used to dry the substrate.

However, in the case of waveguide chips as a substrate, the same steps are followed apart from the chip is merely submerged in acetone and IPA rather than being sonicated whilst submerged due to the delicate nature of the structures on the chip and the fact that sonication can be quite aggressive.

3.2.2 Polymer-supported transfer in DI water (fishing)

In order to transfer the CVD graphene from the copper onto a bare substrate, a method developed by several groups is used.[123,124] This process is pictorially described in Figure 20.

1) The copper foil is cut to the size required in the transfer using scissors and then gently flattened by hand between 2 clean-room paper towels.

2) A thick polymer (PMMA 950 8% in anisole) is spin-coated onto the copper foil at a rate of 3000 rpm for 60 seconds. This is then baked on a hot plate at 115°C for 5 minutes to drive off the solvent inside the PMMA solution.

3) If the CVD graphene is on both sides of the Cu foil, then the side without a polymer coating is plasma etched for 45 seconds to remove the unwanted area of graphene.

4) 25 g of ammonium persulfate (APS) is dissolved in 1000 ml of deionised (DI) water. This dilute solution is used to dissolve the copper for 3 hours, leaving a layer of graphene-coated in polymer floating at the surface. Using a drip and drain setup (10 ml/min for 3 hours), the etchant is replaced with DI water.

5) The polymer composite is fished from the DI water with a clean substrate and dried above a hot plate at 50℃ for 1 hour.

6) To ensure the membrane conforms to the topography of the substrate, the sample is then heated for 2 minutes at 130℃. It has been observed that further heating of the polymer-graphene membrane limits the removal of the polymer in the following step.

(For devices requiring small areas of CVD graphene, it is possible to use thinner polymer films (3% PMMA 495 in anisole). This allows the film to be almost completely removed in the furnace directly after step 6, giving a higher yield[125], leaving only small PMMA residues behind.)

7) The substrate is then immersed in acetone for 1 minute to remove the bulk of the polymer, and then it is transferred to a Petri dish (without letting the sample dry) full of fresh acetone for 30 minutes before being put in a new Petri dish of fresh acetone for 6-8 hours to dissolve any remaining polymer.

8) The sample is then transferred into another dish filled with hexane, without being allowed to dry, for 1 minute before being dried completely in air (can be aided with a flow of nitrogen).

9) Finally, the substrate is annealed at 350°C in a furnace with a flow of hydrogen and argon for 2 hours to ensure suspended graphene features are not exposed to the surface tension of acetone during its evaporation at atmospheric pressure.

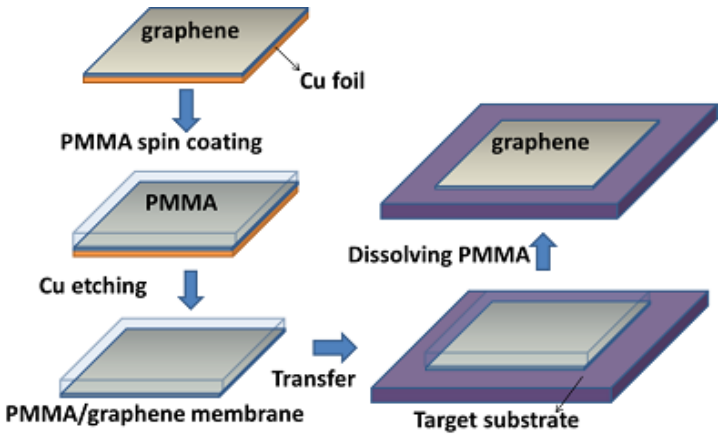

Figure 20: Flowchart of CVD graphene transfer process.[126]

3.2.3 Polymer-assisted transfer in air

1) CVD graphene is coated in PMMA as per Table 1. The PMMA coated CVD graphene is then baked on a hot plate at 115° for 5 minutes.

Table 1: PMMA thicknesses required for approximate graphene transfer sizes and respective spin coating recipes.

Shortest length of transfer area	Total PMMA thickness	Recipe
3 mm – 5 mm	200 nm	3% 950 3000 rpm 1 min
5 mm – 10 mm	800 nm	8% 950 3000 rpm 1 min
10 mm - 40 mm	1600 nm	8% 950 3000 rpm 1 min (x2)

2) A 2-3 layer polyimide (Kapton) tape window is cut. Water-soluble tape tabs are added that are 1 mm larger than the required transfer area. This is then stamped onto the polymer side of the CVD-Cu foil. A diagram is shown in Figure 21.

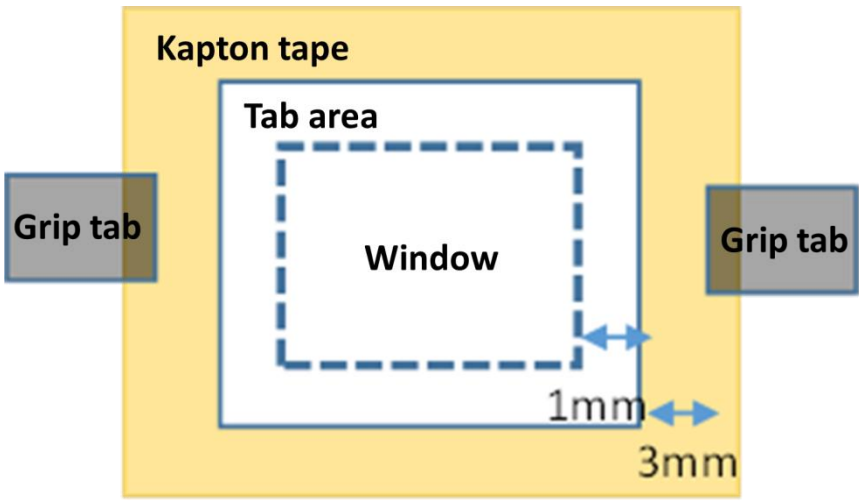

Figure 21: Diagram of tape setup for polymer-assisted graphene transfer in air.

3) The tape-polymer-CVD-Cu window system is placed in APS (as per step 2 of the fishing transfer process), but the window system must be transferred carefully handling the soluble tape handles.

4) The tape window system is suspended between two glass slides on a hotplate at 50°C for 30 minutes to dry.

5) The final target substrate is heated to 130°C, and the window system is stamped down on top.

6) A sharp tool is used to release the PMMA films from the window system at 130°C.

7) The PMMA layer is removed from the graphene as per steps 6 - 9 of the fishing transfer process.

3.2.4 GO preparation

This method was developed especially for this project, adapting transfer methods described for CVD graphene. The new method is shown in Figure 22.

GO was prepared in solution with water using a modified Hummers method. The resultant GO was then diluted in solution with water to different concentrations in preparation for spin coating.

1) The dilute GO was dropped using a pipette onto a clean Si/SiO_2 substrate (approximately 2 cm x 2 cm). The substrates were spun at 1000rpm for 1 minute and then allowed to dry in a desiccator.
2) Aluminium was deposited on top of the GO using a thermal evaporator to a thickness of 70-100 nm.
3) S1805 negative photoresist was spun onto the aluminium layer and then baked at 115°C for 5 minutes.

4) A photolithography mask was designed to produce rectangular strips. This mask was exposed on a laser writer.

5) The photoresist was developed in MF319 developer for 45 seconds, leaving strips of photoresist patterned above the aluminium layer. The sample was then rinsed in DI water.

6) The sample was submerged in aluminium etch for 30 seconds to remove the aluminium layer that was not protected by the developed photoresist strips. Then the sample was rinsed in DI water to remove any residue.

7) The sample was then submerged in acetone to remove the photoresist above the aluminium strips. And then rinsed again in DI to remove residual acetone.

8) The sample was then plasma etched for 2 minutes to remove all GO that remained uncovered by the aluminium strips.

9) The remaining strips of aluminium covering the GO strips were then removed by submerging the sample in aluminium etch for 30 seconds. DI water was used to rinse away residual aluminium etch.

10) PMMA 950 3% was then spun onto the sample and baked as done for the CVD transfers mentioned previously.

11) A tape window was then created as previously. The sample and tape window was then placed in a Petri dish of potassium hydroxide (KOH) etch for 5 hours to etch away the SiO_2 layer beneath the GO. Once the SiO_2 layer had been etched, the window system floated to the top of the dish leaving the Si substrate at the surface. DI water was then used to rinse any residual KOH.

12) The GO strips were then dried and transferred directly onto windows etched above ring resonator waveguides using the same process as the polymer-assisted transfer of CVD described earlier. The PMMA layer was not removed at this stage.

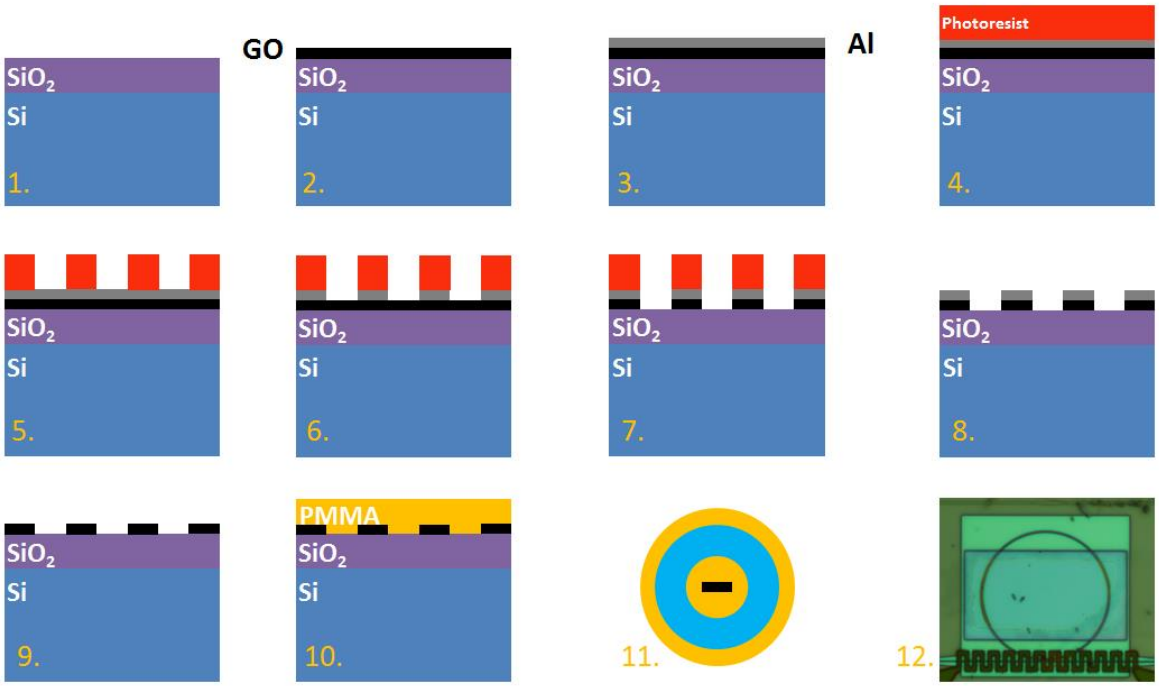

Figure 22: Flowchart of described GO preparation.

An aluminium etch mask was used instead of a photoresist due to the long plasma etch time required to remove GO. Such long etch times cause photoresist masks to cross-link, making them insoluble in acetone.

To characterise the GO using AFM a scratch was made through the membrane so that a thickness measurement could be made comparing the membrane height to the reference point on a flat, blank substrate; a reference image showing the scratch in the GO is shown in Figure 23.

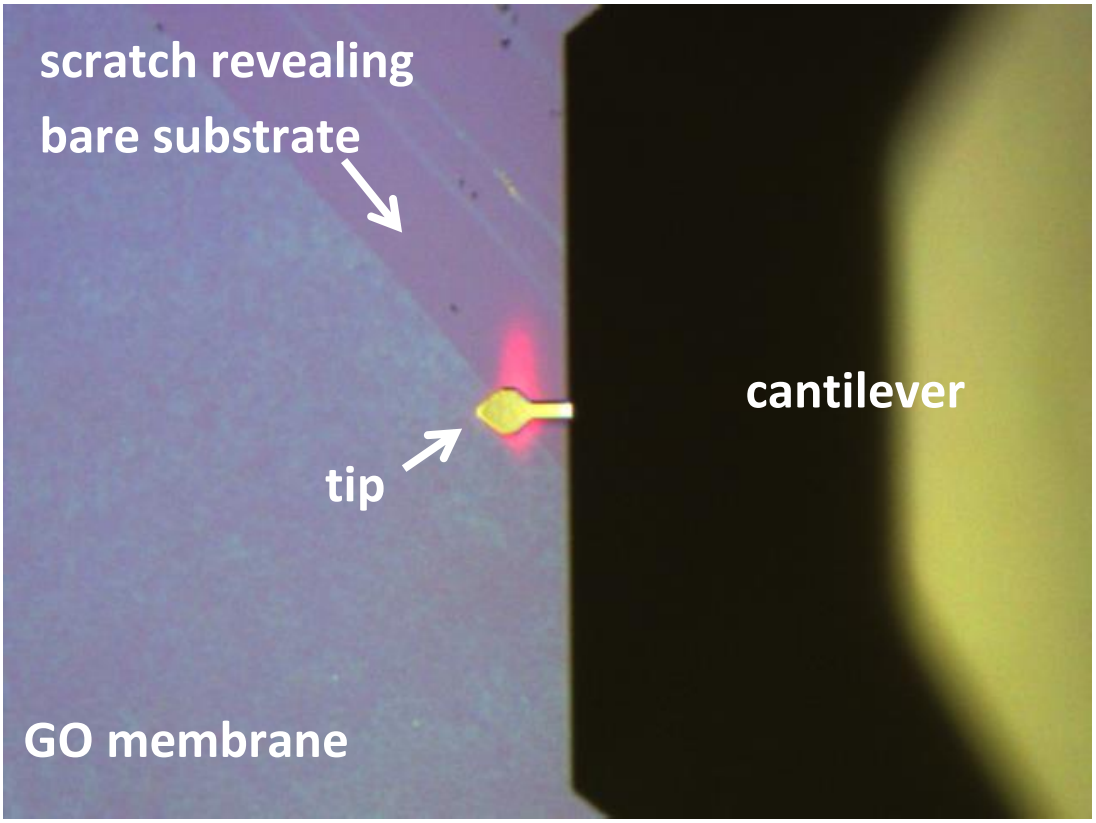

Figure 23: Reference image taken during AFM showing scratch made in GO membrane.

The previous method of GO transfer involved the use of a sacrificial aluminium layer. This process can result in a messy residue of aluminium from the etching process, shown in Figure 24a. A new method was developed to transfer GO without the need for aluminium, resulting in cleaner transfers, shown in Figure 24b. The method developed also allows for multiple strips to be placed onto waveguides in one transfer. A system was developed for the waveguide chips such that six transfers could be performed in the same process.

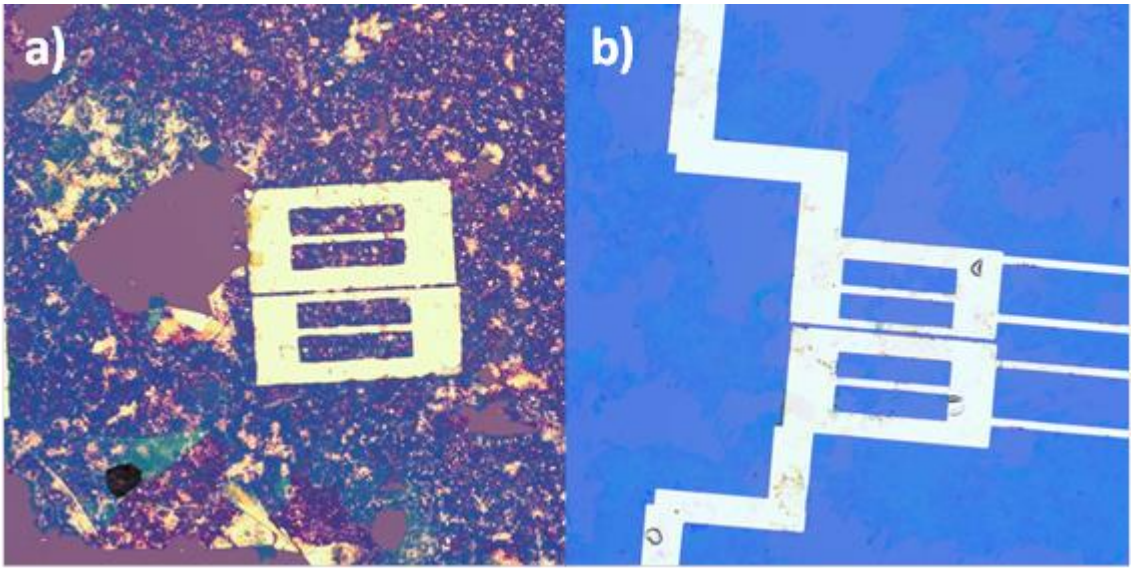

Figure 24: a) Optical image showing aluminium residue surrounding a polymer mask for GO transfer. b) Optical image showing a polymer mask covering GO without processing residue.

The new method involves the following steps:

1) Spin coat GO onto SiO_2/Si substrate.

2) Spin coat S1813 photoresist on top of GO.

3) Expose the designed pattern with a laserwriter.

4) Develop the photoresist in MF-319 developer solution.

5) Coat the sample in PMMA.

6) Apply a window made from SU8 polymer.

7) Transfer six strips simultaneously onto waveguides.

A schematic for the pattern and how the transfer strips align with the useable (no SiO_2 cladding) ring resonators is shown in Figure 25.

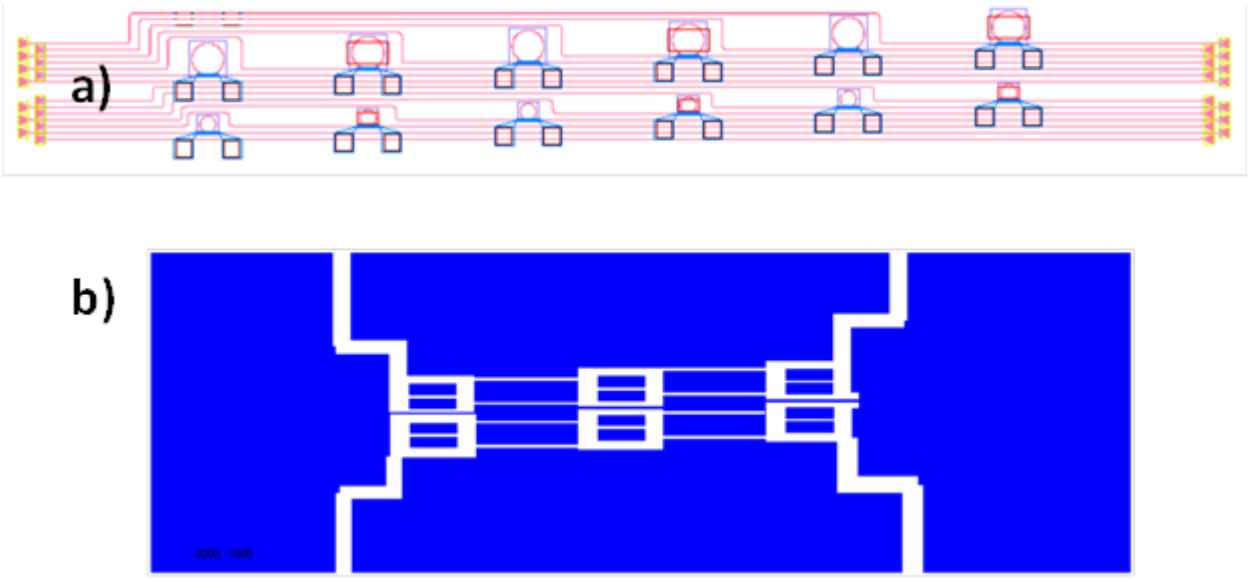

Figure 25: a) Schematic layout of the useable ring resonator systems – the red boxes over alternate rings denote a window into the SiO_2 cladding. b) Transfer design for simultaneous transfer of 6 strips.

SU8 windows were developed to surround the transfer system shown in Figure 25b. The previous method used metallic rings to transfer the GO strips individually. The SU8 polymer is less rigid, thinner and has the potential to remain on-chip for measurement, which means that the strips are less likely to be damaged as the window does not have to be prised away from the membrane.

An image of a SU8 window next to the old-style waveguide chip is shown in Figure 26. The internal dimensions of the window allow complete coverage of the useable area of the old-style chips.

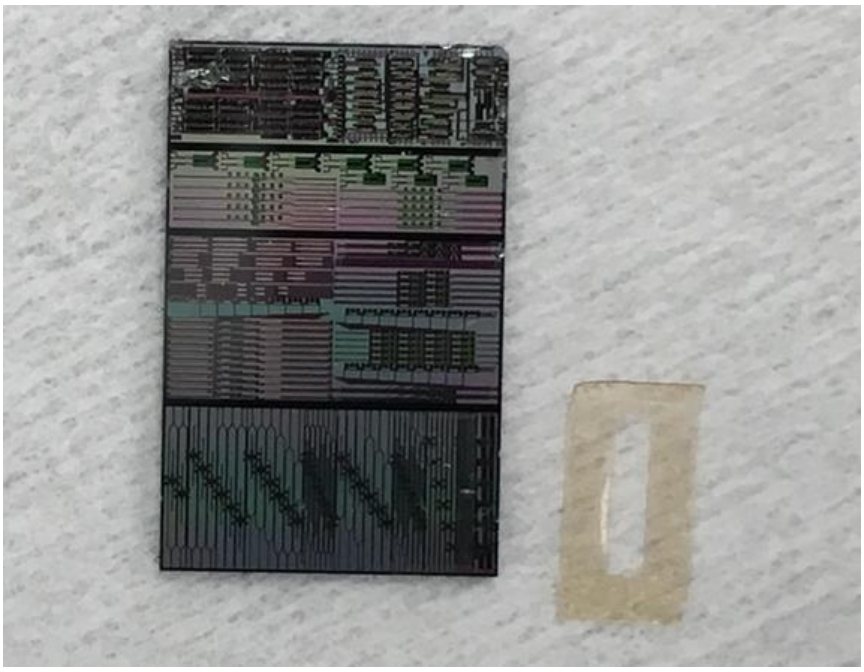

Figure 26: Image of a waveguide chip next to a newly fabricated SU8 transfer window.

This method was very time-intensive and often did not result in successful transfers. This led to the development of the previously mentioned waveguide design changes (section 3.1.2).

Following the final waveguide changes, a more efficient transfer process was developed (outlined in section 3.2.8).

3.2.5 rGO preparation

GO was spin-coated as described previously onto 4" Si/SiO_2 wafers. This was done using three different concentrations of GO.

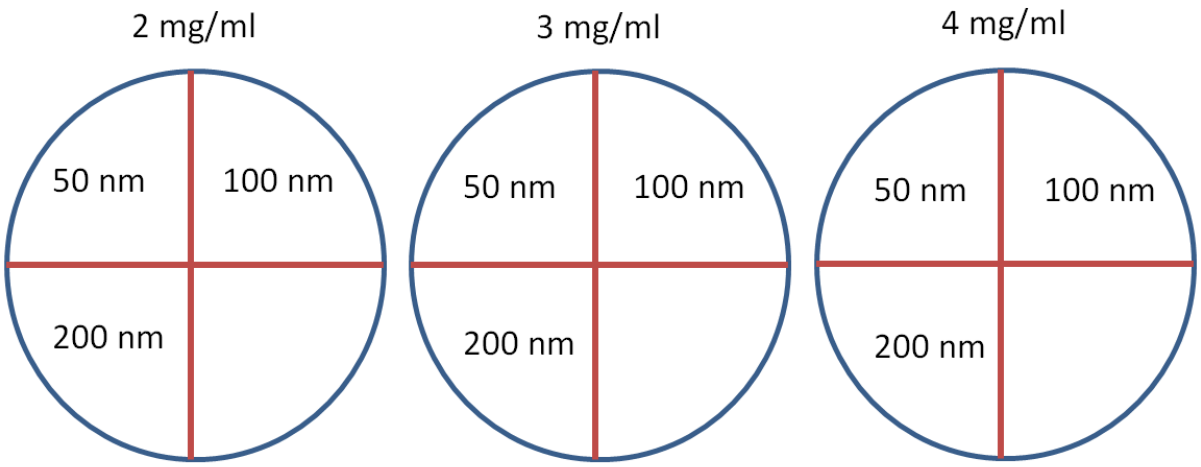

Figure 27: Diagram showing breakdown of SiO_2 wafers for rGO membrane Parylene-C coating. The targeted Parylene-C thicknesses would be 50, 100 and 200 nm.

After drying in a desiccator for 24 hours, each wafer was cracked into four pieces using a diamond-tipped scriber, as shown in Figure 27. This was to allow each thickness of rGO to have three thicknesses of Parylene-C deposited to create nine composite membrane thicknesses. The wafer had to be split before reduction to allow the pieces to fit into the furnace tube.

The wafer pieces were held in quartz boats and placed in the centre of the furnace tube shown in Figure 28.

Ar/N_2 gas, in a 50:50 ratio, was flowed through the furnace tube at a rate of 0.15 L/min.

The furnace was set to ramp up in temperature to 1000°C at a rate of 5°C/min. The furnace was set to hold the temperature at 1000°C for 30 s before ramping back down to room temperature at 5°C/min.

Figure 28: Furnace with ceramic tube used for reduction of rGO.

The reduction was confirmed through AFM of scratches in the GO before reduction (Figure 29) and after reduction (Figure 30) due to the significant decrease in membrane thickness.

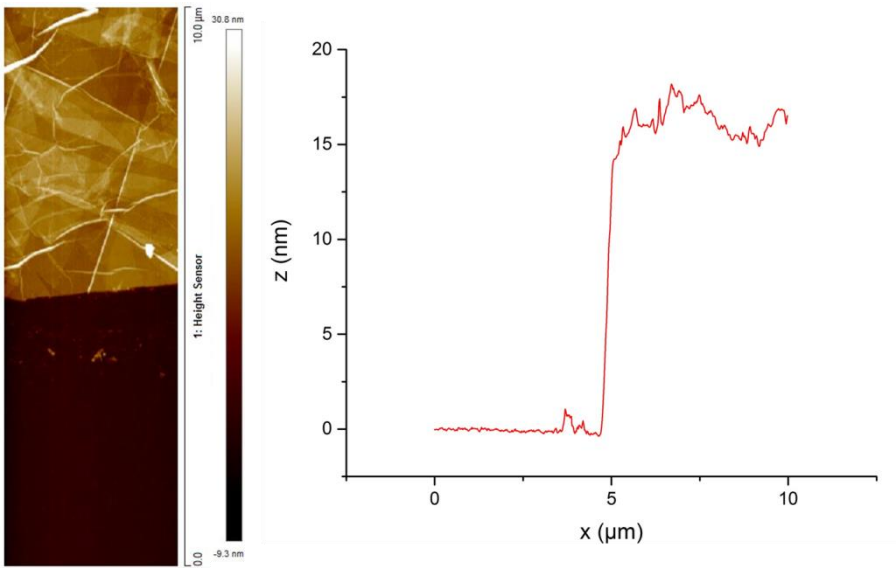

Figure 29: AFM cross-section of GO before reduction - 16.0 nm thick. The bottom of the red line shows the flat SiO2 surface with the sharp incline as the side of the membrane before the rough texture of the surface of the membrane. This roughness is due to folding/ripples of the GO flakes.

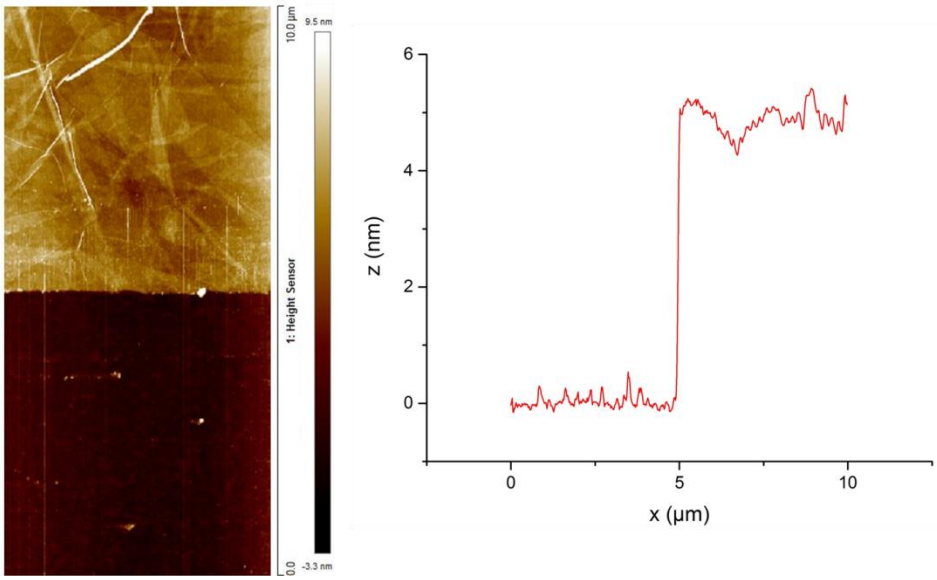

Figure 30: AFM cross-section of resultant rGO – 4.88 nm thick.

Electrical testing was carried out using a 4 point probe set-up. This helped to confirm a successful reduction due to the significant decrease in sheet reduction from ~800 MΩ per square for GO to ~7 kΩ per square for rGO.

3.2.6 Parylene-C CVD coating

The Parylene-C coating system used was an SCS Labcoater® 2 Parylene Deposition System supplied by Speciality Coating Systems.

The system works through a 3 stage process that results in a Parylene-C coating of uniform thickness being deposited onto the target substrate.

1. Vaporisation: The raw material, dimer, is heated in vacuo and vaporised into a dimeric gas.
2. Pyrolysis: The gas is then pyrolyzed to cleave the dimer to its monomeric form.
3. Deposition: In the room temperature deposition chamber, the monomer gas deposits on all surfaces as a thin, transparent polymer film.[127]

The final thickness is dependent upon the mass of dimer that is vaporised. Figure 31 shows the thicknesses gained from multiple depositions, measured using a Dektak Profilometer.

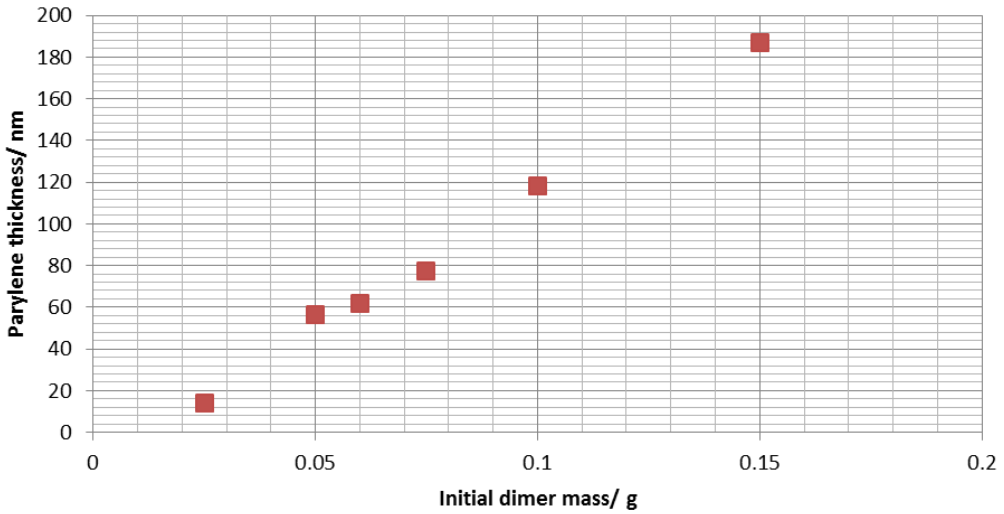

Figure 31: Graph showing Parylene thickness vs dimer mass.

Once the coater had been evaluated for the coating thicknesses, rGO on Si/SiO_2 wafer substrates were coated with targeted Parylene-C thicknesses of 50, 100 and 200 nm.

3.2.7 SiO_2 hole etching

In order to etch holes into SiO_2, an aluminium mask had to be patterned:

1. A 50 nm layer of aluminium was evaporated onto a 1000 nm SiO_2/Si substrate 20 mm x 20 mm.
2. S1805 photoresist was spin-coated on top of the aluminium layer.
3. The designed pattern was exposed with a laserwriter
4. The photoresist was developed in MF-319 developer solution – 15 s to develop the photoresist and an extra 135 s to etch through the aluminium – 150 s total.
5. The remaining S1805 photoresist was washed away with acetone and cleaned with isopropanol (IPA).

A dose test was required initially to find the optimum power setting on the laserwriter for the holes to be clearly resolved. Optical micrographs are shown in Figure 32; the optimum power was found to be 635 mJ/cm^2.

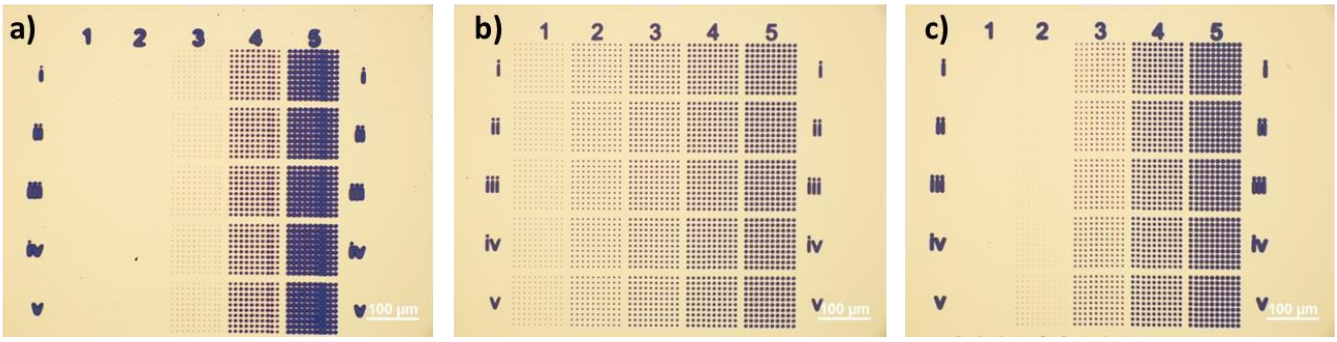

Figure 32: Optical micrograph of photolithography dose test to determine the best power for laserwriting. The yellow areas are the aluminium mask, and the purple areas are silicon dioxide. a) 625 mJ/cm^2 b) 635 mJ/cm^2 - optimum power setting c) 645 mJ/cm^2

The next step was to perform deep reactive ion etching (DRIE) to etch cavities upon which to suspend membranes.

An Oxford Plasma Lab 100 system was used with CHF_3 and Ar gases.

Ultimately, this method of fabrication proved to be time consuming and unrepeatable, with a lot of contamination being added to the substrates during processing. As such, a research group at the Karlsruhe Institute of Technology was tasked with fabricating hole structures. They provided over one hundred chips with hole structures on them, using capabilities that were not available at the NGI. These holes need further deepening, which was done using reactive ion etching (RIE). The holes were deepened to ~900 nm (height map shown in Figure 33) to improve the likelihood of successful membrane suspension.

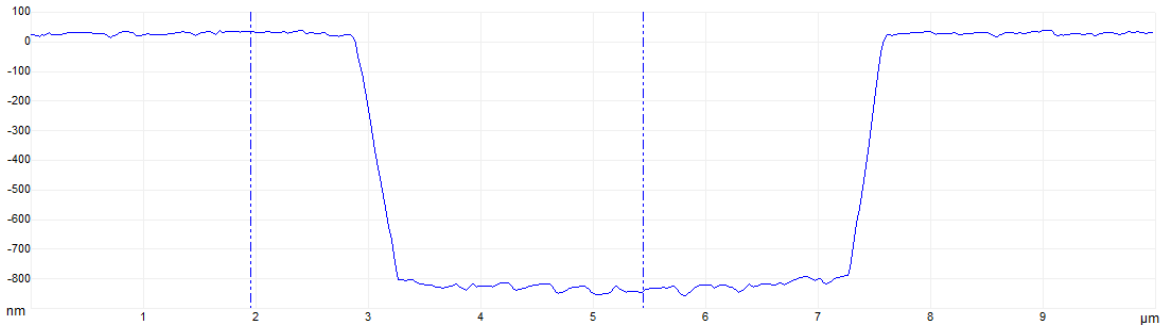

Figure 33: AFM height map of a fabricated hole in SiO_2.

3.2.8 rGO/Parylene-C membrane transfer process

The rGO/Parylene-C composite membranes were held on Si/SiO_2 substrates. In order to remove the membranes from the substrate, it was first cut into small pieces ~ 8 mm^2 before being placed in a KOH solution. The KOH solution etched away the SiO_2 layer of the substrate such that the membranes floated on the surface of the solution leaving the Si wafer at the bottom of the dish. To remove KOH from the underside of the membranes, they were fished from the solution using a glass slide and put into a dish of DI water for 30 minutes. This was repeated three times. Then the membranes were fished out using the substrates with hole structures (Figure 34b, i). They were then placed in a desiccator for 24 hours.

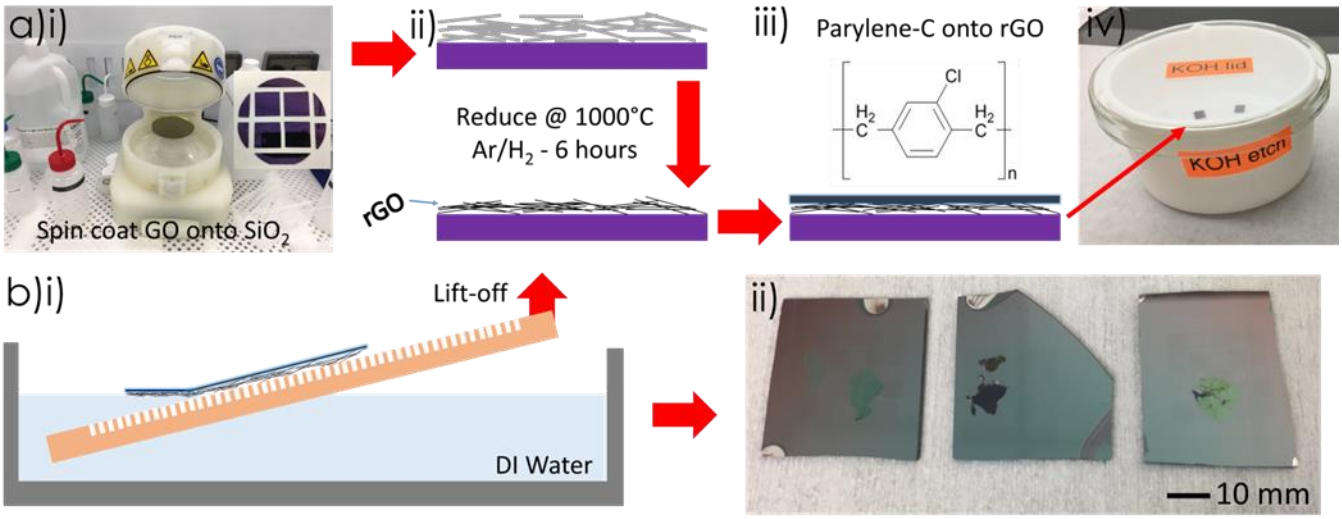

Figure 34: Flowchart of fabrication process. a)i) GO spin-coating ii) Reduction of GO Iii) Chemical vapour deposition (CVD) of Parylene-C onto rGO iv) KOH etch of SiO_2 b)i) Membrane lift-off onto hole structures. ii) rGO/Parylene-C membranes on holes.

This method resulted in many creases in the membranes and contamination from trapped DI water shown in Figure 34b, ii. A new technique was developed to resolve this.

Strips of wafers (~ 5 mm x 12 mm) with the rGO/Parylene-C membranes on them were attached to windows created with blue adhesive tape shown in Figure 35. These would float on the surface of the KOH solution. When the SiO_2 layer had been etched, the Si wafer would sink to the bottom of the dish. Transferring the membranes into DI water for the three washing steps was more straightforward now as tweezers could be used to handle the tape windows.

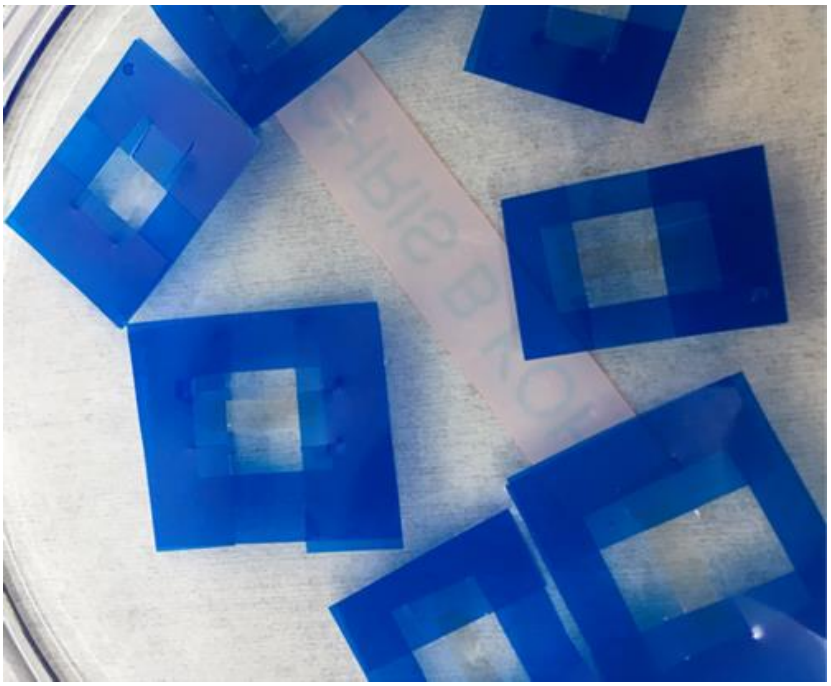

Figure 35: Tape windows with rGO/Paralene-C membranes.

After the third DI water bath, the windows were individually held in tweezers and dried using a very low flow of N_2 gas. This reduced the rippling on the membrane and water droplets (with contamination) beneath the membrane.

The transfer process was confirmed using a blank Si/SiO_2 substrate shown in Figure 36 before being used to transfer onto hole structures (shown in Figure 37). This was the transfer process eventually used for placing rGO/Parylene-C membranes onto waveguides.

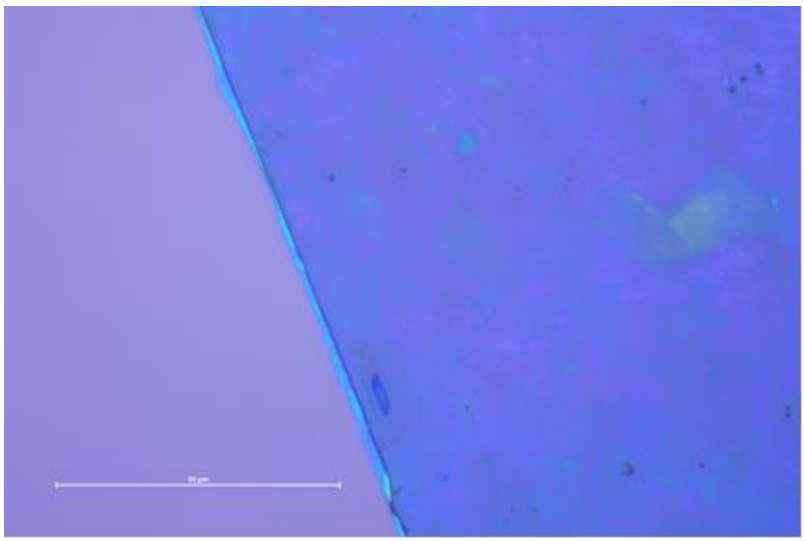

Figure 36: Example transfer showing rGO/Parylene-C membrane on Si/SiO_2 substrate.

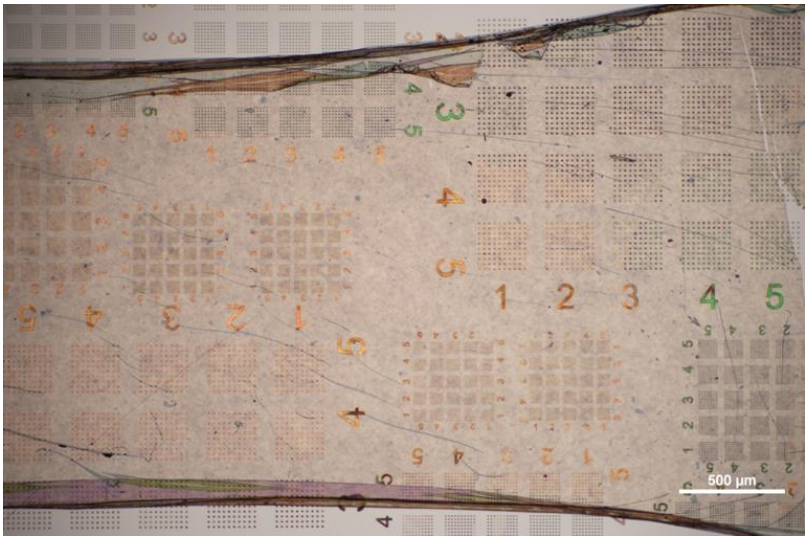

Figure 37: Initial transfer of rGO/Parylene-C membrane onto hole structures. The thicker edges at the top and bottom of the transfer are a result of scrolling of the transferred membrane. When unsupported, membranes will curl back onto themselves.

3.2.9 Blister inflation

Once membranes had been transferred onto the hole structures, they were placed into a nitrogen pressure chamber. The samples were placed into the chamber shown in Figure 38, which was attached to a nitrogen gas line. Nitrogen gas was added to the chamber until a pressure of 1 bar was reached. The pressurised chamber was sealed using the on/off valve, and the system was detached from the nitrogen line

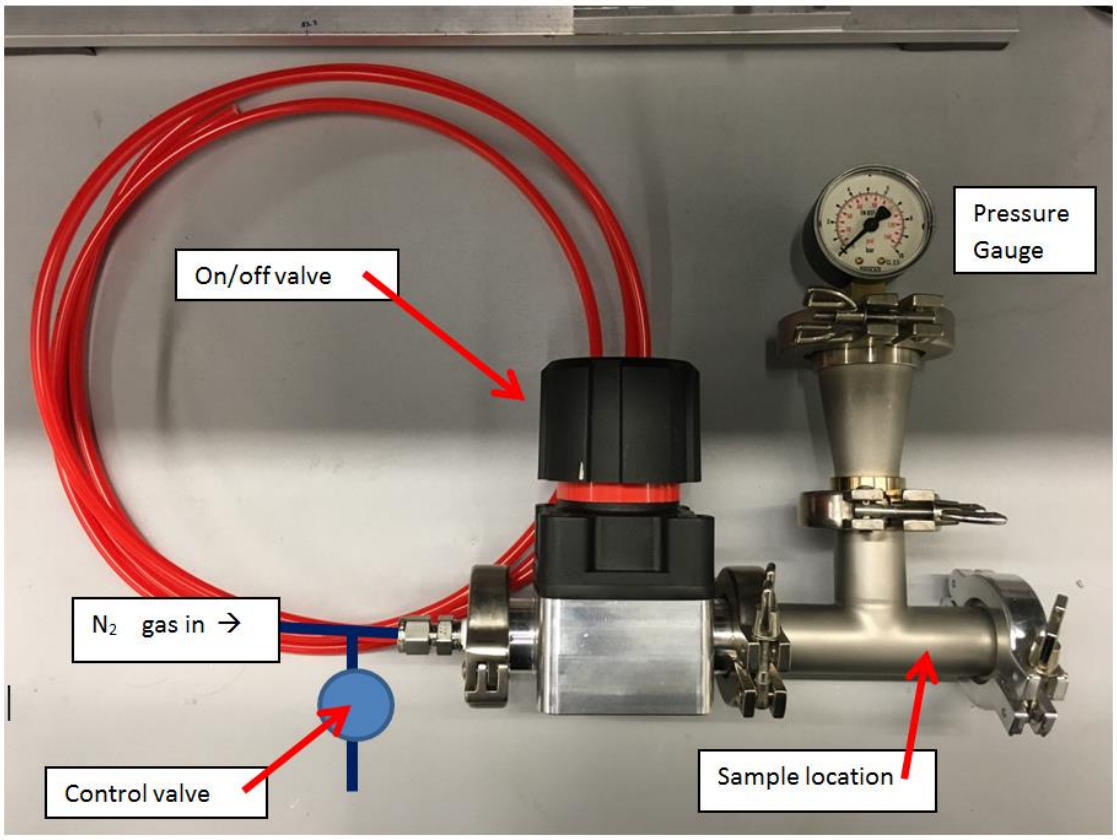

Figure 38: Nitrogen pressure chamber.

The samples were left in the pressurised chamber for 24 hours. This allowed the pressure to equalise from the chamber to the space underneath the membrane.

Once the sample was removed from the chamber, it was immediately measured using AFM with continuous scanning at regular intervals to measure deflation over time.

3.3 PMMA window structures on waveguides

To improve transfer efficiency, a PMMA layer was added to the waveguides, and electron beam lithography (EBL) was used to open triangular windows into it (schematically shown in Figure 39). This was done in order to have multiple waveguides covered with differing interaction lengths with only one membrane transfer.

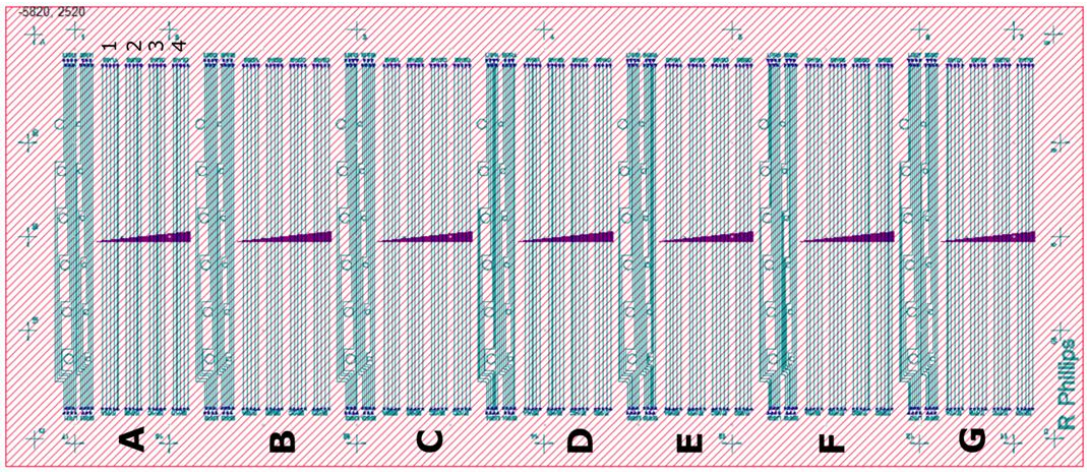

Figure 39: Schematic of the triangular PMMA windows on the waveguide chip.

The EBL was confirmed to have been successful with AFM, shown in Figure 40.

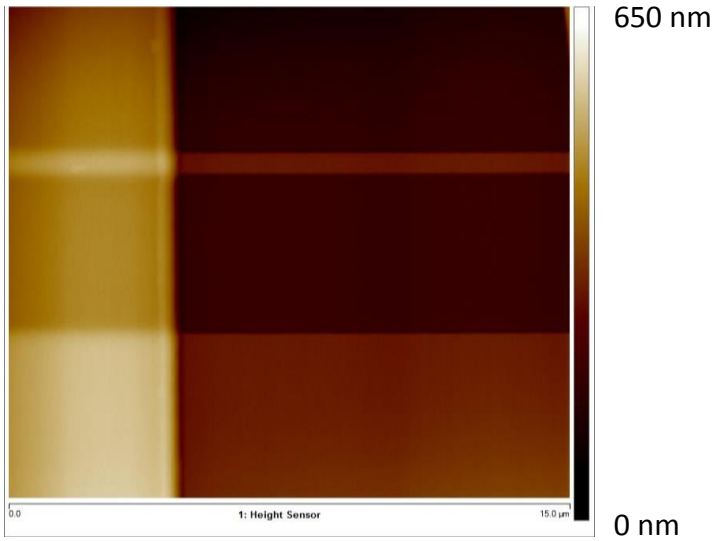

Figure 40: AFM height map of waveguide at the edge of a window in 120 nm deep PMMA.

4 Results and Discussion

4.2 Membranes on waveguides

4.2.3 GO on waveguides

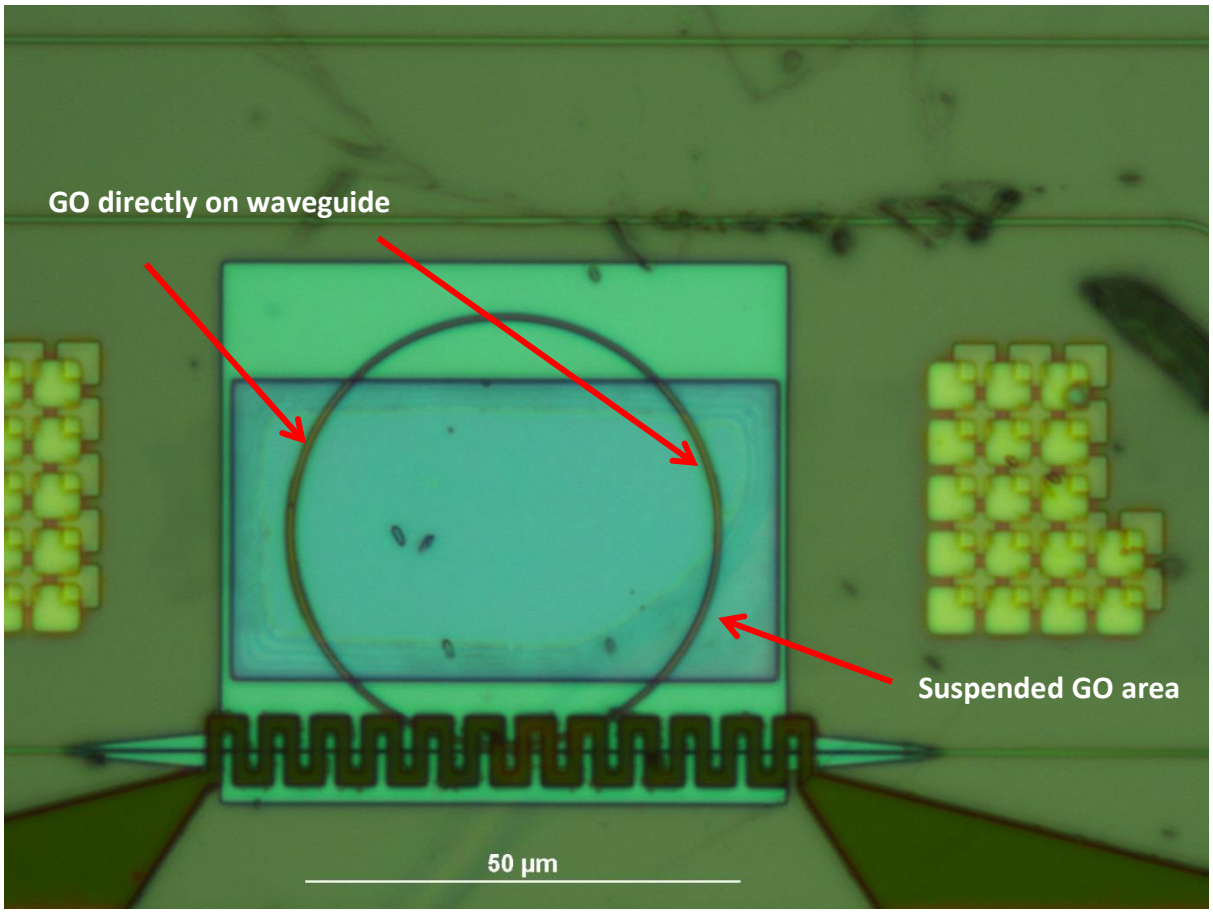

Figure 41: Optical Micrograph at 50x magnification of GO transfer onto a 25 µm radius ring resonator. The blue rectangle is the opening into the SiO_2 allowing access directly to the surface of the Si ring resonator.

The GO transfers onto windows etched in the top SiO_2 cladding material are shown in Figures 41 and 42, with 25 and 50 µm radius ring resonators, respectively. The transfer onto the smaller ring resonator was relatively successful as the GO membrane was almost entirely in contact with the ring resonator (and so inside the evanescent field of light). The transfer onto the larger ring resonator was not as successful. The GO on the right-hand side

of the transfer was successful, but the centre of the transfer experienced significant tearing, ripping and contamination. This can be attributed to the difficulties involved in the transfer process, particularly using a sharp tool to transfer the membrane from the tape structure to the chip. This difficulty in transfer led to the previously mentioned extensive iterations of the transfer process.

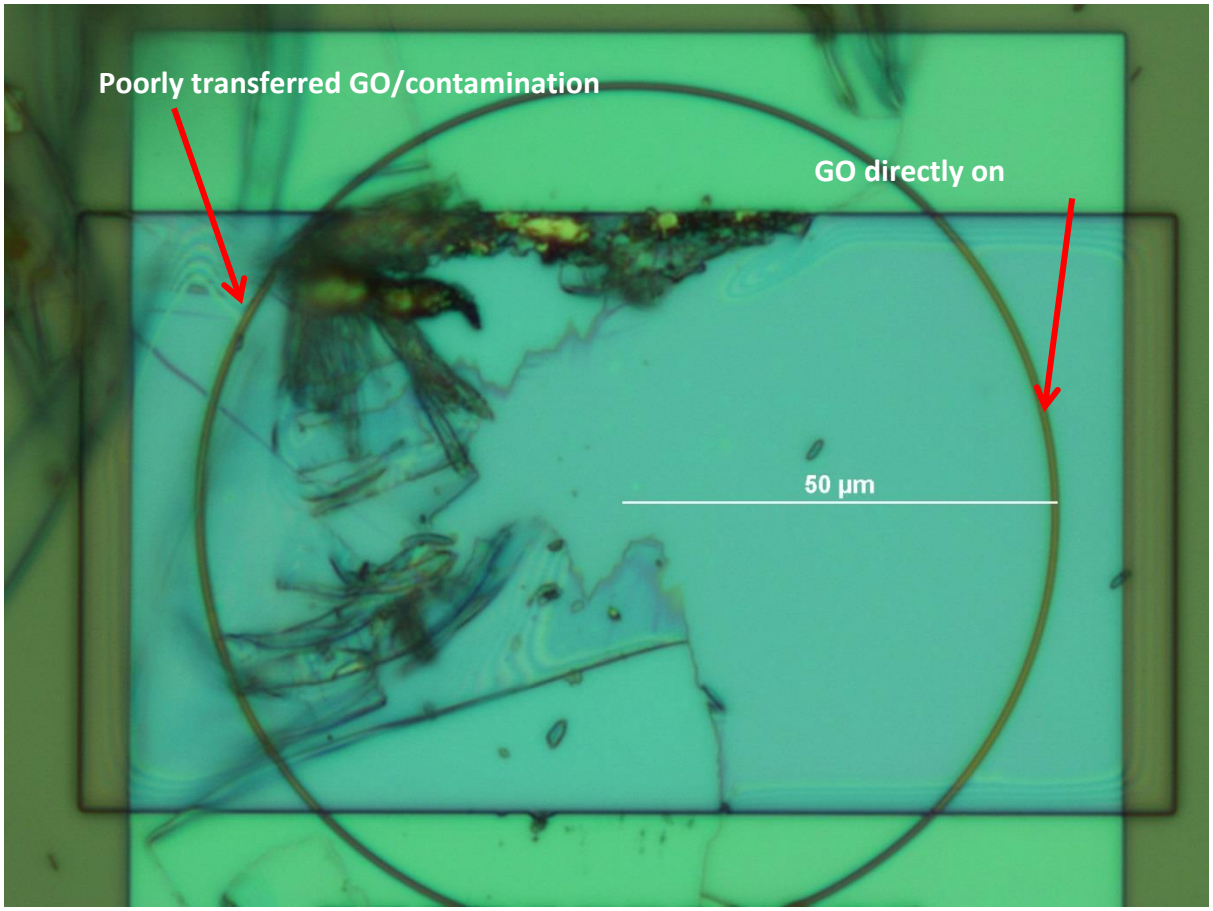

Figure 42: Optical Micrograph at 50x magnification of GO transfer onto a 50 µm radius ring resonator.

Although the transfer onto the larger ring resonator was not perfect, there is a significant amount of GO in contact with the ring resonator, which can still attenuate the light in the evanescent field.

Figures 43 and 44 show the optical spectra obtained from measurements of the waveguides with ring resonators before GO was transferred on the ring resonators and after.

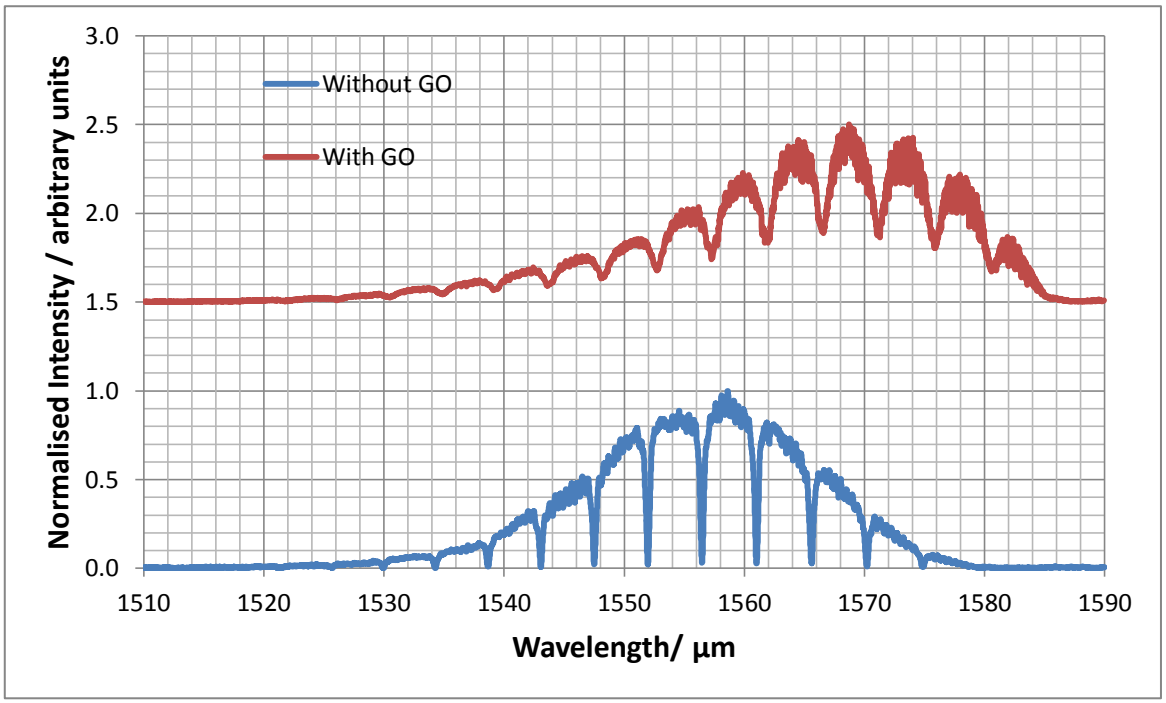

Figure 43: Graph showing intensity vs wavelength of a 25 µm radius ring resonator with and without suspended GO.

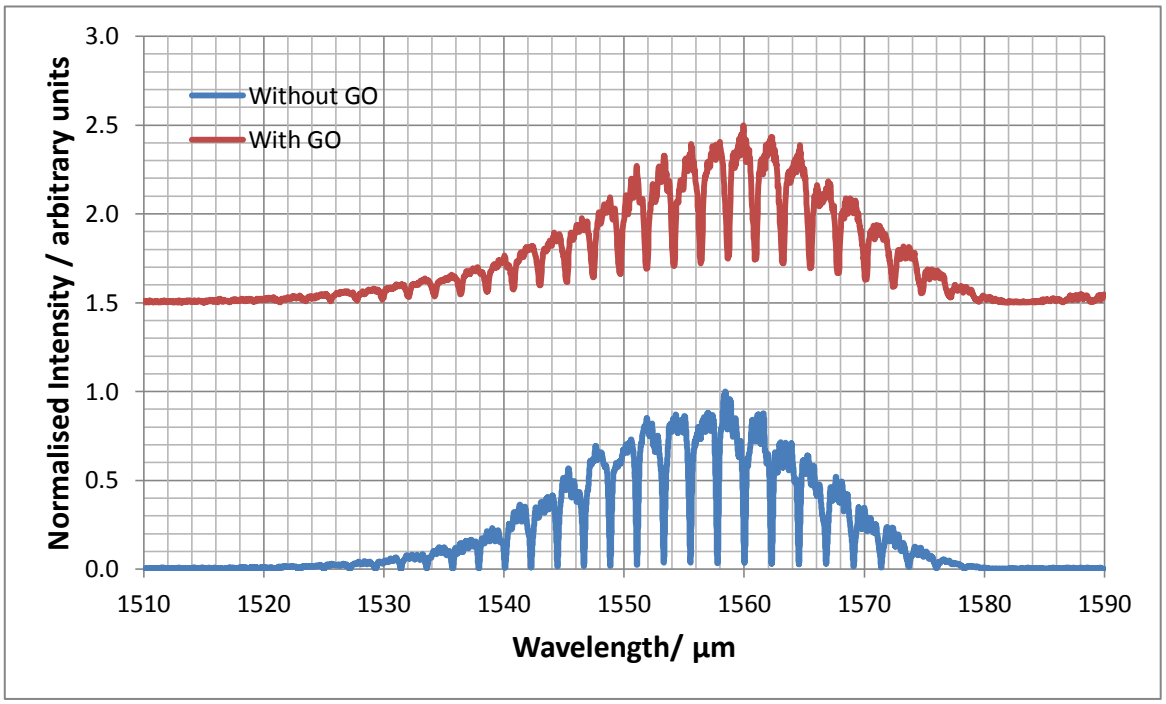

Figure 44: Graph showing intensity vs wavelength of a 50 µm radius ring resonator with and without suspended GO.

The smaller radius ring resonator has fewer notches which is in agreement with the literature as mentioned in the introduction. The notches have shifted further in the case of the 25 µm radius ring resonator than the 50 µm radius ring resonator. However, it could be the case that for the smaller ring, there is more loss at the short-wavelength end (after introducing GO), giving a distortion in the shape of the whole spectrum rather than a larger peak shift. This may be the case for only the smaller ring, possibly due to an increased impact of bend losses at short wavelengths. Further quantitative analysis needs to be undertaken with the data to determine the properties of the ring and the full effects of the GO transfer.

These spectra were flattened by converting the intensities into decibels. Two peaks were selected (from the middle of the spectra) and tracked for both resonators with and without GO, shown in Figures 45 and 46. This peak shift can be attributed to the change in refractive index of the area around the ring resonators due to the presence of the GO.[128] Resonant wavelengths shift proportionately higher as more matter is in contact with the ring – hence a greater shift is seen in the 50 µm radius ring resonator. A Lorentzian fitting was used to model the peaks to determine the extinction on resonance and Q factor of the ring resonators, both with and without GO (results shown in Table 2).

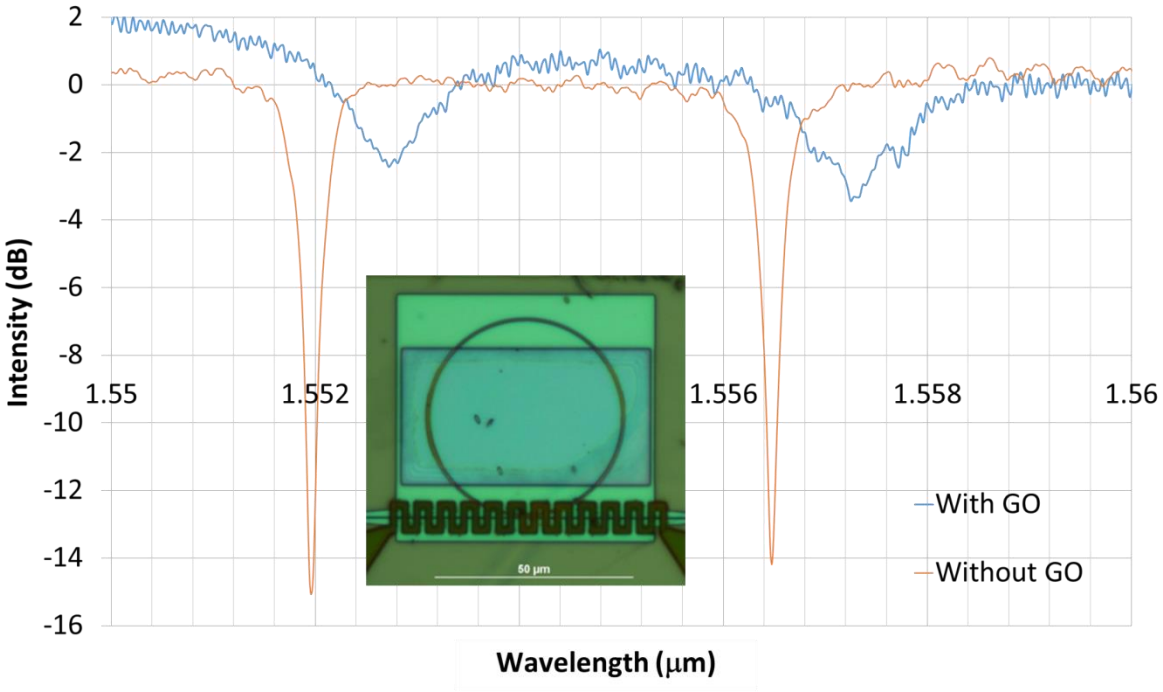

Figure 45: Isolated, normalised peaks of optical measurements of the 25 μm ring resonator with and without GO.

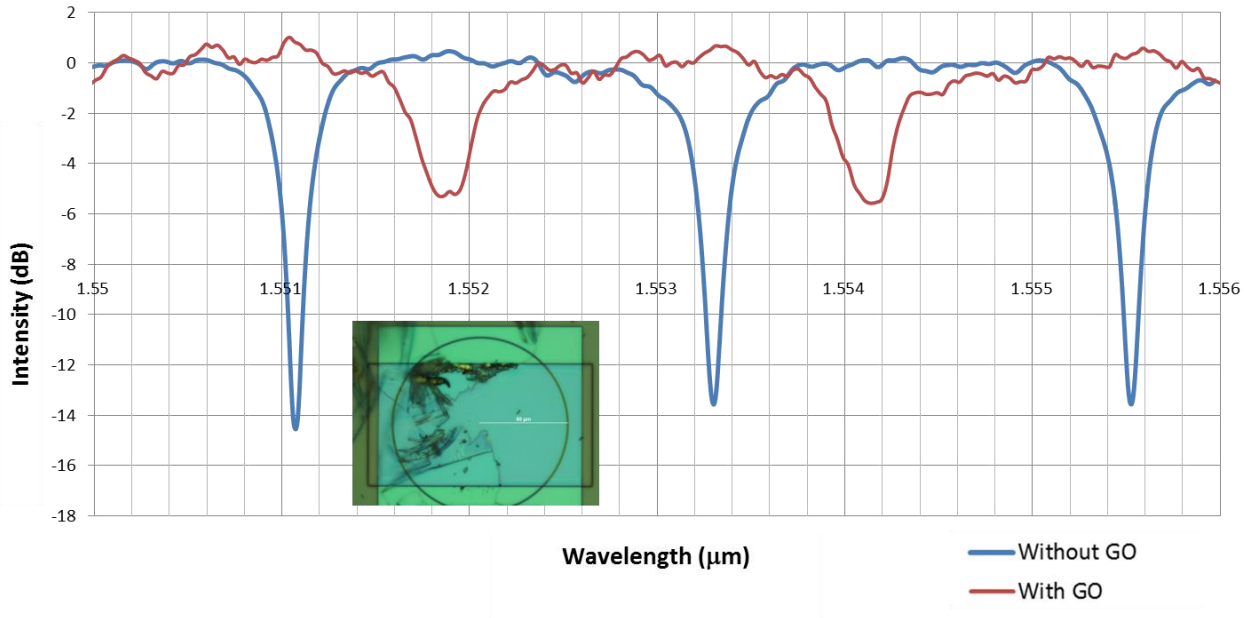

Figure 46: Isolated, normalised peaks of optical measurements of the 50 μm ring resonator with and without GO.

Table 2: Extinction on resonance, Q factor and peak shift of GO of 2 waveguides, 25 and 50 µm diameters.

		EoR/ dB	Q Factor	Peak shift/ nm
25 µm WG	Without GO	14.5	10500	
	With GO	3.1	1730	0.74
50 µm WG	Without GO	14.2	13500	
	With GO	5.1	5000	0.84

Although there is high attenuation with the addition of GO to the ring resonators, there are still clear "notches" in the spectra. Greater attenuation is seen in the 25 µm radius ring resonator, which can be attributed to a more complete covering of GO on the waveguide in comparison to the 50 µm radius ring resonator.

4.1.2 rGO on waveguides

The previously described transfer process was used to place rGO/Parylene-C membranes onto bus waveguides with triangular windows in a PMMA layer offering multiple interaction lengths, shown in Figure 47.

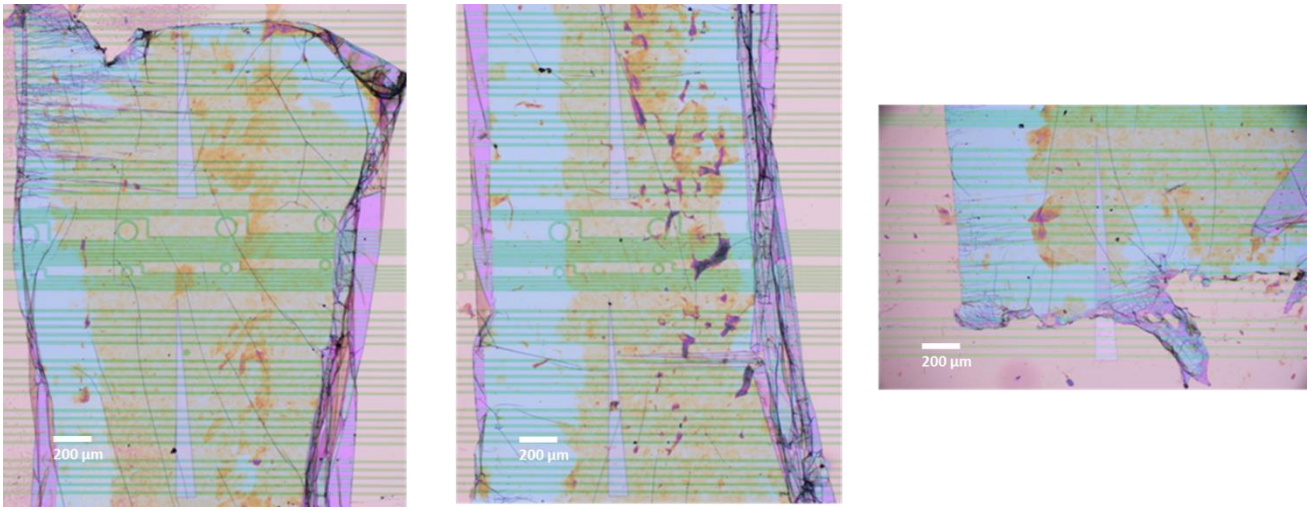

Figure 47: Optical micrographs of the rGO/Parylene-C transfer used for waveguide testing.

The bus waveguides were measured using the optical measurement setup before and after the addition of the membranes. The maximum intensity from each waveguide was used to create the graph shown in Figure 48.

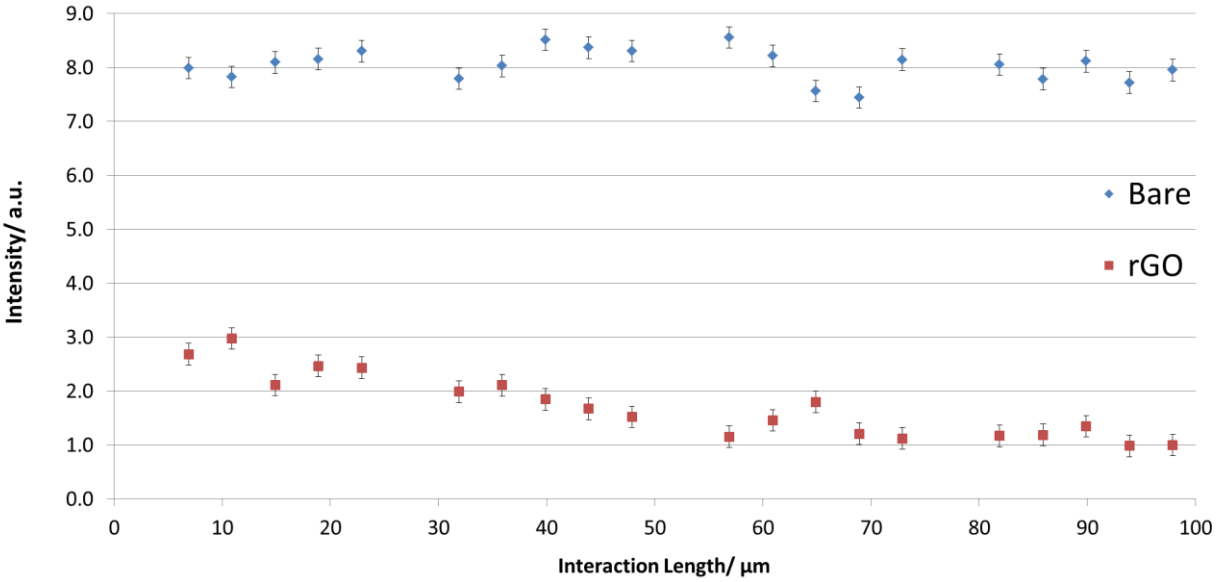

Figure 48: Graph showing intensity of transmitted light through bus waveguides vs interaction length of a rGO/Parylene-C membrane transferred directly onto the waveguide surface.

As expected, there is a clear reduction in intensity with increased interaction lengths of rGO on the waveguides.

4.3 AFM of membranes

4.3.3 GO membrane AFM thickness measurements

Figure 49 shows a representative height map of the GO membrane next to the scratch that was made. The image shows the contrast in the thicknesses of the membrane. Ripples and folds can be seen in the GO membrane as well as areas of overlap of flakes. The dotted line intersecting the AFM image in Figure 49 is shown in Figure 50 as a height profile line. There is a clear step in height from the area of the GO membrane to the area of the scratch (blank SiO_2 substrate).

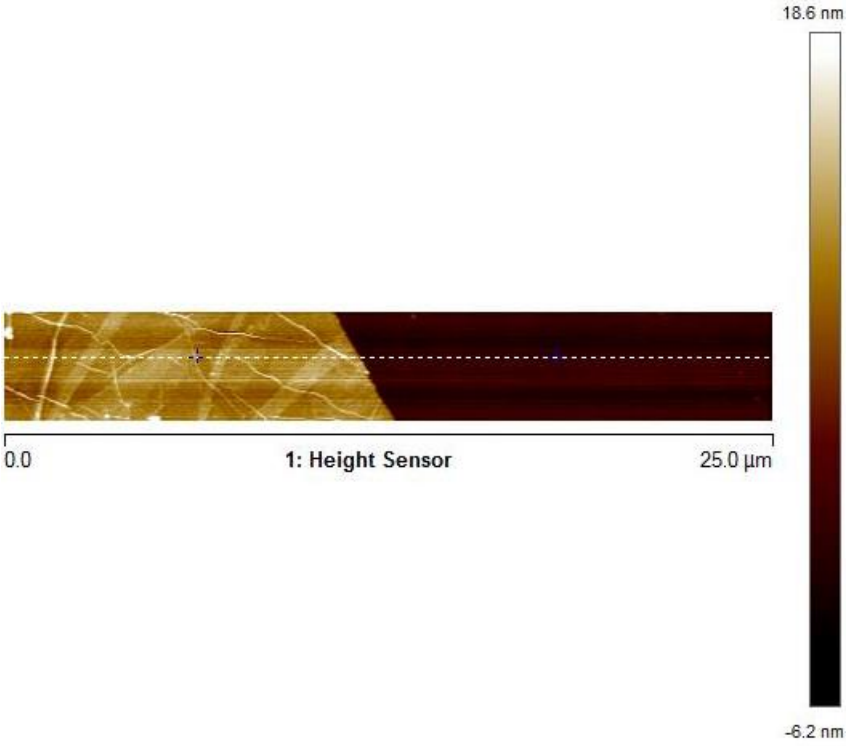

Figure 49: Height map of GO membrane alongside bare substrate.

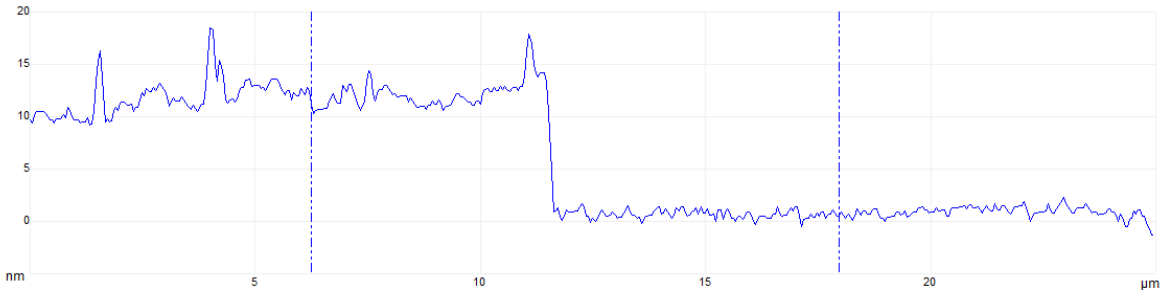

Figure 50: Height of GO membrane along the horizontal dotted line shown in Figure 49.

Height measurements were taken for each concentration of GO spun onto substrates which were then averaged and used to produce the graph shown in Figure 51.

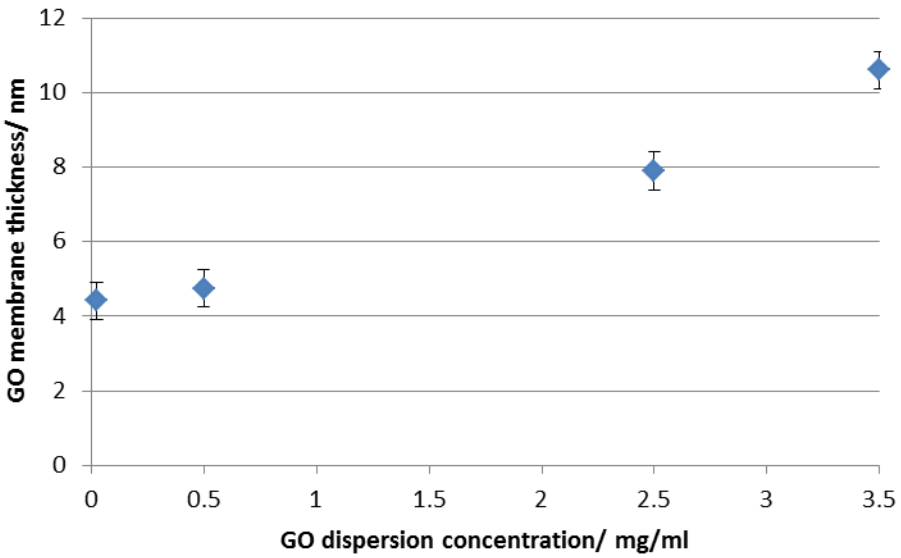

Figure 51: A graph showing the change in GO membrane thickness with a change in initial GO dispersion concentration in water.

With a thickness of between 4 nm and 11 nm, the membrane thickness can be controlled quite readily with initial GO concentration. 5 samples were taken per GO dispersion concentration. Error as estimated at ±0.5 nm per reading. GO membranes of ~4 nm are

seen to have 3-4 layers of GO. This becomes clear when analysing with AFM. A scan of an area with stacks of 1, 2, 3 and 4 flakes can be observed to have clear differences in thickness (Shown in Figure 52). This is desirable as it produces reasonably homogeneous membranes and gives sufficient flake overlap to avoid gaps in the membrane that are seen if very low initial dispersion concentrations are used.

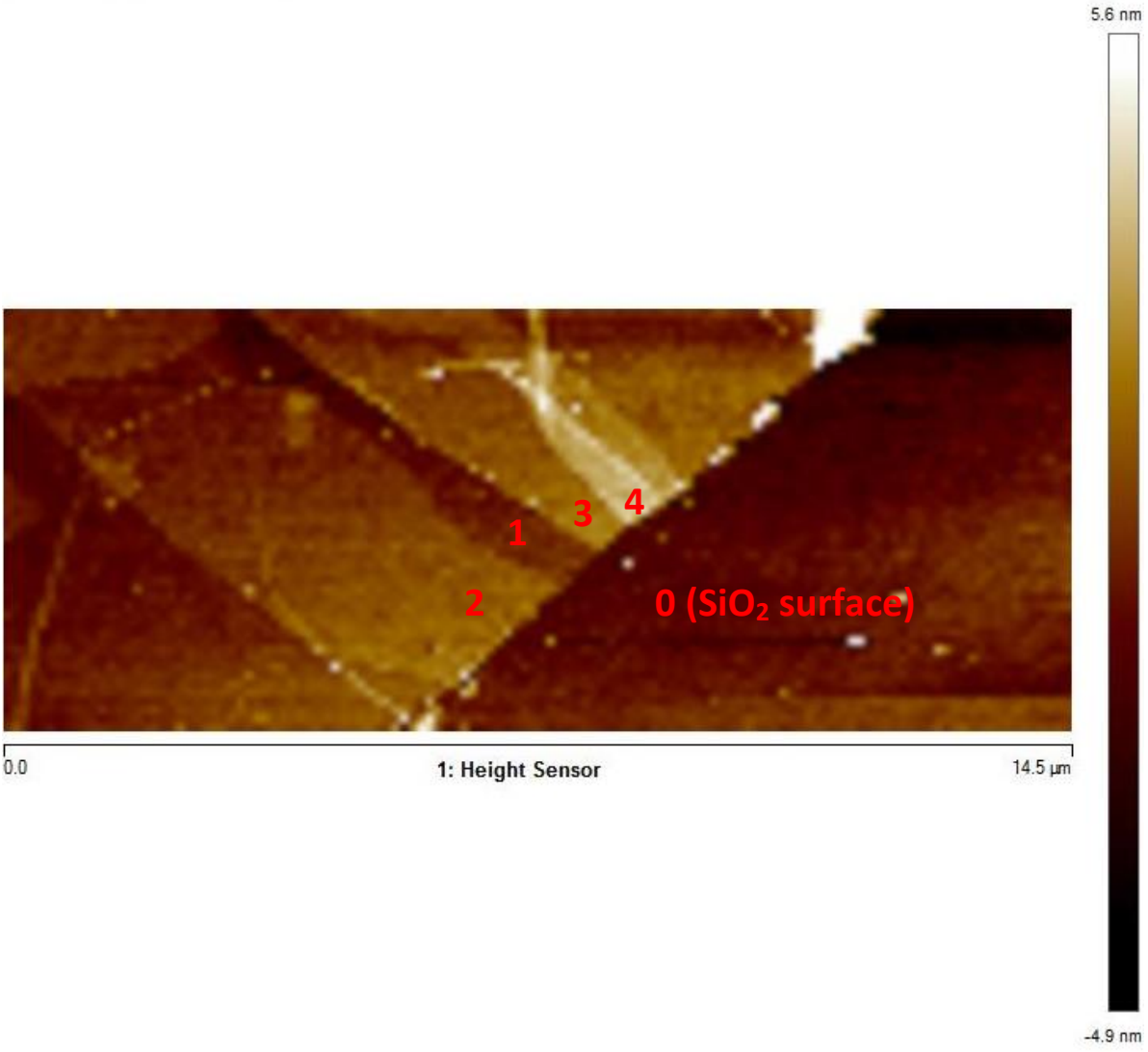

Figure 52 AFM height sensor map of a GO membrane on SiO_2 from a 0.01 mg/ml dispersion – inset numbers indicate number of layers of GO where flakes overlap.

4.2.2 GO suspended on microcavities

GO was transferred onto 3 µm diameter holes etched 200 nm deep into SiO_2 on a SiO_2/Si substrate. The AFM image in Figure 53 shows the GO suspended over one of the cavities.

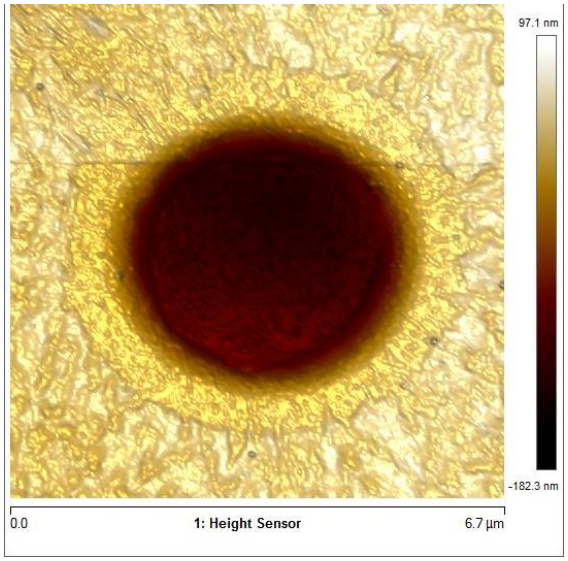

Figure 53: AFM image showing a GO membrane suspended over a 3 µm diameter cavity.

A height profile line through the centre of another cavity is shown in Figure 54. This membrane was over a hole with incomplete etching which can be seen from the bottoming out of the membrane at 163 nm. This explains the flat profile at the bottom of the height profile.

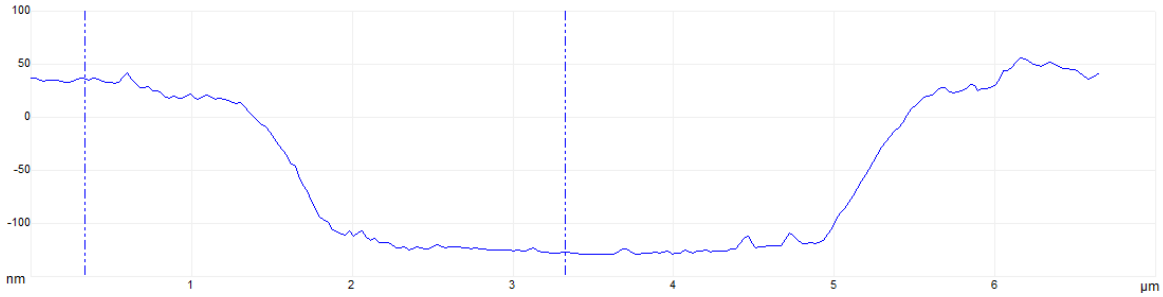

Figure 54: Height profile of the suspended GO membrane.

For this reason, cavity fabrication methods were altered to deepen the holes to allow for total suspension of membranes.

4.2.3 rGO/Parylene-C membranes suspended on microcavities

Following the transfer of the membranes onto hole structures, optical images were taken using a microscope. An example transfer is shown in Figure 55.

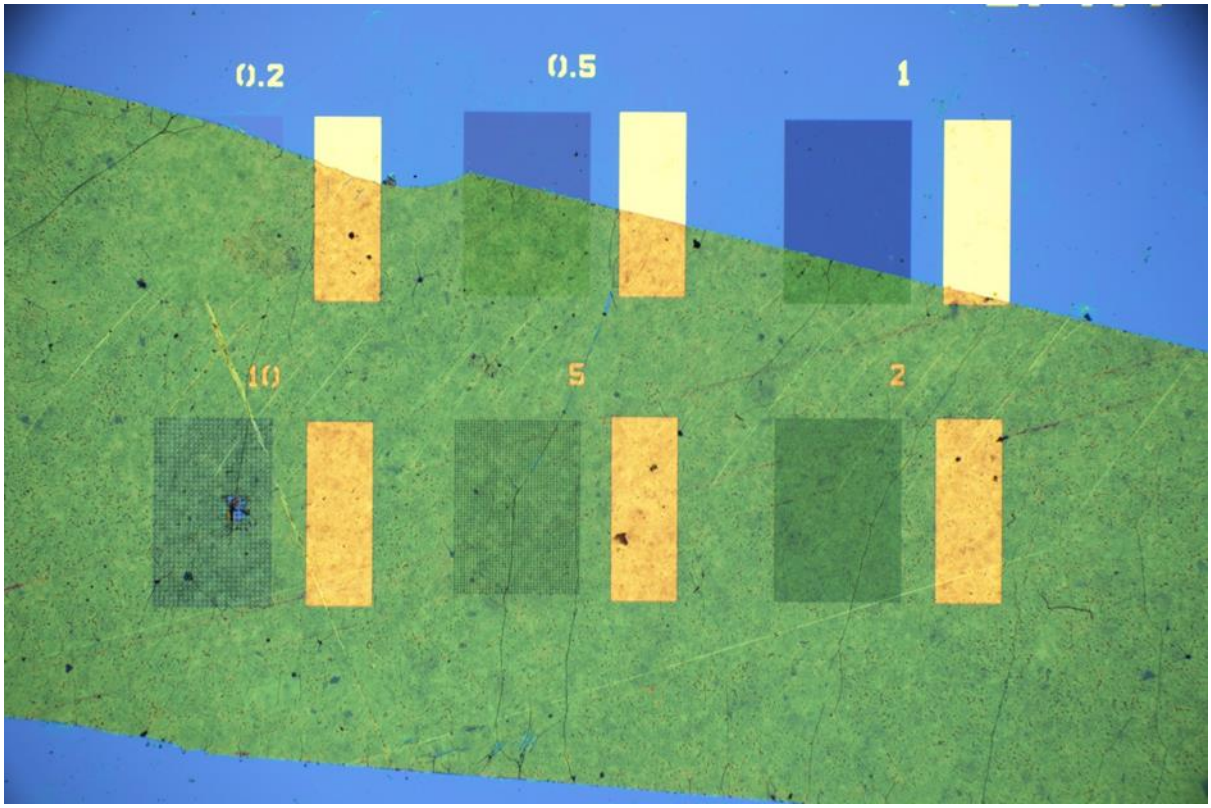

Figure 55: rGO/Parylene-C membrane transferred over hole structures of 0.2, 0.5, 1, 2, 5 and 10 µm diameters..

The result was successful suspension over holes of 0.5, 1 and 2 µm diameter. The corresponding membrane depths are shown in Table 3. Figure 56 shows the majority of the holes with successful suspension in yellow and failed suspension in blue.

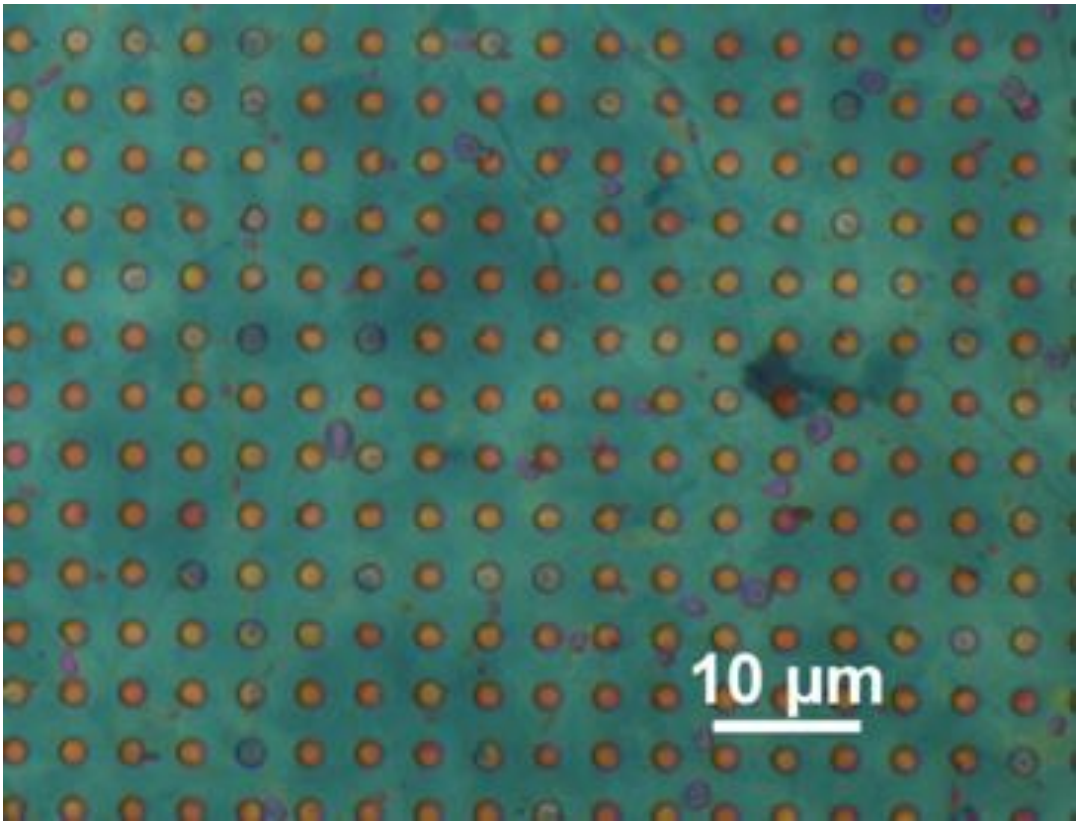

Figure 56: Optical microscope image of rGO/Parylene-C membrane on top of 2 µm holes.

Table 3: Hole diameters and membrane depths for initial suspension.

Hole diameter/ µm	0.2	0.5	1	2	5	10
Membrane depth/ nm	n/a	9-13	~20	~80	n/a	n/a

The 0.2 µm holes were too small to discern with a membrane on top. Due to the stiffness of the membrane, there was no perceivable sag into the 0.2 µm holes. Given that the membranes were already in that order of magnitude for thickness, this hole diameter was disregarded for future testing. The first trial of membranes were transferred before the deepening of the cavities, and as such, the 5 and 10 µm diameter holes were too wide and shallow to suspend a membrane over, resulting in bottoming out.

5 and 10 µm holes resulted in membranes sticking to the bottom of the cavities; a cross-section is shown in Figure 57. This led to the decision to use deep reactive ion etching (DRIE) methods for cavity deepening. Typical DRIE processes involve the use of a high-density plasma. A sequence of alternating steps no more than a few seconds long of silicon etching and polymer deposition are used. The polymer deposition is used to protect the already-carved features from further lateral etching.[129]

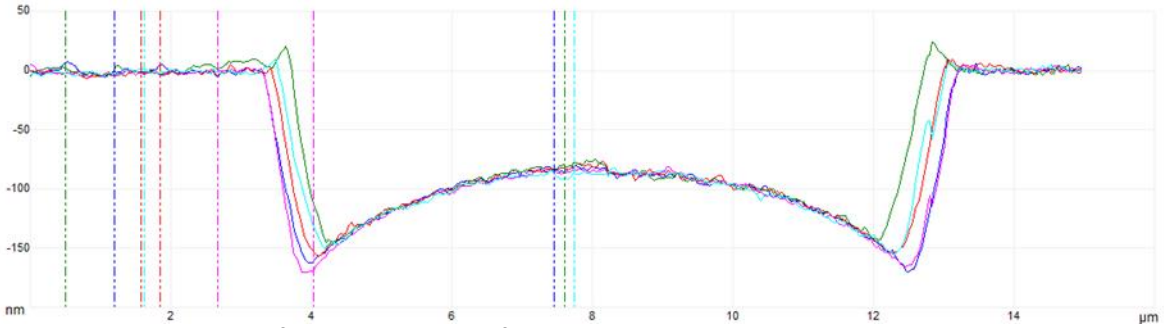

Figure 57: An example of the cross-section of a bottomed-out membrane. This example was completed with a "wet" transfer resulting in the blister shape at the bottom of the cavity.

Following cavity deepening with DRIE, membranes were suspended over 5 µm diameter holes. Figure 58 shows an example of this.

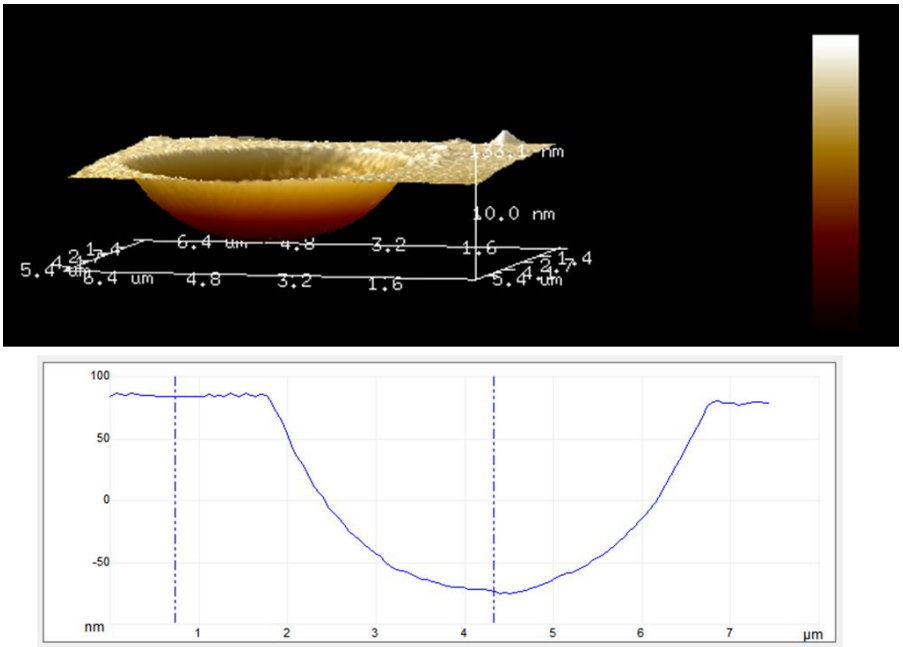

Figure 58: Example of an rGO/Parylene-C composite membrane (4.88 nm rGO, 38.8 nm Parylene-C) suspended over a 5 µm hole.

Further measurements were carried out on thicker membranes. Initial measurements showed membrane deflections of ~140 nm for rGO membranes with 38.8 nm of Parylene-C and ~75 nm for rGO membranes with 208.3 nm of Parylene-C

The first blister tests were carried out on thicker membranes. An example 3D rendering of an AFM height map is shown in Figure 59.

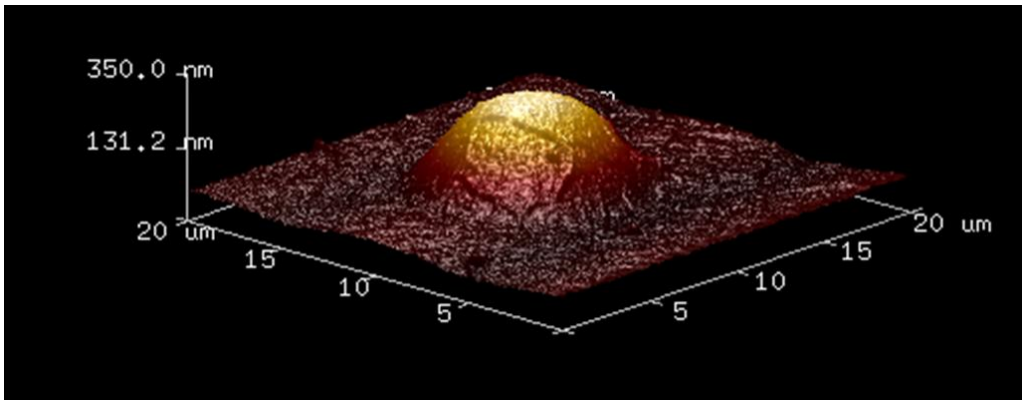

Figure 59: Example AFM 3D rendering of an inflated blister.

Three blisters from the sample were chosen to be scanned. The deflation of these blisters is shown as a reduction of blister height over time shown in Figure 60.

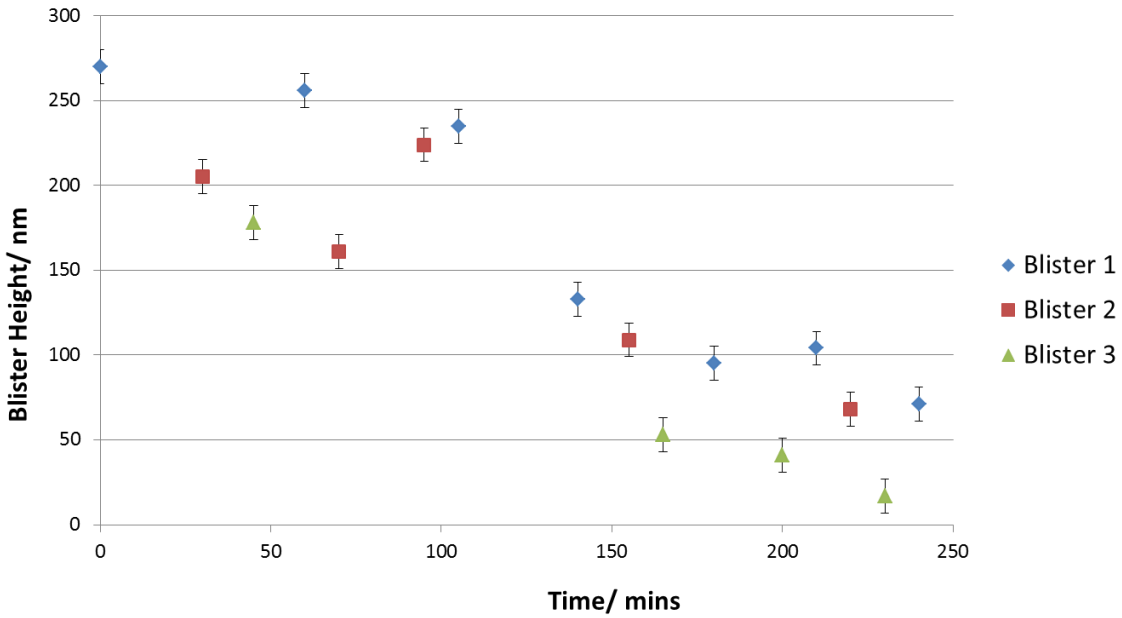

Figure 60: Deflation over time of 10 µm diameter blisters formed with a 208.3 nm rGO/Parylene-C membrane measured as blister heights. Error of blister height estimated at ±10 nm to account for scan time.

4.2.4 Raman spectrum of GO

Raman spectroscopy was undertaken to check that the GO was as expected and representative of GO recognised in the literature. The observed spectrum is shown in Figure 61.

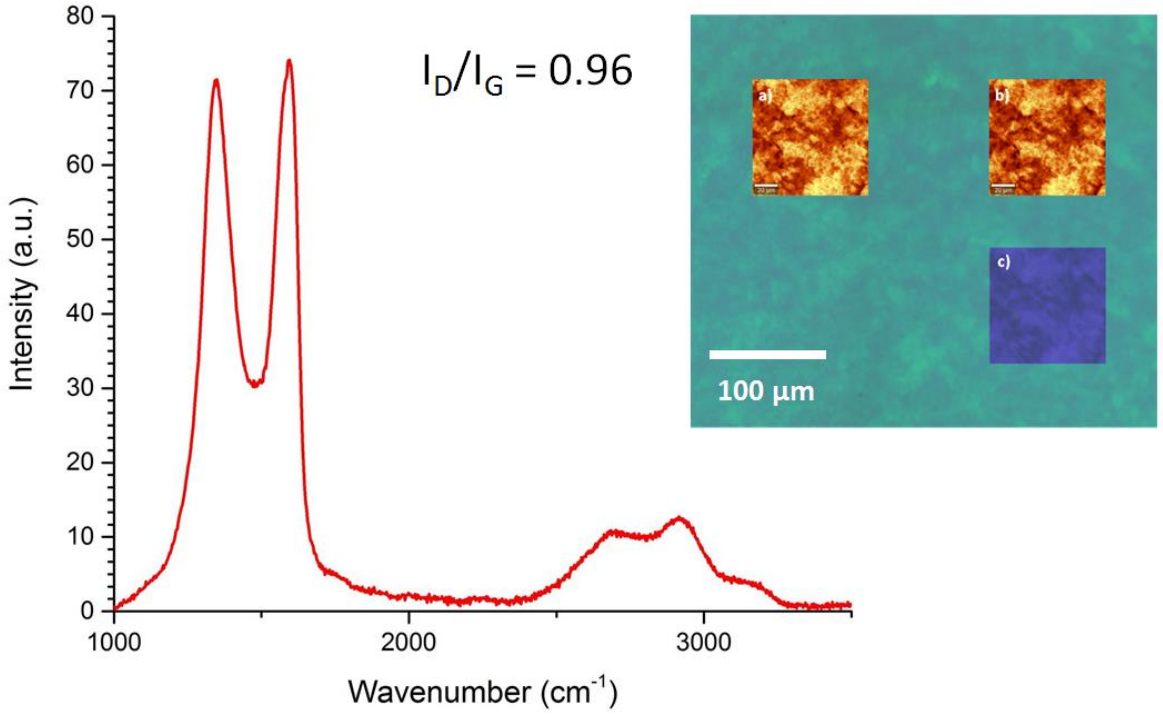

Figure 61: Raman spectrum of GO membrane on Si/SiO_2 substrate a) D peak intensity map of the analysed area. b) G peak intensity map of the analysed area. Inset: An optical image of GO showing where a 100 µm x 100 µm Raman map was measured, c).

The Raman spectrum in Figure 61 shows the characteristic D and G peaks. Raman spectroscopy works by measuring the scattering of incident light as a result of different lattice phonons. Graphene oxide has important characteristic G and D peaks, whereas pristine graphene only exhibits a G peak.

The D peak gives a measure of disorder, hence why it is not present in pure graphene. The disorder is related to the breathing mode of aromatic rings. The D peak is pronounced in GO due to k-point phonons of A_{1g} symmetry.[130] Two parameters control the intensity of the D peak: a short-range structural disorder parameter and a long-range activation parameter of the regions beyond the local disorder. With a greater amount of defects in a lattice, the short-range disorder effect will increase as areas overlap, eventually reaching a saturation point at which the D peak intensity reaches a maximum.[131]

The G peak is attributable to interaction with the E_{2g} in-plane vibration mode and bond stretching of sp^2 carbon pairs.[132] The Raman spectrum observed was similar to the literature results.[133]

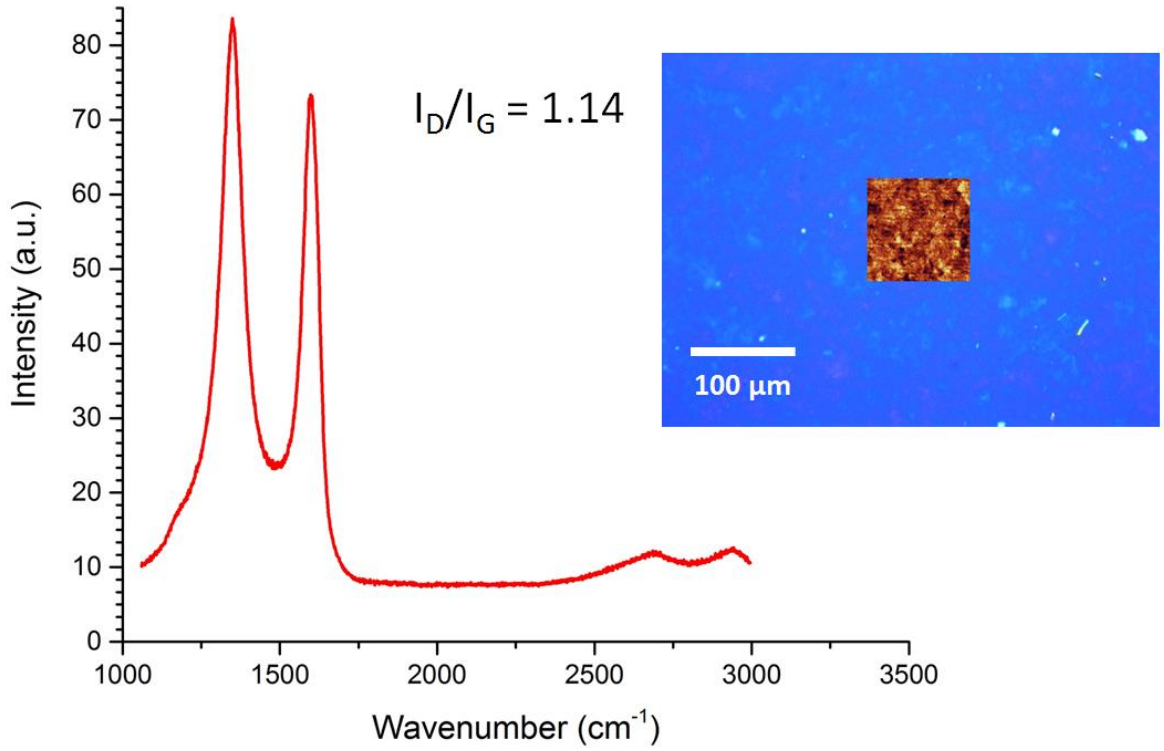

Figure 62: Raman spectrum of rGO membrane on Si/SiO_2 substrate.

The reduction process of GO can manifest itself in Raman spectra by the changes in relative intensity of two main peaks: D and G, which can be observed in Figure 62. This information is used to verify the reduction process. The increase of the D peak intensity indicates the forming of more sp^2 domains. The relative intensity ratio of both peaks (I_D/I_G) is a measure of disorder degree and is inversely proportional to the average size of the sp^2 clusters. This suggests that new (or more) graphitic domains are formed, and the sp^2 cluster number is increased.

4.2.5 UV-Vis spectroscopy

A stock solution of GO was supplied by another member of the research group. UV-Vis spectroscopy is part of the quality control process. An example UV-Vis spectrum of the GO is shown in Figure 63.

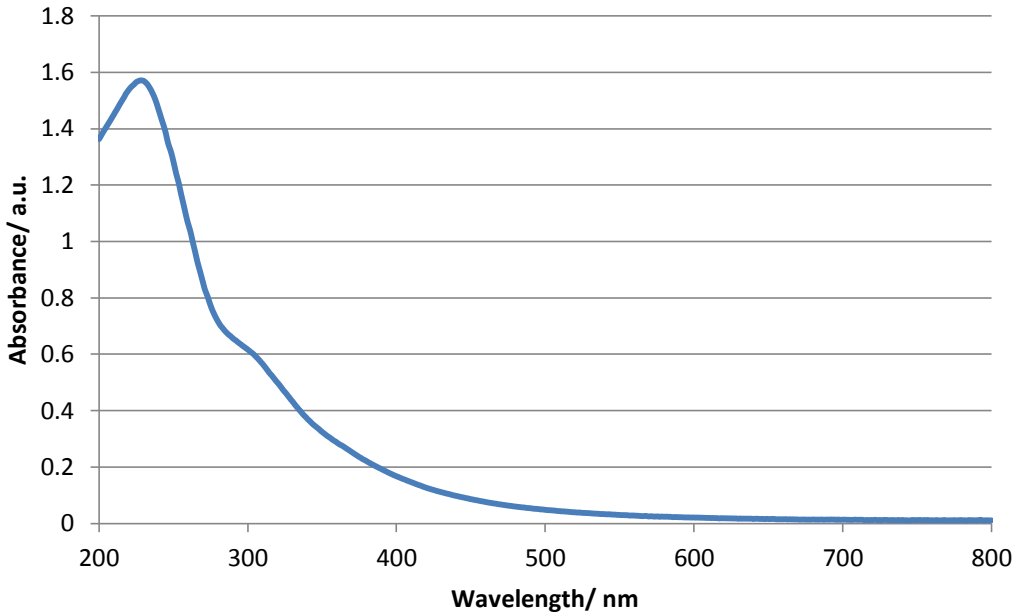

Figure 63: UV-Vis spectrum for 0.03125 mg/ml GO.

The GO is supplied in a thick, highly viscous gel, which is difficult to transfer. A drying method is used to find the initial concentration of the gel. This is then used to dilute to known concentrations. The gel is therefore diluted, and concentrations are found for each dilution.

The absorbance at 660 nm was found for each dilution to form a calibration curve, shown in Figure 64. From the Beer-Lambert law, $A = \varepsilon l c$, where A is absorbance, ε is absorption

coefficient, l is length, and c is concentration, the gradient of the line produced in the absorbance/concentration graph is the absorption coefficient (as l is constant).

660 nm is chosen as it is away from electronic interactions that occur at less than 400 nm, closer to UV. 660 nm measurements come from scattering where light is impeded.

The drying method for finding the concentration can take up to 3 days. Now that the absorption coefficient for this GO is known, the concentration of any dilution can be found in a matter of minutes.

The results are very good in this case as the equation for the line (Figure 64 inset) shows only a very small intercept value (due to marginal experimental error) and an R^2 value of 0.9999.

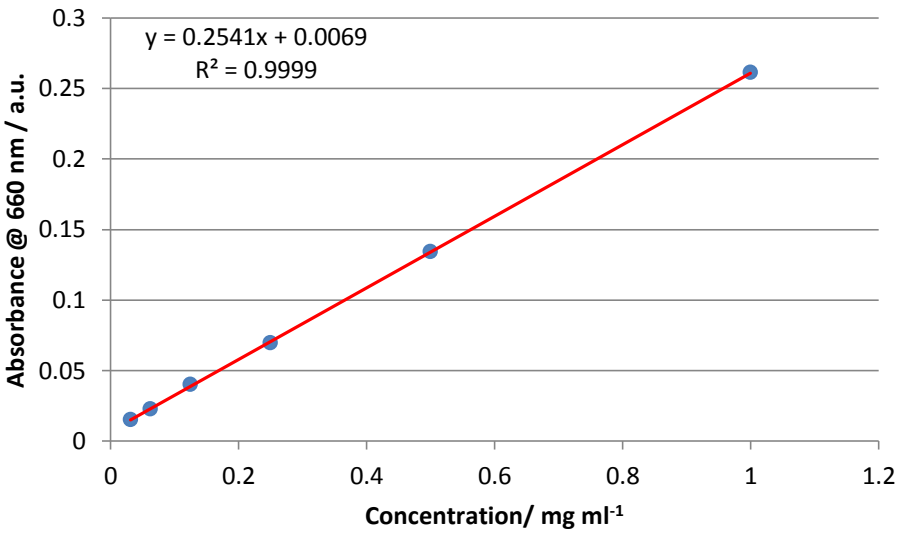

Figure 64: Calibration curve for the UV-Vis spectrum of the used GO (inset: equation for the line and R^2 value).

5 Conclusions and Further Work

A CVD graphene transfer process has been adapted for GO and shown to be effective. This is beneficial as it has also been shown that different thicknesses of GO membrane are achievable and reproducible by using different concentrations of GO in solution. However, because GO is dispersible in acetone, the transfer process has had to be modified with a different etching process that adds an extra step.

The thicknesses of membranes have been measured using AFM, and now a process exists for spinning specific thickness membranes from a dispersion of GO in water.

GO has been shown suspended over cavities. However, there are difficulties in processing GO. Regular methods for transferring CVD-graphene require a plasma etching step to remove the graphene that isn't required. This cannot be used in the process for GO as the plasma etch time required is much longer for GO than it is for graphene. Longer etching times cause the photoresist on the sample (from lithography) to crosslink, which makes it insoluble, rendering the rest of the transfer process impossible.

GO tends to sag more than graphene when it is suspended. This is because the GO membrane is multilayer and multi-flake. This means that the membrane has ripples and folds that will unfold when the GO is suspended, hence why the GO membrane suspends so far into the cavity it is placed on. However, the same van der Waals forces apply to GO as to graphene. Therefore, it should be possible to perform blister pressure testing and elastic modulus testing, techniques that have been shown for graphene covering micro-cavities.

These reasons dictated the move to rGO membranes. It was found that they were easier to transfer and interface with silicon photonic waveguides. Parylene-C was shown to be an

excellent composite material for the membranes to increase structure and improve transferability. Their structural resilience has been proven through blister testing.

Optical data has been gained from the waveguides with rGO/Parylene-C composite membranes. A fit needs to be made to the data using the following expression, modified from work by Menon et al.[134]

$$T\left(\lambda, L, n_{eff}, \alpha\right) = \left(1-\gamma\right)\left[\frac{\left(\sqrt{1-k}\right)-\left(\sqrt{1-\gamma}\right)e^{-\alpha\frac{\left(Ln_{eff}\right)}{2}-i\left(2\pi n_{eff}^{2}\frac{L}{\lambda}\right)}}{1-\left(\sqrt{1-\gamma}\right)\left(\sqrt{1-k}\right)e^{-\alpha\frac{\left(Ln_{eff}\right)}{2}-i\left(2\pi n_{eff}^{2}\frac{L}{\lambda}\right)}}\right]^{2}$$

Where k and γ are power coupling and intensity loss factors respectively, which are dependent on the coupling efficiency of the ring resonator structure, L (= $2\pi r + 2L_c$) is the total physical round-trip length of the ring resonator waveguide with a radius of curvature, r and coupling length, L_c. n_{eff} is the effective refractive index, and α is the loss coefficient, which includes contributions from both scattering and absorption.[1] A fit will need to be made from this expression and the spectra obtained so far with the rGO/Parylene-C composite membranes.

It has been shown that due to the interaction strength of the evanescent field, there is a dependence on the height of the graphene from the waveguide to the absorption coefficient.[135] This is shown in the following equation:

$$\alpha\left(h\right) = \alpha_0 e^{-2\gamma h}$$

Crowe et al.[1] analysed results from Menon et al.[134] to derive α_0 as the linear absorption coefficient for h = 0 of graphene above the waveguide and derived the waveguide evanescent decay constant, γ. Furthermore, the length of graphene L_g was incorporated to lead to an expression for signal attenuation, A_g, as a function of both L_g and h.

$$A_g\left(L_g, h\right)_{dB} = \left[ER(0) - ER(L_g)\right]_{dB} = \alpha_0 e^{-2\gamma h} L_g$$

Further AFM blister testing can be carried out on rGO/Parylene-C membranes in order to extract their exact mechanical properties.

Additional work needs to be undertaken in suspending rGO/Parylene-C membranes over waveguides. Once suspended, optical measurements should be taken whilst the pressure on the suspended membranes is fluctuated. This will form the basis of a suspended membrane silicon photonic pressure sensor.

6 References

1. Crowe, I. F. *et al.* Determination of the quasi-TE mode (in-plane) graphene linear absorption coefficient via integration with silicon-on-insulator racetrack cavity resonators. **22**, 18625–18632 (2014).

2. Geim, A. K. & Novoselov, K. S. The rise of graphene. *Nat. Mater.* **6**, 183–191 (2007).

3. Peierls, R. Quelques propriétés typiques des corps solides. *Ann. l'I.H.P.* **5**, 177–222 (1935).

4. Landau, L. Zur Theorie der Phasenumwandlungen II. *Phys. Z. Sowjet* **11**, 26–35 (1937).

5. Novoselov, K. S. K. S. *et al.* Electric field effect in atomically thin carbon films. *Science (80-.).* **306**, 666–669 (2004).

6. Singh, V. *et al.* Graphene based materials: Past, present and future. *Prog. Mater. Sci.* **56**, 1178–1271 (2011).

7. Sadasivuni, K. K., Ponnamma, D., Thomas, S. & Grohens, Y. Evolution from graphite to graphene elastomer composites. *Prog. Polym. Sci.* **39**, 749–780 (2014).

8. Hu, K., Kulkarni, D. D., Choi, I. & Tsukruk, V. V. Graphene-polymer nanocomposites for structural and functional applications. *Prog. Polym. Sci.* 1–39 (2014). doi:10.1016/j.progpolymsci.2014.03.001

9. Lee, C., Wei, X., Kysar, J. W. & Hone, J. Measurement of the elastic properties and intrinsic strength of monolayer graphene. *Science* **321**, 385–388 (2008).

10. Zhu, Y. *et al.* Graphene and graphene oxide: Synthesis, properties, and applications. *Adv. Mater.* **22**, 3906–3924 (2010).

11. Yang, Y., Asiri, A. M., Tang, Z., Du, D. & Lin, Y. Graphene based materials for biomedical applications. *Mater. Today* **16**, 365–373 (2013).

12. Wang, Y., Li, Z., Wang, J., Li, J. & Lin, Y. Graphene and graphene oxide: Biofunctionalization and applications in biotechnology. *Trends Biotechnol.* **29**, 205–212 (2011).

13. Balandin, A. a *et al.* Superior Thermal Conductivity of Single-Layer Graphene 2008. *Nano Lett.* **8**, 902–907 (2008).

14. Savage, N. Materials science: Super carbon. *Nature* **483**, S30–S31 (2012).

15. Martin, P. Electrochemistry of gaphene: New horizons for sensing and energy storage. *Chem. Rec.* **9**, 211–223 (2009).

16. Liu, Y., Dong, X. & Chen, P. Biological and chemical sensors based on graphene materials. *Chem. Soc. Rev.* **41**, 2283 (2012).

17. Geim, A. K. Graphene: Status and Prospects. *Science (80-.).* **324**, 1530–1534 (2009).

18. Ojha, K., Anjaneyulu, O. & Ganguli, A. K. Graphene-based hybrid materials: synthetic approaches and properties. *Curr. Sci.* **107**, 397–418 (2014).

19. Stoller, M. D., Park, S., Zhu, Y., An, J. & Ruoff, R. S. Graphene-Based Ultracapacitors. *Nano Lett.* **8**, 3489–3502 (2008).

20. Wang, X., Zhi, L. & Müllen, K. Transparent, Conductive Graphene Electrodes for Dye-Sensitized Solar Cells. *Nano Lett.* **8**, 323–327 (2008).

21. Soldano, C., Mahmood, A. & Dujardin, E. Production, properties and potential of graphene. *Carbon N. Y.* **48**, 2127–2150 (2010).

22. Paredes, J. I., Marti, A., Tasco, J. M. D. & Martı, A. Graphene Oxide Dispersions in Organic Solvents. *Langmuir* **24**, 10560–10564 (2008).

23. Paton, K. R. *et al.* Scalable production of large quantities of defect-free few-layer graphene by shear exfoliation in liquids. *Nat. Mater.* **13**, 624–30 (2014).

24. Terrones, M. *et al.* Graphene and graphite nanoribbons: Morphology, properties, synthesis, defects and applications. *Nano Today* **5**, 351–372 (2010).

25. Chen, L., Hernandez, Y., Feng, X. & Müllen, K. From Nanographene and Graphene Nanoribbons to Graphene Sheets: Chemical Synthesis. *Angew. Chemie - Int. Ed.* **51**, 7640–7654 (2012).

26. Lalwani, G., Cai, X., Nie, L., Wang, L. V. & Sitharaman, B. Graphene-based contrast agents for photoacoustic and thermoacoustic tomography. *Photoacoustics* **1**, 62–67 (2013).

27. Rafiee, M. a *et al.* Graphene Nanoribbon Composites. *ACS Nano* **4**, 7415–7420 (2010).

28. Zhang, R. Q. & de Sarkar, A. Theoretical Studies on Formation , Property Tuning and Adsorption of Graphene Segments. *Phys. Appl. Graphene - Theory* **INTECH Ope**, 3–28 (2011).

29. Bonaccorso, F., Sun, Z., Hasan, T. & Ferrari, a. C. Graphene Photonics and Optoelectronics. **4**, 611–622 (2010).

30. Avouris, P. Graphene: Electronic and photonic properties and devices. *Nano Lett.* **10**, 4285–4294 (2010).

31. Stauber, T., Peres, N. M. R. & Geim, A. K. Optical conductivity of graphene in the visible region of the spectrum. *Phys. Rev. B - Condens. Matter Mater. Phys.* **78**, 1–8 (2008).

32. Kuzmenko, A. B., Van Heumen, E., Carbone, F. & Van Der Marel, D. Universal optical conductance of graphite. *Phys. Rev. Lett.* **100**, 2–5 (2008).

33. Li, Z. Q. *et al.* Dirac charge dynamics in graphene by infrared spectroscopy. *Nat. Phys.* **4**, 6–9 (2008).

34. Wang, F. *et al.* Gate-Variable Optical Transitions in Graphene. *Science (80-.).* **320**,

206–209 (2008).

35. Vasko, F. T. Saturation of interband absorption in graphene. *Phys. Rev. B - Condens. Matter Mater. Phys.* **82**, 1–6 (2010).

36. Bolotin, K. I. *et al.* Ultrahigh electron mobility in suspended graphene. *Solid State Commun.* **146**, 351–355 (2008).

37. Gannett, W. *et al.* Boron nitride substrates for high mobility chemical vapor deposited graphene. *Appl. Phys. Lett.* **98**, 24–27 (2011).

38. Li, X. *et al.* Large-area synthesis of high-quality and uniform graphene films on copper foils. *Science (80-.).* **324**, 1312–1314 (2009).

39. Li, X. *et al.* Transfer of large-area graphene films for high-performance transparent conductive electrodes. *Nano Lett.* **9**, 4359–4363 (2009).

40. Novoselov, K. S. *et al.* Two-dimensional gas of massless Dirac fermions in graphene. *Nature* **438**, 197–200 (2005).

41. Zhang, Y. B., Tan, Y. W., Stormer, H. L. & Kim, P. Experimental observation of the quantum Hall effect and Berry's phase in graphene. *Nature* **438**, 201–204 (2005).

42. Kim, K., Choi, J.-Y., Kim, T., Cho, S.-H. & Chung, H.-J. A role for graphene in silicon-based semiconductor devices. *Nature* **479**, 338–44 (2011).

43. Xia, F., Mueller, T., Lin, Y., Valdes-Garcia, A. & Avouris, P. Ultrafast graphene photodetector. *Nat. Nanotechnol.* **4**, 839–843 (2009).

44. Mueller, T., Xia, F. & Avouris, P. Graphene photodetectors for high-speed optical communications. *Nat. Photonics* **4**, 297–301 (2010).

45. Liu, M. *et al.* A graphene-based broadband optical modulator. *Nature* **474**, 64–67 (2011).

46. Sensale-Rodriguez, B. *et al.* Broadband graphene terahertz modulators enabled by intraband transitions. *Nat. Commun.* **3**, 780 (2012).

47. Bao, Q. *et al.* Broadband graphene polarizer. *Nat. Photonics* **5**, 411–415 (2011).

48. Bao, Q. *et al.* Atomic-layer craphene as a saturable absorber for ultrafast pulsed lasers. *Adv. Funct. Mater.* **19**, 3077–3083 (2009).

49. Sun, Z. *et al.* Graphene Mode-Locked Ultrafast Laser. *ACS Nano* **4**, 803–810 (2010).

50. Nair, R. R. *et al.* Fine Structure Constant Defines Visual Transperency of Graphene. *Science (80-.).* **320**, 2008 (2008).

51. Reed, G. T. & Jason Png, C. E. Silicon optical modulators. *Mater. Today* **8**, 40–50 (2005).

52. Green, W. M., Rooks, M. J., Sekaric, L. & Vlasov, Y. a. Ultra-compact, low RF power, 10 Gb/s silicon Mach-Zehnder modulator. *Opt. Express* **15**, 17106–13 (2007).

53. Kim, J. H. *et al.* 40 Gbit/s silicon optical modulator for high-speed applications. *Japanese J. Appl. Physics, Part 1 Regul. Pap. Short Notes Rev. Pap.* **43**, 608–610 (2004).

54. Zortman, W. a., Watts, M. R., Trotter, D. C., Young, R. W. & Lentine, A. L. Low-power high-speed silicon microdisk modulators. *Lasers Electro-Optics Quantum Electron. Laser Sci. Conf. (QELS), 2010 Conf.* 4–5 (2010). doi:10.1364/CLEO.2010.CThJ4

55. Xu, Q., Manipatruni, S., Schmidt, B., Shakya, J. & Lipson, M. 12.5 Gbit/s silicon micro-ring silicon modulators. *Conf. Lasers Electro-Optics, 2007, CLEO 2007* **15**, 430–436 (2007).

56. Feng, N.-N. *et al.* 30GHz Ge electro-absorption modulator integrated with 3 µm silicon-on-insulator waveguide. *Opt. Express* **19**, 7062–7 (2011).

57. Tang, Y. *et al.* 50 Gb/s hybrid silicon traveling-wave electroabsorption modulator. *Opt. Express* **19**, 5811–5816 (2011).

58. Compton, O. C. & Nguyen, S. T. Graphene oxide, highly reduced graphene oxide, and graphene: Versatile building blocks for carbon-based materials. *Small* **6**, 711–723 (2010).

59. Mcallister, M. J. *et al.* Expansion of Graphite. *Chem. Mater.* **19**, 4396–4404 (2007).

60. Mas-Ballesté, R., Gómez-Navarro, C., Gómez-Herrero, J. & Zamora, F. 2D materials: to graphene and beyond. *Nanoscale* **3**, 20–30 (2011).

61. Gao, W., Alemany, L. B., Ci, L. & Ajayan, P. M. New insights into the structure and reduction of graphite oxide. *Nat. Chem.* **1**, 403–408 (2009).

62. Hofmann, U. & Holst, R. Über die Säurenatur und die Methylierung von Graphitoxyd. *Berichte der Dtsch. Chem. Gesellschaft* **72**, 754–771 (1939).

63. Ruess, G. Über das Graphitoxyhydroxyd (Graphitoxyd). *Monatshefte für Chemie und verwandte Teile anderer Wissenschaften* **76**, 381–417 (1947).

64. Scholz, W. & Boehm, H. P. Betrachtungen zur Struktur des Graphitoxids. *Zeitschrift für Anorg. und Allg. Chemie* **369**, 327–340 (1969).

65. Nakajima, T. & Matsuo, Y. Formation process and structure of graphite oxide. *Carbon N. Y.* **32**, 469–475 (1994).

66. He, H., Klinowski, J., Forster, M. & Lerf, A. A new structural model for graphite oxide. *Chem. Phys. Lett.* **287**, 53–56 (1998).

67. Shao, G. *et al.* Graphene oxide: The mechanisms of oxidation and exfoliation. *J. Mater. Sci.* **47**, 4400–4409 (2012).

68. Sheka, E. F. & Popova, N. a. Molecular theory of graphene oxide. *Phys. Chem. Chem. Phys.* **15**, 13304–22 (2013).

69. Lerf, A., He, H., Forster, M. & Klinowski, J. Structure of Graphite Oxide Revisited. *J.*

Phys. Chem. B **102**, 4477–4482 (1998).

70. Dikin, D. a *et al.* Preparation and characterization of graphene oxide paper. *Nature* **448**, 457–460 (2007).

71. Gonçalves, G. *et al.* Breakdown into nanoscale of graphene oxide: Confined hot spot atomic reduction and fragmentation. *Sci. Rep.* **4**, 6735 (2014).

72. Gao, W., Dreyer, D. R., Park, S., Bielawski, C. W. & Ruoff, R. S. The chemistry of graphene oxide. *Chem. Soc. Rev.* **39**, 228–240 (2010).

73. Li, D., Müller, M. B., Gilje, S., Kaner, R. B. & Wallace, G. G. Processable aqueous dispersions of graphene nanosheets. *Nat. Nanotechnol.* **3**, 101–105 (2008).

74. Dimiev, A. M., Alemany, L. B. & Tour, J. M. Graphene oxide. Origin of acidity, its instability in water, and a new dynamic structural model. *ACS Nano* **7**, 576–588 (2013).

75. Fiorillo, M. *et al.* Graphene oxide selectively targets cancer stem cells , across multiple tumor types : Implications for non-toxic cancer treatment , via " differentiation-based nano-therapy ". *Oncotarget* **6**, 3553–3562 (2015).

76. Chien, C. T. *et al.* Tunable photoluminescence from graphene oxide. *Angew. Chemie - Int. Ed.* **51**, 6662–6666 (2012).

77. Kundu, A., Layek, R. K., Kuila, A. & Nandi, A. K. Highly fluorescent graphene oxide-poly(vinyl alcohol) hybrid: An effective material for specific Au 3+ ion sensors. *ACS Appl. Mater. Interfaces* **4**, 5576–5582 (2012).

78. Jung, J. H., Cheon, D. S., Liu, F., Lee, K. B. & Seo, T. S. A graphene oxide based immuno-biosensor for pathogen detection. *Angew. Chem. Int. Ed. Engl.* **49**, 5708–5711 (2010).

79. Sun, X. *et al.* Nano-Graphene Oxide for Cellular Imaging and Drug Delivery. *Nano Res* **1**, 203–212 (2008).

80. Peng, C., Hu, W., Zhou, Y., Fan, C. & Huang, Q. Intracellular imaging with a graphene-based fluorescent probe. *Small* **6**, 1686–1692 (2010).

81. Narayanan, T. N. *et al.* Hybrid 2D nanomaterials as dual-mode contrast agents in cellular imaging. *Adv. Mater.* **24**, 2992–2998 (2012).

82. Robinson, J. T. *et al.* Ultrasmall reduced graphene oxide with high near-infrared absorbance for photothermal therapy. *J. Am. Chem. Soc.* **133**, 6825–6831 (2011).

83. Eda, G., Mattevi, C., Yamaguchi, H., Kim, H. & Chhowalla, M. Insulator to semimetal transition in graphene oxide. *J. Phys. Chem. C* **113**, 15768–15771 (2009).

84. Wang, S. *et al.* High mobility, printable, and solution-processed graphene electronics. *Nano Lett.* **10**, 92–98 (2010).

85. Feng, X., Chen, W. & Yan, L. Electrochemical reduction of bulk graphene oxide

materials. *RSC Adv.* **6**, 80106–80113 (2016).

86. Tressler, J. F., Alkoy, S. & Newnham, R. E. Piezoelectric sensors and sensor materials. *J. Electroceramics* **2**, 257–272 (1998).

87. Praveenkumar, B., Kumar, H. H. & Kharat, D. K. Study on microstructure, piezoelectric and dielectric properties of 3-3 porous PZT composites. *J. Mater. Sci. Mater. Electron.* **17**, 515–518 (2006).

88. Salib, M. *et al.* Silicon Photonics. *Intel Technol. J.* **8**, 143–160 (2004).

89. Kakarantzas, G. *et al.* Structural rocking filters in highly birefringent photonic crystal fiber. *Opt. Lett.* **28**, 158–160 (2003).

90. Dong, X., Tam, H. Y. & Shum, P. Temperature-insensitive strain sensor with polarization-maintaining photonic crystal fiber based Sagnac interferometer. *Appl. Phys. Lett.* **90**, 88–91 (2007).

91. Gahir, H. K. & Khanna, D. Design and development of a temperature-compensated fiber optic polarimetric pressure sensor based on photonic crystal fiber at 1550 nm. *Appl. Opt.* **46**, 1184–9 (2007).

92. Fu, H. Y. *et al.* Pressure sensor realized with polarization-maintaining photonic crystal fiber-based Sagnac interferometer. *Appl. Opt.* **47**, 2835–2839 (2008).

93. De Brabander, G. N., Boyd, J. T. & Beheim, G. Integrated Optical Ring Resonator With Micromechanical Diaphragm for Pressure Sensing. *IEEE Photonic Technol. Lett.* **6**, 6–8 (1994).

94. Kodl, G. A new optical waveguide pressure sensor using evanescent field. *2004 Proceedings. 54th Electron. Components Technol. Conf. (IEEE Cat. No.04CH37546)* 1943–1946 (2004). doi:10.1109/ECTC.2004.1320392

95. Blake, P. *et al.* Making graphene visible. *Appl. Phys. Lett.* **91**, 2–4 (2007).

96. Biniak, S. THE CHARACTERIZATION OF ACTIVATED CARBONS WITH OXYGEN AND NITROGEN SURFACE GROUPS. *Carbon N. Y.* **35**, 1799–1810 (1997).

97. Susi, T., Pichler, T. & Ayala, P. X-ray photoelectron spectroscopy of graphitic carbon nanomaterials doped with heteroatoms. *Beilstein J. Nanotechnol* **6**, 177–192 (2015).

98. Qian;, C. C. A. H. E. L. H. Rayleigh imaging of graphene and graphene layers, Nano. *Nano Lett.* **7**, 2711–2717 (2007).

99. DoITPoMS. Raman scattering. *DoITPoMS* 1 Available at: http://www.doitpoms.ac.uk/tlplib/raman/raman_scattering.php. (Accessed: 5th September 2016)

100. Ferrari, A. & Basko, D. Raman spectroscopy as a versatile tool for studying the properties of graphene. *Nat. Nanotechnol.* **8**, 235–46 (2013).

101. Malard, L. M., Pimenta, M. a., Dresselhaus, G. & Dresselhaus, M. S. Raman

spectroscopy in graphene. *Phys. Rep.* **473**, 51–87 (2009).

102. Bao, Q. & Loh, K. P. Graphene photonics, plasmonics, and broadband optoelectronic devices. *ACS Nano* **6**, 3677–3694 (2012).

103. Xia, F., Yan, H. & Avouris, P. The interaction of light and graphene: Basics, devices, and applications. *Proc. IEEE* **101**, 1717–1731 (2013).

104. Tielrooij, K. J. *et al.* Photoexcitation cascade and multiple hot-carrier generation in graphene. *Nat. Phys.* **9**, 248–252 (2013).

105. Smith, B. T. *et al.* Fundamentals of Silicon Photonic Devices. *Kotura* 1–7 (2006).

106. Kurdi, B. N. & Hall, D. G. Optical waveguides in oxygen-implanted buried-oxide silicon-on-insulator structures. *Opt. Lett.* **13**, 175 (1988).

107. Soref, R. A. Silicon-Based Optoelectronics. *Proc. IEEE* **81**, 1687–1706 (1993).

108. Ohkawa, M., Izutsu, M. & Sueta, T. Integrated optic pressure sensor on silicon substrate. *Appl. Opt.* **28**, 5153–7 (1989).

109. Roelkens, G., Van Thourhout, D. & Baets, R. High efficiency Silicon-on-Insulator grating coupler based on a poly-Silicon overlay. *Opt Express* **14**, 11622–11630 (2006).

110. Bauters, J. F. *et al.* Ultra-low loss silica-based waveguides with millimeter bend radius. *Eur. Conf. Opt. Commun. ECOC* **1**–**2**, 23–25 (2010).

111. Xiao, S., Khan, M. H., Shen, H. & Qi, M. Compact silicon microring resonators with ultra-low propagation loss in the C band. *Opt. Express* **15**, 14467–14475 (2007).

112. Biberman, A., Shaw, M. J., Timurdogan, E., Wright, J. B. & Watts, M. R. Ultralow-loss silicon ring resonators. *IEEE Int. Conf. Gr. IV Photonics GFP* **37**, 39–41 (2012).

113. Niehusmann, J., Vörckel, A., Bolivar, P. H., Wahlbrink, T. & Henschel, W. Microring Resonator. *Opt. Lett.* **29**, 2861–2863 (2004).

114. Herres, D. Basics of TEM, TE, and TM propagation. *Design World* (2015). Available at: http://www.designworldonline.com/basics-of-tem-te-and-tm-propagation/.

115. Bogaerts, W. *et al.* Silicon microring resonators. *Laser Photonics Rev.* **6**, 47–73 (2012).

116. Sefunc, M. A., Pollnau, M. & Garcia-Blanco, S. M. Low-loss sharp bends in polymer waveguides enabled by the introduction of a thin metal layer. *Opt. Express* **21**, 29808–29817 (2013).

117. Khan, I. & Rahman, M. Bending Loss Analysis of Optical Waveguide for SOI & SOS Material System towards Photonic Integration. *Proc. 4th Glob. Eng. Sci. Technol. Conf.* 1–8 (2013).

118. Zhao, X. *et al.* A nano-opto-mechanical pressure sensor via ring resonator. *Opt. Express* **20**, 8535 (2012).

119. Zhao, Y.-G. *et al.* Polymer waveguides useful over a very wide wavelength range from

the ultraviolet to infrared. *Appl. Phys. Lett.* **77**, 2961 (2000).

120. Ferreira, P. H. D., Stefanutti, R., Pavinatto, F. J. & Mendonça, C. R. Femtosecond laser fabrication of waveguides in DR13-doped PMMA. *Opt. Commun.* **318**, 53–56 (2014).

121. Prajzler, V. *et al.* Design, Fabrication and Measurement Polymethylmethacrylate Optical Waveguides Prepared by Modification of Surface Profile by Applying Electric Field. *Electroscope* (2010).

122. Project, C. Home Page. (2021). Available at: https://www.cornerstone.sotonfab.co.uk/. (Accessed: 2nd March 2021)

123. Jeong, H. J. *et al.* One-step transfer and integration of multifunctionality in CVD graphene by TiO2/graphene oxide hybrid layer. *Small* **10**, 2057–2066 (2014).

124. Liu, S. *et al.* Fast and controllable fabrication of suspended graphene nanopore devices. *Nanotechnology* **23**, 1–6 (2012).

125. Lee, G.-H. *et al.* High-strength chemical-vapor-deposited graphene and grain boundaries. *Science (80-.).* **340**, 1073–1076 (2013).

126. CVD Graphene Growth/Transfer. (2016). Available at: http://ishigamigroup.wikidot.com/graphene.

127. Speciality Coating Systems. Parylene Deposition Process. (2021). Available at: https://scscoatings.com/parylene-coatings/parylene-deposition/. (Accessed: 4th April 2021)

128. Mudumba, S. *et al.* Photonic ring resonance is a versatile platform for performing multiplex immunoassays in real time. *J. Immunol. Methods* **448**, 34–43 (2017).

129. Fu, Y. Q., Colli, A. & Fasoli, A. Deep reactive ion etching as a tool for nanostructure fabrication Deep reactive ion etching as a tool for nanostructure fabrication. *J. Vac. Sci. Technol. B Microelectron. Nanom. Struct. Process. Meas. Phenom.* **27**, 1520 (2009).

130. Larciprete, R. *et al.* Dual Path Mechanism in the Thermal Reduction of Graphene Oxide. *J. Am. Chem. Soc.* **133**, 17315–17321 (2011).

131. Lucchese, M. M. *et al.* Quantifying ion-induced defects and Raman relaxation length in graphene. *Carbon N. Y.* **48**, 1592–1597 (2010).

132. Tuinstra, F. & Koenig, L. Raman Spectrum of Graphite. *J. Chem. Phys.* **53**, 1126–1130 (1970).

133. Childres, I., Jauregui, L., Park, W., Cao, H. & Chen, Y. Raman Spectroscopy of Graphene and Related Materials. *New Dev. Phot. Mater. Res.* **1**, 1–20 (2013).

134. Menon, V. M., Tong, W. & Forrest, S. R. Control of quality factor and critical coupling in microring resonators through integration of a semiconductor optical amplifier. *IEEE Photonics Technol. Lett.* **16**, 1343–1345 (2004).

135. Li, H., Anugrah, Y., Koester, S. J. S. & Li, M. Optical absorption in graphene integrated on silicon waveguides. *Appl. Phys. Lett.* **111110**, 1–5 (2012).